TU/e EINDHOVEN UNIVERSITY OF TECHNOLOGY

Liquid-liquid processes in spinning disc equipment

Citation for published version (APA):
Visscher, F. (2013). *Liquid-liquid processes in spinning disc equipment.* [Phd Thesis 1 (Research TU/e / Graduation TU/e), Chemical Engineering and Chemistry]. Technische Universiteit Eindhoven. https://doi.org/10.6100/IR758245

DOI:
10.6100/IR758245

Document status and date:
Published: 01/01/2013

Document Version:
Publisher's PDF, also known as Version of Record (includes final page, issue and volume numbers)

Please check the document version of this publication:

• A submitted manuscript is the version of the article upon submission and before peer-review. There can be important differences between the submitted version and the official published version of record. People interested in the research are advised to contact the author for the final version of the publication, or visit the DOI to the publisher's website.
• The final author version and the galley proof are versions of the publication after peer review.
• The final published version features the final layout of the paper including the volume, issue and page numbers.

Link to publication

General rights
Copyright and moral rights for the publications made accessible in the public portal are retained by the authors and/or other copyright owners and it is a condition of accessing publications that users recognise and abide by the legal requirements associated with these rights.

• Users may download and print one copy of any publication from the public portal for the purpose of private study or research.
• You may not further distribute the material or use it for any profit-making activity or commercial gain
• You may freely distribute the URL identifying the publication in the public portal.

If the publication is distributed under the terms of Article 25fa of the Dutch Copyright Act, indicated by the "Taverne" license above, please follow below link for the End User Agreement:

www.tue.nl/taverne

Take down policy
If you believe that this document breaches copyright please contact us at:

openaccess@tue.nl

providing details and we will investigate your claim.

Download date: 04. Oct. 2023

Liquid-liquid processes in spinning disc equipment

PROEFSCHRIFT

ter verkrijging van de graad van doctor aan de Technische Universiteit Eindhoven, op gezag van de rector magnificus prof.dr.ir. C.J. van Duijn, voor een commissie aangewezen door het College voor Promoties, in het openbaar te verdedigen op maandag 23 september 2013 om 16:00 uur

door

Frans Visscher

geboren te Zaanstad

Dit proefschrift is goedgekeurd door de promotiecommissie:

voorzitter:	prof.dr.ir. R.A.J. Janssen
1e promotor:	prof.dr.ir. J.C. Schouten
copromotor(en):	dr.ir. J. van der Schaaf
leden:	dr. K.V.K. Boodhoo (Newcastle University)
	prof.dr.ir. A.I. Stankiewicz (TUD)
	prof.dr. J. Meuldijk
	dr.ir. A. de Rijke (DSM Research)
adviseur(s):	dr. M.H.J.M. de Croon

Eindhoven University of Technology, 2013

A catalogue record is available from the Eindhoven University of Technology Library

Visscher, Frans
Liquid-liquid processes in spinning disc equipment

ISBN: 978-90-386-3438-8

Printed by Ipskamp Drukkers, The Netherlands

Het begin van wijsheid is dat je wijsheid zoekt,
aan alles wat je hebt verworven, inzicht toevoegt.

Spreuken 4:7 (NBV)

The beginning of wisdom is this: Get wisdom,
And whatever you get, get insight.

Proverbs 4:7 (ESV)

Table of Contents

Summary

Liquid-liquid processes in spinning disc equipment

Liquid-liquid processes are widely encountered in chemical industry and can be divided in liquid-liquid reactions and liquid-liquid extractions. This thesis describes the research and development program leading to novel and compact equipment for liquid-liquid processes, which is based on spinning disc technology. In this equipment two immiscible phases are contacted, either in co-current mode or in counter-current mode.

Spinning disc technology utilizes high-gravity, high-shear conditions, and is known for its high gas-liquid, liquid-liquid, and liquid-solid mass transfer rates. Because of its low surface area, the equipment could be coated with materials suited for strong corrosive environments, like titanium, platinum, and tantalum. Also, the low volume allows one to rapidly change the product stream without losing valuable time for equipment cleaning. Last, the required floor space is reduced.

Liquid-liquid extraction is a purification technique based on the distribution of a solute over two immiscible liquid phases. It is used in many processes in the chemical industry. Most industrial extractions are performed in counter-current operated extraction columns. When operated in counter-current mode, multiple stages of consecutive mixing and separation are applied. By operating the column in counter-current mode, it becomes possible to transfer the solute almost completely from one liquid to the other. When the density difference between the liquids is small, the required extractor length is increased. As a result, industrial used extraction columns may have inventories up to 700 m^3 and processing times in the range of hours. Centrifugal extractors were developed to reduce the inventory volume and residence time.

In this thesis, first a reactor model is presented for the single phase fluid flow in a rotor-stator spinning disc reactor. This reactor model is based on residence time distribution (RTD) measurements which are obtained as a function of the rotor-stator distance, rotational speed and the volumetric flow rate. For the RTD measurements water soluble ink is injected pulse wise at the reactor inlet. The RTD can be described by a plug flow model in combination with 2 to 3 ideally stirred tanks-in-series.

Next, the single phase study is extended to a multiphase study in which two immiscible liquids, *n*-heptane and water, are contacted in a rotor-stator spinning disc reactor. The volume fractions are measured using γ-ray tomography and photographic image analysis as a function of rotational disc speed, flow ratio, position in the reactor, and rotor material.

The volume fraction of *n*-heptane is close to the ratio of the *n*-heptane volumetric flow rate to the total volumetric flow rate, for rotation speeds ranging from 0-1600 RPM.

With the volume fractions known, the liquid-liquid mass transfer rates are measured in a rotor-stator spinning disc reactor. For this purpose, benzoic acid is extracted from *n*-heptane to water. The liquid-liquid mass transfer rate increases from 0.2 $m^3_{ORG}\ m^{-3}_{R}\ s^{-1}$ at 100 RPM, to 51.5 $m^3_{ORG}\ m^{-3}_{R}\ s^{-1}$ at 1600 RPM. This is at least 25 times higher compared to those in packed columns, and 15 times higher compared to those in state of the art microchannels.

Next, the liquid-liquid flow in an impeller-stator spinning disc reactor is studied. For this purpose water and *n*-heptane are contacted as a function of the rotational speed and the volume fractions, and is characterized by six different flow regimes. The impeller is able to selectively pump *n*-heptane through the reactor, whilst it is intensively mixed with water that remains in the reactor.

Based on the results discussed above, a counter-current operated spinning disc extractor is presented**.** This extractor is based on rotor-impeller-rotor spinning disc technology and processes up to 5 m^3 liquid per day. The mixing intensity and the separation efficiency of the extractor can be chosen independently by adjusting the rotation speed of the impeller and of the enclosure. The height of a transfer unit, and thus the extractor volume, is ten times lower compared to other types of centrifugal extractors.

In the final chapter of this thesis, the single stage spinning disc extractor is extended with two additional stages. The separation efficiency at the extractor outlets, and the separation between the consecutive stages are determined.

As a result of the chapters above, a promising alternative for liquid-liquid extraction equipment is presented in this thesis. The mixing intensity in the extractor is tuned independently of the separation efficiency, by adjusting the rotation speed difference between the impeller and the enclosure. The extractor has a low volume per stage (102 10^{-6} m^3 per stage), high separation efficiency (>99.9%), and can be extended to 71 consecutive contacting stages per meter.

Samenvatting

Liquid-liquid processes in spinning disc equipment

Vloeistof-vloeistof processen komen veel voor in de chemische industrie, en kunnen worden onderverdeeld in vloeistof-vloeistof reacties en vloeistof-vloeistof extracties. In dit proefschrift staat het onderzoek naar een nieuw compact apparaat beschreven dat is gebaseerd op spinning disc technologie. In het apparaat kunnen twee niet mengbare vloeistoffen zowel in meestroom als in tegenstroom worden gemengd.

Spinning disc technologie maakt gebruik van een hoge afschuifspanning en een hoog krachtenveld om de vloeistof-vloeistof menging te intensiveren. Door het lage extractorvolume kunnen constructiematerialen worden toegepast die geschikt zijn voor zeer corrosieve omstandigheden. Daarnaast maakt deze extractor het mogelijk om snel van voedingsstroom te wisselen zonder dat er tijd verloren gaat in het reinigen van de extractor. Ten slotte neemt het benodigde vloeroppervlak af op de productielocatie waar het apparaat is geplaatst.

Vloeistof-vloeistof extractie is een zuiveringstechniek, die gebaseerd is op de verdeling van een opgeloste component over twee niet-mengbare vloeistoffen. De techniek wordt in diverse sectoren van de chemische industrie toegepast. Veel industriële extracties worden uitgevoerd in tegenstrooms bedreven extractiekolommen. Bij een tegenstroomsextractie worden meerdere seriële extractietrappen toegepast, waarbij in elke trap de vloeistoffen intensief worden gedispergeerd en gescheiden. Door de vloeistoffen in tegenstroom te contacteren kan een component tussen de twee vloeistoffen volledig worden uitgewisseld. Wanneer het dichtheidsverschil tussen de vloeistoffen gering is neemt de benodigde extractorlengte toe. Dergelijke kolommen kunnen daardoor een volume hebben van 700 m^3 en een verblijftijd van enkele uren. Centrifugaalextractoren zijn ontwikkeld om het extractorvolume en de verblijftijd daarin te verkleinen.

Dit proefschrift beschrijft een model van het vloeistofgedrag van één vloeistoffase in een rotor-stator spinning disc reactor (SDR). Dit model is gebaseerd op metingen van de verblijftijdsspreiding (RTD). De RTD is gemeten als functie van de afstand tussen de rotor en de stator, de rotatiesnelheid, en het vloeistofdebiet. De RTD metingen zijn uitgevoerd door pulsgewijs wateroplosbare inkt te injecteren. De RTD in de reactor kan worden beschreven als een propstroomvolume in combinatie met 2-3 ideaal geroerde volumes in serie.

Vervolgens beschrijft de volumefracties van water en *n*-heptaan in de SDR die zijn gemeten met behulp van γ-straaltomografie en fotografie. Water en *n*-heptaan zijn gebruikt als testsysteem. De volumefracties zijn bepaald als functie van rotatiesnelheid, vloeistofdebieten, positie in de reactor en het constructiemateriaal van de rotor. De volumefractie van *n*-heptaan is nagenoeg gelijk aan de verhouding tussen het *n*-heptaan vloeistofdebiet en het totale vloeistofdebiet, voor rotatiesnelheden tot 1600 RPM.

Ook is de vloeistof-vloeistof-stofoverdrachtsnelheid in de SDR als functie van de rotatiesnelheid en het vloeistofdebiet bepaald. Deze is gemeten door benzoëzuur vanuit *n*-heptaan naar water te extraheren. De vloeistof-vloeistof-stofoverdracht-snelheid neemt toe van 0.2 $m^3_{ORG}\ m^{-3}_R\ s^{-1}$ bij 100 rotaties per minuut (RPM) naar 51.5 $m^3_{ORG}\ m^{-3}_R\ s^{-1}$ bij 1600 RPM. Deze stofoverdrachtsnelheid is 25 maal hoger dan de waarden uit de literatuur voor gepakte kolommen en 15 keer hoger dan de crème de la crème uit de microreactortechnologie.

Daaropvolgend is het stromingsgedrag van water en *n*-heptaan in een impeller-stator spinning disc reactor beschreven als een functie van de rotatiesnelheid en de volumefractie van water. Het stromingsgedrag kan worden gekarakteriseerd door zes verschillende stromingsprofielen. Daarnaast wordt aangetoond dat een impeller-stator configuratie de mogelijkheid biedt om selectief *n*-heptaan door de reactor te laten stromen, terwijl er intense menging plaats vindt met water dat stationair in de reactor blijft.

Hierna wordt op basis van de gepresenteerde resultaten een tegenstroom bedreven spinning disc extractor gepresenteerd. Deze extractor bestaat uit één rotor-impeller-rotor combinatie, en kan tot 5 m^3 vloeistof per dag verwerken. De vloeistof-vloeistof-menging en de vloeistof-vloeistof scheiding kunnen onafhankelijk van elkaar worden ingesteld door de rotatiesnelheden van de rotor en de impeller te variëren. De hoogte van één extractietrap, en dus ook het extractorvolume, is tien keer lager in vergelijking met conventionele centrifugaalextractoren.

Het laatste hoofdstuk beschrijft hoe de ééntrapsextractor uitgebreid kan worden met twee additionele extractietrappen. Zowel de scheidingsefficiency bij de uitgangen van de extractor, als de scheiding tussen de opeenvolgende extractietrappen is bepaald.

1. Introduction

1.1. Chemical industry

The world chemicals turnover was valued at 2744 billion euro in 2011 (CEFIC, 2012). The European Union contributes 20% to these global sales. Half of the expenditure in the European Union is due to polymers and petrochemicals (**Figure 1**). Most of these industrial processes are combinations of one or more reaction steps, with one or more purification steps.

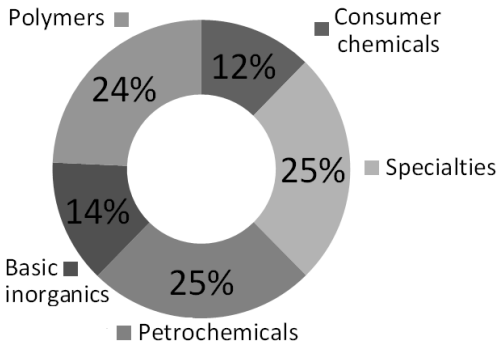

Figure 1. Percentage of European Union chemical industry sales per sector. Specialties involve amongst others auxiliaries for industry and paints & inks. Basic inorganics involve industrial gases, fertilizers and other inorganics (CEFIC, 2012).

There is an urgent need in chemical industry to reduce the equipment volume by a factor 10-100; this need is commonly addressed as process intensification (Stankiewicz et al., 2000). Colin Ramshaw and co-workers were the first pioneers who envisioned the promising future that would originate from the implementation of process intensification (Reay et al., 2008). With a lower equipment volume the holdup of liquids, gases and solids in the reactor is smaller, which reduces the impact of potential escalation of dangerous situations. Also the volume reduction allows for the application of expensive coating materials, like platinum and tantalum. Mechanical agitation is often used to intensify chemical processes in which mixtures of gasses, liquids and solids are involved. The liquid-liquid, gas-liquid or liquid-solid mass transfer rate is increased if the energy dissipation due to mixing is increased.

The research described in this thesis, is part of the "Smart Structured Rotating Reactors"–research program at the Eindhoven University of Technology. The aim of this program is the development of scientific and technological breakthroughs in the understanding, design and operation of equipment for the production of high-added value chemicals. The technological breakthroughs of this research program provide promising perspectives for greenification and intensification of chemicals production. Industrial chemical production becomes more flexible, using low volume equipment and will take place just-in-time and close to the raw materials origin or at the consumer site.

1.2. Liquid-liquid reaction

Liquid-liquid reactions are widely encountered in chemical industry; examples of liquid-liquid reactions that are relevant on industrial scale are, e.g., the exothermic nitration of aromatic compounds (Zaldívar et al., 1996), the production of benzaldehyde, hydroformylation of propene and polymerization reactions like the Shell Higher Olefin Process (Wiseman, 1979). Equipment used for liquid-liquid processes, like stirred tanks and packed columns are space consuming, requiring a significant processing time, and involving severe safety challenges. Therefore equipment, in which liquid-liquid reactions are performed, needs to be intensified: a larger productivity is desired. Such a productivity increase can be obtained by increasing mass transfer rates for processes in which the mass transfer rate is limiting, which is the case for most liquid-liquid processes. The said process intensification can be achieved by applying mechanical agitation in existing equipment. Often, this leads to an increase of the liquid-liquid mass transfer rate and it allows one to prevent hotspot formation which is a common cause of reactor runaway and product degradation in chemical processes.

1.3. Liquid-liquid extraction

Liquid-liquid extraction (LLE) is a purification technique that is widely applied in chemical industry. It is used when other separation techniques are less suited, for example due to temperature sensitivity of the desired product, or when a high boiling component is present in small quantities in a waste stream. LLE is based on the distribution of a solute over two immiscible liquid phases. Intimate contacting of a solute-rich phase (the feed) with a solute-free phase (the solvent) yields two product streams. The solvent is enriched with the solute (the extract), and the feed solution is impoverished with solute (the raffinate), as is shown in **Figure 2**.

Applications of LLE are found in the petrochemical industry (e.g. to separate aliphatic and aromatic product streams (Ali et al., 2003)), in polymer manufacturing (e.g. in the production process of nylon-6 (Alessi et al., 1997)), and in the pharmaceutical industry (e.g. for the production of penicillin (Likidis et al., 1987, Eisenlohr, 1951)). In the early 19th century, Friedrich Sertüner used LLE to obtain morphine (Klockgether-Radke, 2002). At that time LLE was executed batch wise, i.e. over a repetitive sequence of mixing and separation steps that is shown in **Figure 2**. In each contacting stage the solute partitions over the two liquid phases: the solute concentration in the feed solution is decreased and the solute concentration in the solvent is increased.

Ideally, the solute concentrations in both phases are in equilibrium after each contacting step. This is only valid when the liquid-liquid mass transfer rate is high enough at the given residence time.

When these premises are fulfilled, the solute can be almost completely transferred from the feed to the extract after multiple consecutive steps of mixing and separation. LLE is nowadays performed in gravity driven, continuously operated equipment (Míšek, 1994). Both co-current and counter-current operation is possible (**Figure 3** and **Figure 4**).

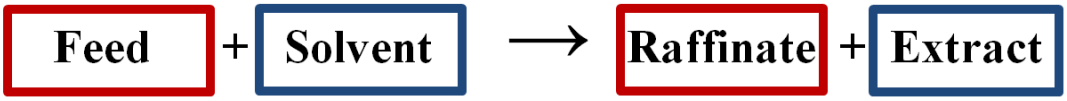

Figure 2. Principle of single stage extraction between an organic phase (Feed, red) and an aqueous phase (Solvent, blue). The organic phase has a high initial solute concentration. The aqueous phase is initially solute-free. The solute is transferred from the organic phase to the aqueous phase during intimate contacting.

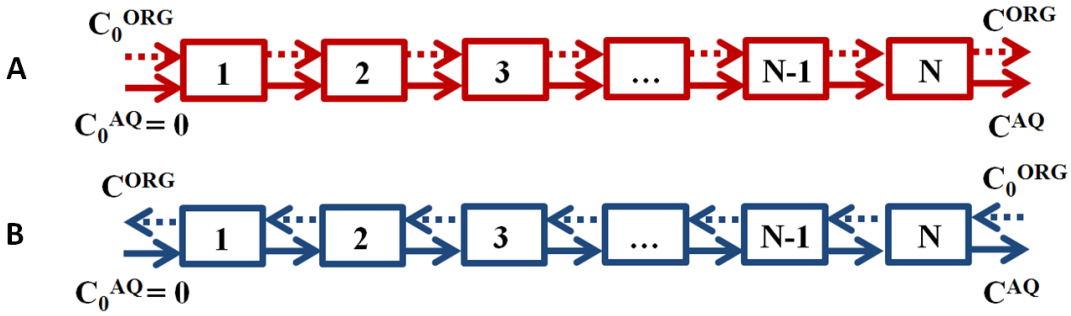

Figure 3. Schematic representation of co-current (A) and counter-current (B) extraction.

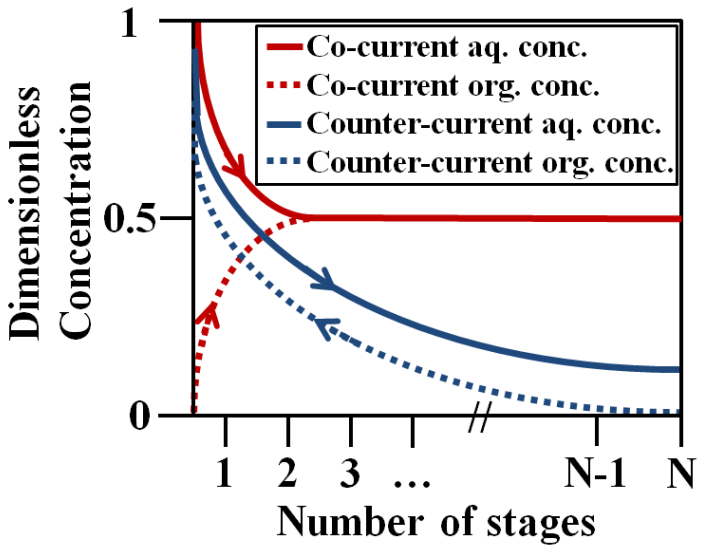

Figure 4. Co-current and counter-current liquid-liquid extraction. In this counter-current example, the solute is transferred almost completely from the solute rich phase (aqueous) to the organic solvent. The partition coefficient of the solute over the two liquids is assumed to be unity, and the concentrations are dimensionless.

When the extraction is operated in counter-current mode, there is a crossover of the solute between two liquids that are flowing in opposite directions. The solute can transfer almost completely from the feed solution to the solvent. When an extractor is operated in co-current mode, the solute concentration in both phases reaches equilibrium. The difference in the experimental procedure between co-current and counter-current extraction is shown in **Figure 3.** The concentration profiles of the extract and the raffinate are shown in **Figure 4**.

1.4. Liquid-liquid extraction equipment

Liquid-liquid extractors can be classified in static columns, rotary-agitated columns, pulsed columns, reciprocating-plate columns, centrifugal extractors, and mixer-settlers (Hashtochahar et al., 2010, Frank et al., 2012, Godfrey et al., 1994). Static columns have a low liquid-liquid mass transfer rate and as a result also a low efficiency: only low amounts of solute can be transferred in these columns. They are used in chemical industry when only a few contact stages are needed. Their main benefit is their low costs and their simplicity. Examples of the static columns are spray columns (Keith et al., 1955), packed columns (Varteressian et al., 2002), and sieve tray columns (Krishna et al., 2002). In spray columns the continuous phase circulates, while the dispersed phase is fed counter-currently by means of a nozzle or by means of perforated plates in series. Spray columns have a higher liquid-liquid mass transfer rate than other static columns, but have a lower efficiency because the continuous phase suffers of excessive back mixing (Horvath et al., 1978, Seibert et al., 1988, Kumar et al., 1999). Also the nozzles in the spray column entail a significant pressure drop (Trambouze et al., 2002).

Extensive research has been performed in the field of packed liquid-liquid extraction columns (Kumar, 1994). Packed columns are equipped with either a random or structured packing. The interaction between the liquids and the packing is responsible for coalescence and redispersion effects. Because of the packing, the back mixing effects that are encountered in spray columns are much smaller. In packed columns the preferential wetting of the packing is important. If the dispersed phase wets the packing, a thin film flow of the dispersed phase over the packing is present. If the continuous phase wets the packing, the dispersed phase will flow as droplets or rivulets over the packing. Packed columns typically can have a capacity up to 50 m^3_{liquid} $m^{-2}_{extractor}$ h^{-1} (Frank et al., 2012). Sieve tray columns also have a capacity of 50 m^3_{liquid} $m^{-2}_{extractor}$ h^{-1} (Frank et al., 2012). In sieve tray columns the liquid with the higher density flows to the bottom of the extractor across each tray and through the down comers from tray to tray.

The liquid with the lower density is dispersed by the perforations in each tray, and flows through the liquid with the higher density in the form of drops, enters into a flocculation zone, and subsequently coalesces such that it accumulates under each tray (Rocha et al., 1989b, Rocha et al., 1989a, Krishna et al., 2002). Examples of the agitated columns are Scheibel columns (Bonnet et al., 1985), Kuhni-columns (Gomes et al., 2009), Oldshue-Rushton columns (Gutoff, 1965), or rotating disc contactors (Al-Rahawi, 2007, Trambouze et al., 2002). These columns are shown in **Figure 5**.

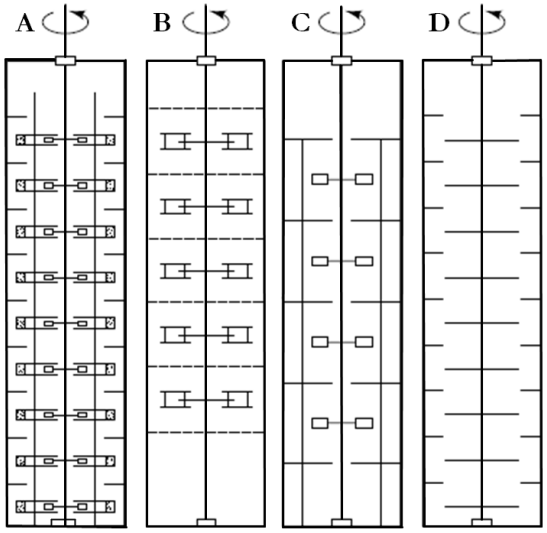

Figure 5. Industrial applied agitated extraction columns: (A) Scheibel column, (B) Kuhni Column, (C) Oldshue-Rushton column, and (D) Rotating disc contactor.

The first design of the Scheibel column consisted of multiple knitted wire-mesh packed sections and an impeller which is rotating around a centered shaft between each packed section (Scheibel et al., 1950). In a later version, flat baffles were added to the end of each knitted wire mesh section. Simultaneously, the impellers were surrounded by stationary shroud baffles (Scheibel, 1956). Because the wire mesh packing is prone to fouling, the packed sections were replaced by agitated sections in a third version.

The Scheibel column is shown in **Figure 5A**, and has a maximum capacity of 25 $m^3_{liquid}\ m^{-2}_{extractor}\ h^{-1}$ (Frank et al., 2012). The Kuhni column uses shrouded turbine impellers as mixing elements on a central shaft (**Figure 5B**). Perforated stator rings are used to separate the extraction stages and to reduce back mixing between stages. Kuhni columns have a typical rotational speed of 10-100 RPM and a maximum capacity of 40 $m^3_{liquid}\ m^{-2}_{extractor}\ h^{-1}$, although much larger columns are applied for dedicated applications. In chemical industry, often the exact geometry of the impeller, the stator rings, and the perforation is changing with the column height because the interfacial tension can vary significant along the column height (Frank et al., 2012, Kumar et al., 1999, Dongaonkar et al., 1991).

The Oldshue-Rushton Column (ORC, **Figure 5C)** and the Rotating Disc Contactor (RDC, **Figure 5D**) have a similar structure. Each contacting stage in the column consists of horizontal doughnut-shaped baffles, and within each compartment in the middle of the column a disk is mounted. The rotating disk is flat and has a diameter which is smaller than the central opening in the stationary baffles. The ORC has a height/diameter ratio of the compartments which is larger than the RDC. Also, in the ORC each compartment is equipped with vertical baffles. The ORC can handle solids. With a decreasing density difference between the two liquids, the extractor length required to obtain an almost complete crossover of the solute is increased. As a result, on an industrial scale, extraction columns may have volumes up to 700 m^3 (Trambouze et al., 2002). Because liquid-liquid extraction often involves liquids with a low vapor pressure the large inventory volume induces safety challenges. Also, a large inventory volume results in large floor space requirements.

1.5. Centrifugal extractors

Centrifugal extractors were developed to reduce the equipment volume by a factor 100, reduce the processing time accordingly and to enhance the separation efficiency (Gebauer et al., 1982). This is especially the case for liquids with a low density difference. In centrifugal extractor the settling effect of a density difference is multiplied by the centrifugal force. Examples of such extractors are the Podbielniak extractor (Barson et al., 1953, Podbielniak et al., 1959), the annular centrifugal extractor (Deshmukh et al., 2007), and the Westfalia/Luwesta extractor (Likidis et al., 1989). An introduction on a wide range of centrifugal extractors is presented elsewhere (Gebauer et al., 1982, Blass, 1994). The Podbielniak extractor allows one to perform counter-current extraction and is shown in **Figure 6** (Barson et al., 1953, Podbielniak et al., 1959). The Podbielniak extractor consists of a cylindrical drum which is rotating around a horizontal shaft. Multiple concentric cylindrical shells are mounted adjacent to the rotating drum. The liquid phase with the higher density is fed through the central shaft. As a result of the centrifugal force and density difference, the liquid phase with the higher density is forced radially outwards to the rim of the drum. Simultaneously, the liquid phase with the lower density is fed to the extractor at the rim of the rotating drum and flows radially inwards. Because of the internal cylindrical shells, multiple consecutive coalescing and dispersion steps are achieved (D.B.Todd et al., 1965). The smallest Podbielniak extractor that is commercially available is the so-called "babypod" (type A1) and has a maximum volumetric flow rate of 0.03 $m^3\ hr^{-1}$ (Frank et al., 2012), an inner diameter of 0.30 m, a maximum rotation speed of 10.000 RPM and an extractor volume of 0.6 10^{-3} m^3 (Gebauer et al., 1982). The largest Podbielniak commercially available (type E-48) has a maximum volumetric flow rate of 113.5 $m^3\ hr^{-1}$, an inner diameter of 1.2 m, a maximum rotational speed of 1600 RPM, and an extractor volume of 0.925 m^3 (Frank et al., 2012).

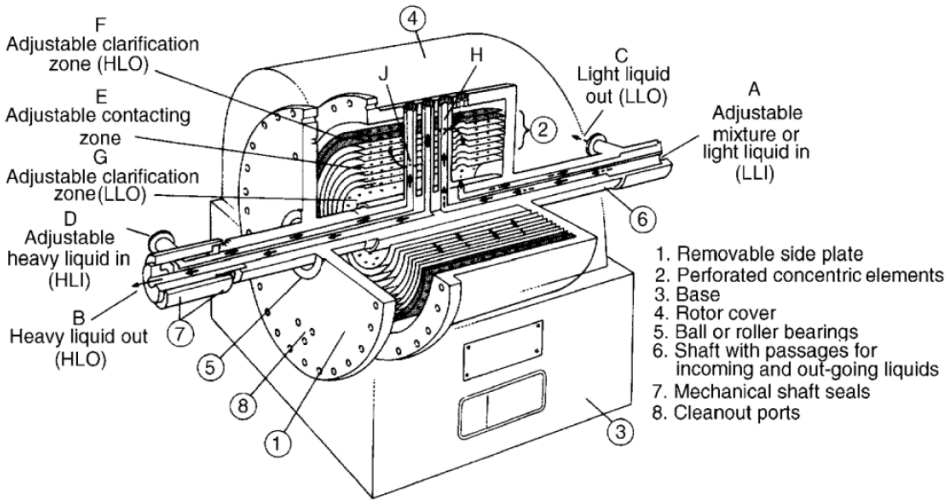

Figure 6. 3D-sideview of the Podbielniak extractor (courtesy of Perking Elmer).

A schematic side view of the annular centrifugal extractor (ACE) is shown in **Figure 7**. An excellent review on the ACE has been published elsewhere (Vedantam et al., 2006). The ACE consists of two coaxial cylinders in which the outer one is stationary and the inner cylinder is rotating. In the extractor mixing takes place in the volume between the inner cylinder and the outer cylinder. Inside the inner cylinder weirs are present which allow for the selective collection of liquids phases (Schuur et al., 2012). Multistage extraction can only be achieved in these extractors by combining various rotor-stator units. The ACE has been used for extraction, emulsion polymerization (Imamura et al., 1993), monodispersed silica particle synthesis (Ogihara et al., 1995), heterogeneous catalysis (Sczechowski et al., 1995), and bio catalytic reactions (Kraai et al., 2008). The ACE is commercialized by e.g. Costner Industries Nevada Corporation (CINC) Inc.

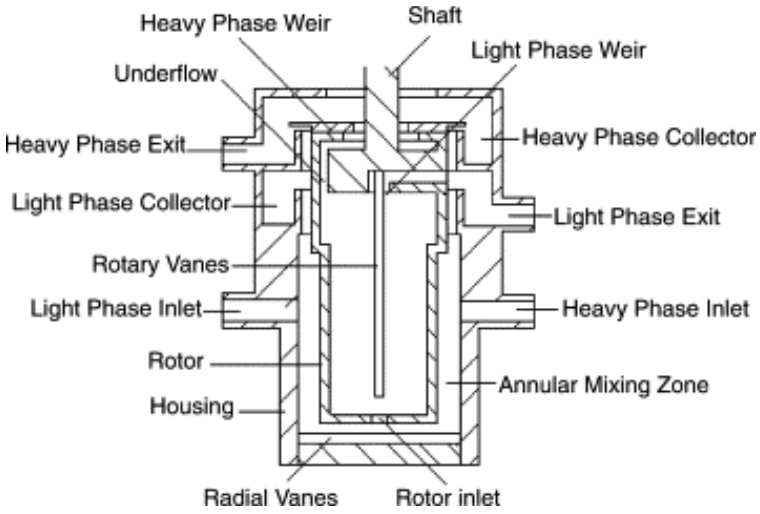

Figure 7. Schematic diagram of the annular centrifugal extractor (Xu et al., 2006).

Rousselet-Robatel has developed single-stage and multistage centrifugal extractors (Miachon, 1980, Buffet, 1981). The multistage extractor is produced for pilot scale and industrial scale. Up to 7 stages can be installed in a single multistage extractor. Each contacting stage consists of a mixing chamber and a decantation chamber; with inter stage counter-current liquid flow. The centrifuge consists of a stationary central axis which is enclosed by a rotating bowl. The rotor-stator configuration is enclosed by a stationary bowl. The high difference in rotational speed between the stationary agitation disc and the rotating walls of the mixing chamber creates a dispersion in which the high interfacial area allows one to achieve high mass transfer rates.

In the Rousselet-Robatel design, increasing the rotational speed will thus influence both the separation efficiency at the extractor outlets and the mixing intensity. The smallest multistage extractor (type LX124) is equipped with 4 consecutive contact stages, has a maximum volumetric flow rate of 30 10^{-3} m^3 hr^{-1}, and a maximum rotational speed of 3600 RPM. The largest multistage extractor (type LX576) is equipped with 6 contacting stages, has a maximum volumetric flow rate of 6.0 m^3 hr^{-1}, and has a maximum rotational speed of 2000 RPM (Gebauer et al., 1982, Rousselet Robatel, 2013).

More extractors exist which are not discussed here because they are not widely used in industry (anymore): The Craig apparatus (Craig et al., 1949) and the Graesser Raining bucket extractor (Coleby, 1962); a more recent innovation is the Coflore extractor (Jones et al., 2012). Also a counter-current operated combination of micro reactors is used to achieve liquid-liquid extraction (Gaakeer et al., 2012, Kashid et al., 2007b).

1.6. Extractor comparison

Comparison of liquid-liquid extractors is an intricate task. Stichlmair made a comparison for liquid-liquid extraction columns which is shown in **Figure 8** (Stichlmair, 1980). In the publication centrifugal extractors were not taken into account. The capacity of the extraction columns, shown in **Figure 8** is defined as m^3_{LIQUID} m^{-2}_{AREA} h^{-1}. The area is calculated from the column diameter. The capacity thus increases with decreasing column diameter, at a given volumetric flow rate.

The Stichlmair plot does not include the extractor residence time, or the energy dissipated in the extractor. Energy can be dissipated in liquid-liquid extraction columns by the rotational shaft, pulsating engine, or by the pumps that force fluids through the columns. In general, for centrifugal extractors the energy dissipation is higher. The number of contacting stages per meter of extractor length is plotted versus the maximum power consumption of the centrifugal extractor motor in **Figure 9**.

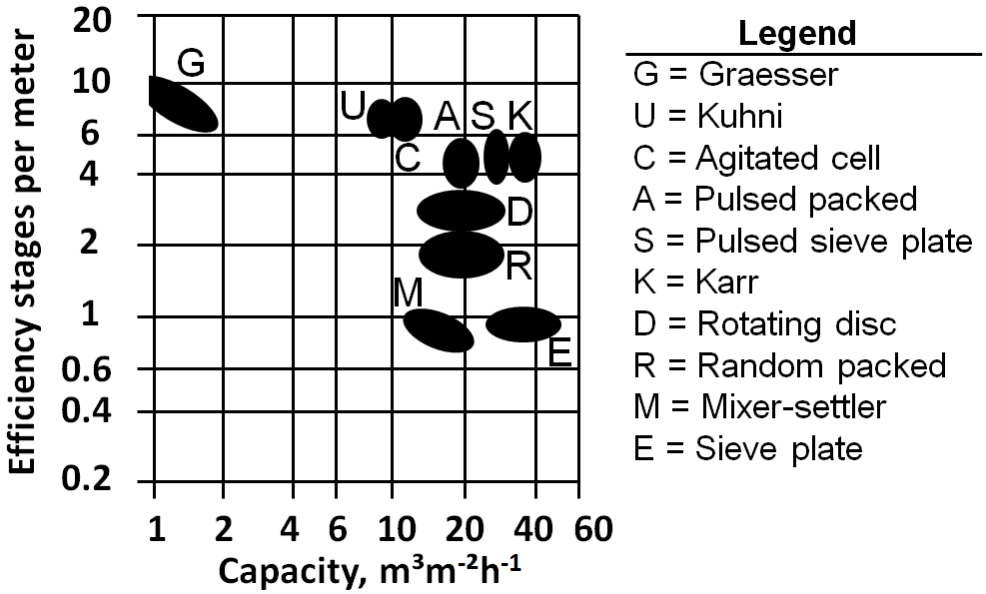

Figure 8. Stichlmair plot, which shows the number of efficiency stages per meter versus the capacity. Only liquid-liquid extraction columns are shown in the initial publication (Stichlmair, 1980).

In **Figure 9**, data from the Podbielniak extractors is taken from (Frank et al., 2012), Data on ACE extractors (from CINC Inc.) is taken from (Schuur et al., 2012), and data for the Rousselet-Robatel extractor is taken from the manufacturer (Rousselet Robatel, 2013). The most suited extractor for a given test case will depend on the required residence time, the settling characteristics of the dispersed phase (surface tension, viscosity), the required scale (volumetric throughput), and the number of contact stages required.

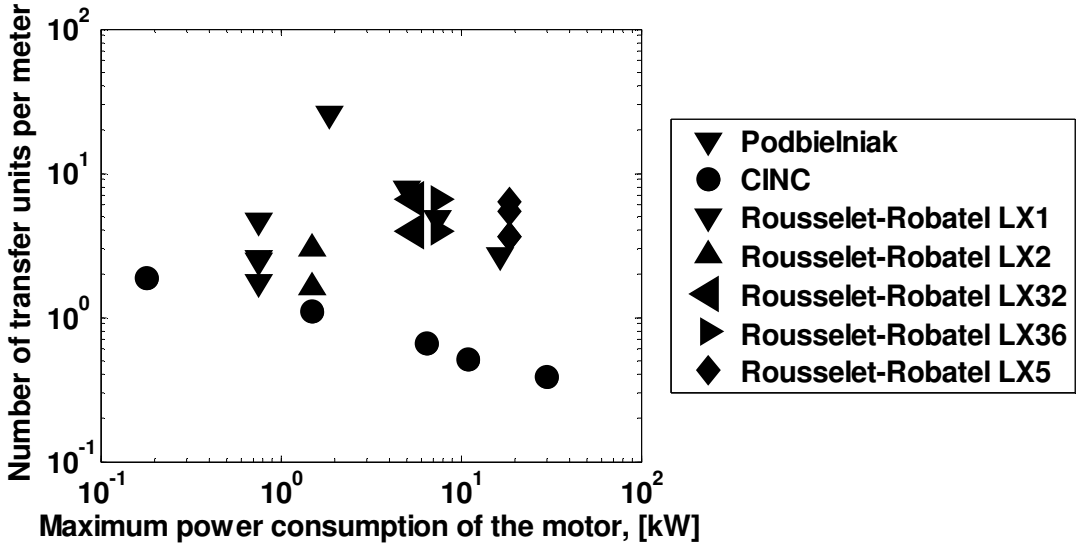

Figure 9. The number of contacting stages per meter of extractor length is plotted versus the maximum power consumption of the centrifugal extractor motor.

1.7. Spinning disc equipment

Three types of spinning disc reactors have been developed. The first type is the so-called free-disc-type. In these reactors a disc is rotating inside a vessel. Rotation of the disc induces recirculation of the liquid, and enhances the mass transfer rates (Schlichting et al., 1999).

The second type is the so-called thin-film spinning disc. In this reactor a liquid is fed at the center of a rotating disc. Due to the rotation, the liquid is forced radially outwards as a thin liquid film. The main principle of this reactor was patented in 1927 (Buhtz, 1927). High gas-liquid, liquid-solid, and heat transfer rates are reported (Burns et al., 2005, Jachuck et al., 2005). This reactor has been used for polymer processing and pharmaceutical production (Boodhoo et al., 2000, Pask et al., 2012, Oxley et al., 2000).

The third type of spinning disc reactor, the rotor-stator spinning disc reactor (SDR), is known for its excellent mixing capability (Meeuwse et al., 2010b, Meeuwse et al., 2010a). In the SDR a rotating disc (rotor) is mounted near a stationary disc (stator) (**Figure 10**). Typically the axial distance is 1 10^{-3} m. Upon rotation of the rotor, the difference in rotational speed between the rotor and the stator induces a velocity gradient that results in a shear force that acts on the droplets, bubbles or particles between the rotor and the stator. Accordingly, an increase of the rotational speed yields an increase of the shear force and thus of the mixing intensity. As a result, the gas-liquid and liquid-solid mass transfer rates in the SDR are higher than for other chemical reactors like e.g. bubble columns (Meeuwse et al., 2010b, Meeuwse et al., 2010a).

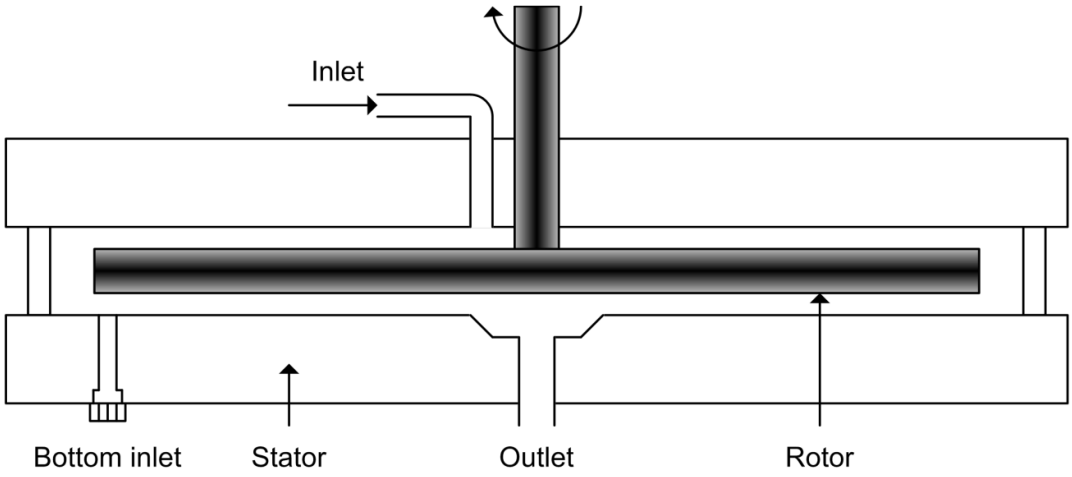

Figure 10. The side view of the rotor-stator spinning disc reactor. Rotation of the rotor induces a velocity gradient between the rotor and the stator. As a result a shear force acts on the droplets, bubbles or particles between the rotor and the stator. This results in high gas-liquid and liquid-solid mass transfer rates. Typically, the axial distance between the rotor and the stator equals 1 10^{-3} m, and the rotor diameter is below 0.135 m.

The volumetric gas-liquid mass transfer coefficient in the case of a 0.135 m rotor is 3 times higher than in case of a 0.066 m wide rotor. The energy dissipation is a factor 8 higher (Meeuwse et al., 2012). Therefore the scale up of a rotor-stator spinning disc reactor is preferentially done via stacking of single stage rotor-stator units in series on a single shaft (Meeuwse et al., 2012).

1.8. The scope and structure of this thesis

The research described in this thesis is carried out within the "Smart Structured Rotating Reactor"-program at the Eindhoven University of Technology. This program has received funding from the European Research Council under the European Community's Seventh Framework Programme (FP7/2007-2013) / ERC grant agreement n° 227010.

The objective of this thesis is to develop novel compact rotating equipment in which two immiscible liquids are intensely contacted over multiple stages. The targeted volume reduction of the equipment is at least two orders of magnitude in comparison with classical equipment. This research has a focus on the application of centrifugal high-shear high-gravity conditions to obtain the said process intensification. The high-shear high-gravity conditions are investigated for liquid-liquid processes in both the rotor-stator and rotor-rotor multiple spinning discs equipment.

Chapter 2 presents a reactor model for the single phase flow in a rotor-stator spinning disc reactor. This reactor model is based on residence time distribution (RTD) measurements. **Chapter 3** expands the single phase study to a multi-phase study; it describes the volume fractions of water and *n*-heptane in a rotor-stator spinning disc reactor, which are measured using γ-ray tomography and photographic image analysis. With these volume fractions known, the liquid-liquid mass transfer rates in a rotor-stator spinning disc reactor are presented in **Chapter 4.** The liquid-liquid mass transfer rates are measured from the extraction of benzoic acid between *n*-heptane and water. In **Chapter 5**, the rotating solid disc is replaced with an impeller. The liquid-liquid flow behavior in an impeller-stator spinning disc reactor is presented. Also the requirements for the selective through flow of *n*-heptane through the reactor are discussed. **Chapter 6** presents a single stage spinning disc extractor that is based on rotor-impeller-rotor technology and processes up to 5 m^3 liquid per day. **Chapter 7** presents a method to scale-up the single stage extractor with two additional contacting stages. The separation efficiency at the extractor outlets and the separation between the consecutive stages are determined. **Chapter 8** presents a summary of the main conclusions from the above mentioned chapters and recommendations for further research.

2. Residence time distribution in a rotor-stator spinning disc reactor

This chapter has been published as:

Visscher F., de Hullu, J. van der Schaaf, J., de Croon, M.H.J.M., Schouten, J.C., **"Single phase residence time distribution in a rotor-stator spinning disc reactor",** *AIChE Journal*, 2013, 59 (7), pp. 2686-2693.

Abstract

This chapter describes a reactor model for the single phase rotor-stator spinning disc reactor based on residence time distribution measurements. For the experimental validation of the model the axial clearance between the rotor and both stators is varied from $1.0 \cdot 10^{-3}$ to $3.0 \cdot 10^{-3}$ m, the rotational disc speed is varied from 50 to 2000 RPM, and the volumetric flow rate is varied from $7.5 \cdot 10^{-6}$ to $22.5 \cdot 10^{-6}$ m^3 s^{-1}. Tracer injection and response experiments show that the residence time distribution can be described by a plug flow model in combination with 2 to 3 ideally stirred tanks-in-series. The resulting reactor model is explained with the effect of turbulence, the formation of von Kármán and Bödewadt boundary layers, and the effect of the volumetric flow rate.

2.1. Introduction

Numerical characterization of the macro-mixing behavior in chemical reactors can be made when the residence time distribution (RTD) in the reactors is known (Nauman, 2004). The RTD can be determined from tracer injection and response experiments (Levenspiel, 1999, Thyn et al., 2004, Rothfeld et al., 1963, Anderson, 2012, Danckwerts et al., 1954, Danckwerts, 1953), and has been characterized for different reactors like microchannel reactors (Thulasidas et al., 1999), foam packed trickle flow reactors (Saber et al., 2012), annular centrifugal extractors (Deshmukh et al., 2008), and the rotating disc reactor (Jin Kim et al., 1984). In this chapter a single phase model for a rotor-stator spinning disc reactor (SDR) is presented which is based on residence time distribution measurements. The SDR consists of a rotating disc (rotor) with two stationary discs (stators). The rotor and stators are located at low axial clearance, typically in the range of millimeters. The configuration is schematically shown in **Figure 1.**

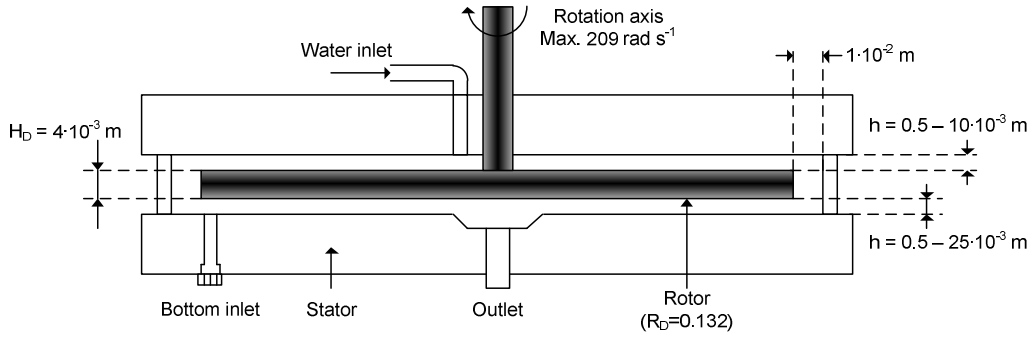

Figure 1. Schematic side view of the rotor-stator spinning disc reactor. The reactor volume equals $167 \cdot 10^{-6}$ m³ at $h=1.0 \cdot 10^{-3}$ m, $299 \cdot 10^{-6}$ m³ at $h=2.0 \cdot 10^{-3}$ m and $431 \cdot 10^{-6}$ m³ at $h=3.0 \cdot 10^{-3}$ m. The rotor radius equals 0.132 m.

Due to the difference in rotational disc speed, a velocity gradient is present between the rotor and the stators, causing a high shear force to act on the fluid between the rotor and stators. For liquid-liquid, liquid-solid, and gas-liquid mixtures, this results in a large interfacial area and an increase of the turbulence intensity, which yields mass transfer rates up to 20 times higher than those measured for conventional multiphase reactors (Meeuwse et al., 2010a, Visscher et al., 2012d, van der Schaaf et al., 2011, Meeuwse et al., 2011, Meeuwse et al., 2010b, Visscher et al., 2012b). The gas-liquid mass transfer rate was described by a model which is based on a combination of ideally stirred tanks and plug flow (Meeuwse et al., 2009). Multiple discs were mounted on a single rotational axis in order to obtain ideally stirred tanks in series, which ultimately will lead to more plug flow behavior of the fluid flow in the reactor (Meeuwse et al., 2012, Danckwerts, 1953). Therefore this reactor is a promising tool to achieve process intensification goals, e.g. realize a reduction of equipment volume, enhance volumetric productivity, and increase of mass transfer rates in continuous flow reactors.

This chapter presents the residence time distribution in the rotor-stator spinning disc reactor as a function of the rotational disc speed, axial disc spacing, and the volumetric flow rate. Based on the RTD measurements, a single phase reactor model is described as the combination of a plug flow model and a number of tanks-in-series. With the RTD known, the feasibility of industrial implementation can be evaluated (Mohammadi et al., 2012).

2.2. Experimental section

2.2.1. Materials

Demineralised water was used for all experiments. The water was demineralized with a Millipore Elix UV-10. Pelikan® Royal Blue fountain pen ink was used as a tracer for the water phase and supplied by BETO Schoolartikelen. All experiments were performed at ambient lab temperature, 292 ± 2 K.

2.2.2. Experimental set-up

The rotor-stator spinning disc reactor was previously described by Meeuwse et al., (**Figure 1**) (Meeuwse et al., 2011). The stationary reactor wall has an inner radius of 0.145 m. The top stator and the rotor are made of stainless steel. The bottom stator is made of poly(methyl methacrylate) (PMMA) for visualization purposes. The rotor is made of stainless steel and has an outer radius of 0.135 m and a thickness of $4 \cdot 10^{-3}$ m. The spacing between the rotor and the stators, further denoted as disc spacing, is equal for the top and bottom stator and can be adjusted by changing the height of the stators. The applied disc spacings are $h=1.0 \cdot 10^{-3}$ m, $h=2.0 \cdot 10^{-3}$ m, and $h=3.0 \cdot 10^{-3}$ m. The rotational disc speed ranged from 50 to 2000 RPM. The water flow rate, Q, ranged from $7.5 \cdot 10^{-6}$ m^3 s^{-1} to $22.5 \cdot 10^{-6}$ m^3 s^{-1}, and was controlled by a CORI-FLOW® M55 mass flow controller from Bronkhorst®. All operational data were acquired through LabView 9. The heat dissipated due to the shear forces in the reactor was removed by precooling the water, using a Lauda WKL-1200 cooling system with ethylene glycol as coolant. The complete set-up is schematically shown in **Figure 2**.

2.2.3. Tracer

Ink was injected by a $25 \cdot 10^{-6}$ m^3 Cetoni® Nemesys Syringe pump, through a ¼" Swagelok® T-piece at $70 \cdot 10^{-3}$ m from the reactor inlet. At $30 \cdot 10^{-3}$ m after the injection point a ¼" stainless steel in-line UV-VIS flow cell from Avantes® was connected, with an optical path length of $5 \cdot 10^{-3}$ m. At $30 \cdot 10^{-3}$ m below the reactor outlet a ½" in-line flow cell from Avantes® was connected with an optical path length of $10 \cdot 10^{-3}$ m. A dual channel AvaSpec-2048-USB2 UV-VIS spectrophotometer was used, which was equipped with an AvaLight-DH-S light source. Lamp, spectrofotometer and flow cells were connected through $600 \cdot 10^{-6}$ m diameter fibers, with a solar resistant coating. The total volume of the inlet and outlet tubing is equal to $4.3 \cdot 10^{-6}$ m^3 s^{-1}. The absorbance of the Pelikan Royal Blue ink was measured at 306 nm. A calibration curve was made to ensure that linear range of Lambert-Beer's law was obeyed.

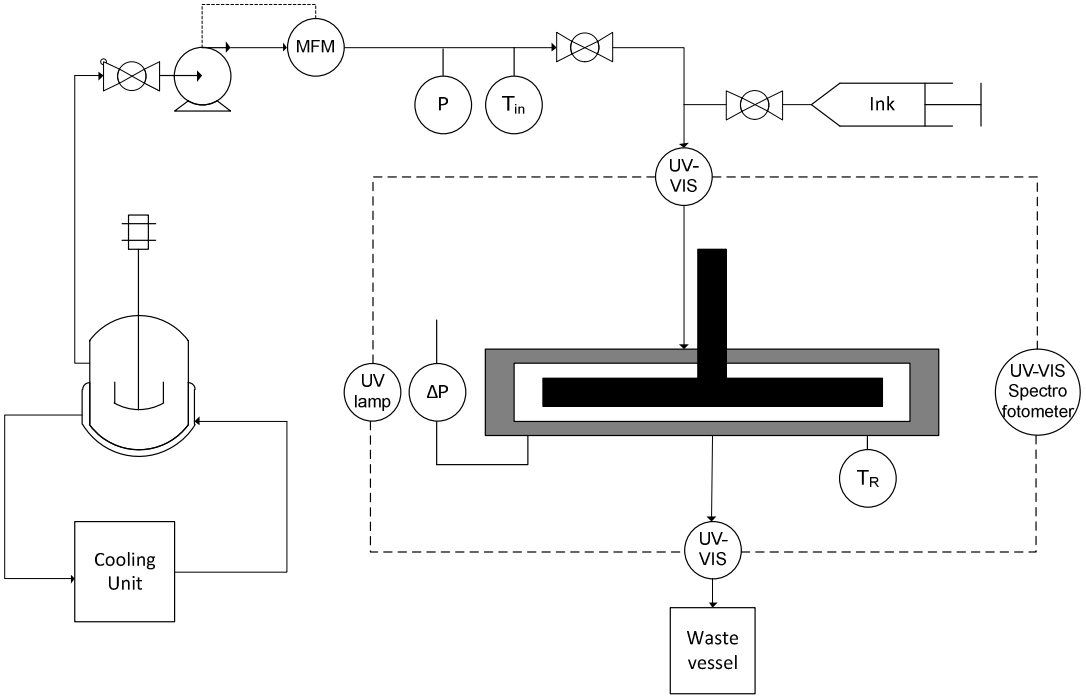

Figure 2. Experimental set-up with all additional equipment. All tubing is made out of ¼" Swagelok tubing. All operational data is controlled and monitored through a LabView® application. Data work up is done through MatLab®.

The applied pulse (injected volume $50 \cdot 10^{-9}$, $100 \cdot 10^{-9}$, and $200 \cdot 10^{-9}$ m³, and injection rate $50 \cdot 10^{-9}$, $100 \cdot 10^{-9}$, and $200 \cdot 10^{-9}$ m³ s^{-1}), were examined to ensure reproducible injections with an optimal Dirac character, in which peak tailing was minimized. All tracer injections were performed by injecting $200 \cdot 10^{-9}$ m³ ink at $200 \cdot 10^{-9}$ m³ s^{-1}.

The tracer injection took place over a period which is short compared with residence times of the reactor, i.e. less than 4%. At each experimental condition two successive injections were performed. Data from successive measurements was collected through LabView® every 0.50 seconds during the period of successive measurements, and analyzed using MatLab®. A standard MatLab® routine was used to separate successive measurements, which separates measurements based on a minimal time difference between peaks, minimum height difference in peaks, and a minimum height between peaks. Equation (1) shows how the residence time distribution function, E(t), is calculated from the tracer concentration at the reactor outlet.

$$E(t) = \frac{C(t)}{\int_0^\infty C(t)\,dt} \tag{1}$$

The integral in the denominator of equation (1) is calculated through trapezoidal numerical integration. The limits of the integration interval are deduced from the maximum absorbance and the average base line absorbance of the outlet signal.

The integration interval is calculated for each separate measurement. The lower integration limit of the integral in equation (1) is given by the last time step before the maximum absorbance in the outlet signal, at which the absorbance is equal to the average baseline absorbance.

The upper integration limit is given by the first time step after the maximum absorbance in the outlet signal is detected, at which the absorbance is at the baseline absorbance. When the integration interval exceeds 6 times the residence time ($\tau = V_R/Q$), the measurement is discarded to prevent tailing dominated measurements (Torres et al., 1998, Boskovic et al., 2008, Cengroš et al., 1995, Martin, 2000). Less than 2% of the measurements were discarded.

2.3. Results and discussion

2.3.1. Tracer detection

Between two injections, at least 10 seconds of steady state signal at the absorbance baseline level was awaited, to ensure a good distinction between the consecutive measurements. The measured absorbance at the inlet and outlet is given in **Figure 3**.

The injection of the tracer causes a sharp increase of the tracer concentration at the reactor inlet. Only one peak is observed after tracer injection, thus channeling is absent. From **Figure 3** it is concluded that the reactor can be modeled as a plug flow volume in combination with a mixed volume.

The plug flow volume is further denoted as V_{PFR}, the mixed volume as V_{CSTR}. The corresponding residence times equal τ_{PFR} (= V_{PFR} Q^{-1}) and τ_{CSTR} (= V_{CSTR} Q^{-1}), respectively. The residence time of the plug flow volume, τ_{PFR}, is calculated from the difference between the points in time at which the tracer is first detected at the reactor inlet and outlet, respectively.

2.3.2. Plug flow volume

The SDR can be modeled as a combination of a plug flow volume with a mixed volume, as is shown in **Figure 4A**. V_{PFR} originates from the volume of the reactor where the radial liquid velocity profile between the rotor and the stator is dominated by the through flow of the liquid phase. The transition is shown in **Figure 4B**. When the through flow is dominating the velocity profile, in laminar conditions the radial liquid velocity profile has a parabolic shape over the height between the rotor and the stator. This is shown in **Figure 4C**.

V_{PFR} is shown as a function of the rotational disc speed, for the measurements at $h=1.0\cdot10^{-3}$ m in **Figure 5A**. For all investigated flow rates, i.e. $7.5\cdot10^{-6}$ m^3 s^{-1}, $15.0\cdot10^{-6}$ m^3 s^{-1}, and $22.5\cdot10^{-6}$ m^3 s^{-1}, it is decreasing with the rotational disc speed. The decrease is small, i.e. 6% for $Q=22.5\cdot10^{-6}$ m^3 s^{-1}, 7% for $Q=15.0\cdot10^{-6}$ m^3 s^{-1}, and 5% for $Q=7.5\cdot10^{-6}$ m^3 s^{-1}.

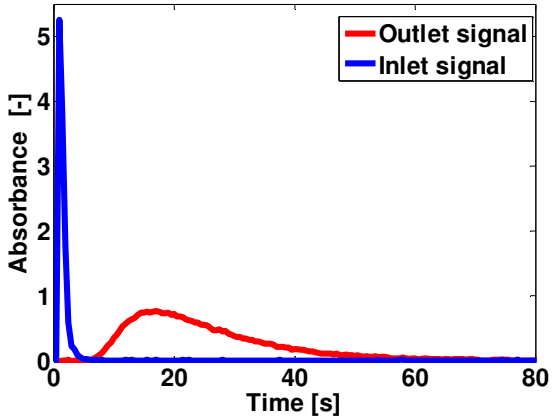

Figure 3. The measured absorbance at the inlet and outlet signal is shown for a pulse, under the experimental condition Q=7.5·10^{-6} m^3 s^{-1}, Ω=250 RPM, and h=1.0·10^{-3} m.

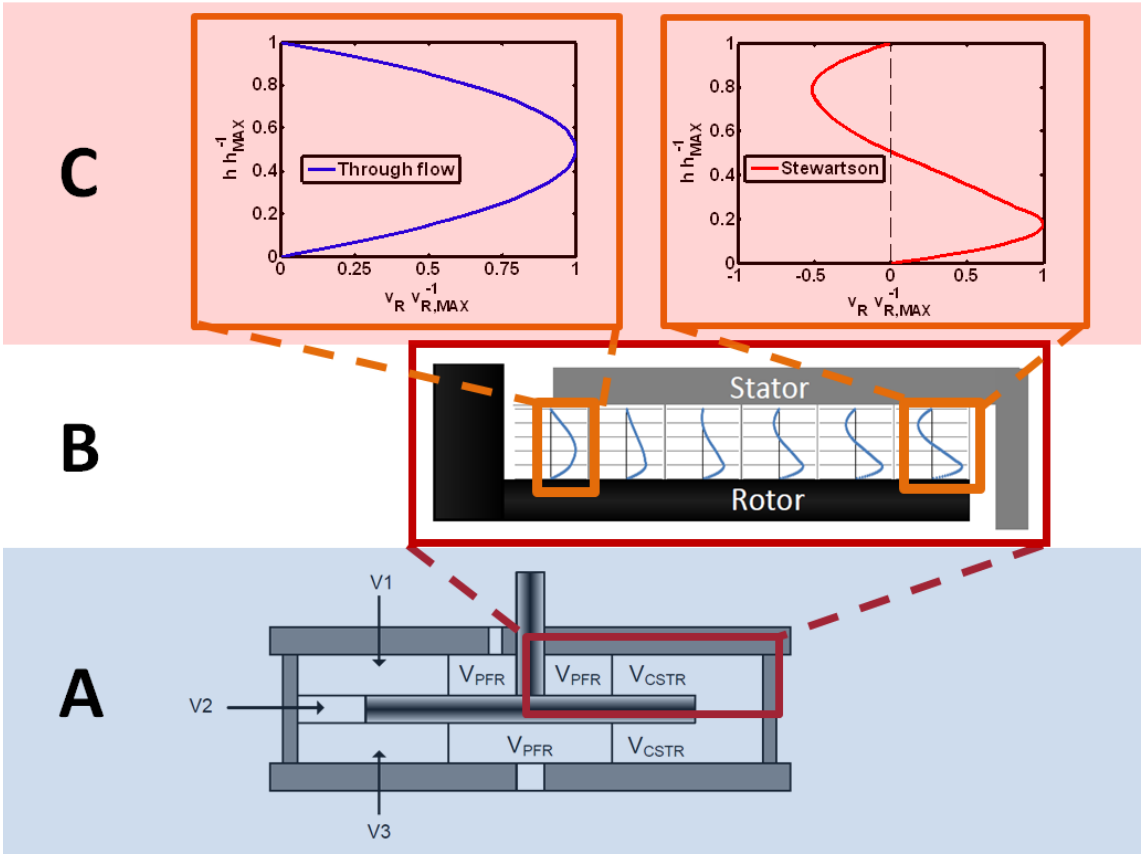

Figure 4. A. Reactor model which described the single phase fluid flow in the spinning disc reactor. B. The transition of the though flow governed radial velocity profile to the boundary layer governed radial velocity profile. C. The through flow and boundary layer governed radial liquid velocity profiles for the case of laminar flow.

V_{PFR} increases with an increase of the flow rate. At 250 RPM, V_{PFR} increases from $75 \cdot 10^{-6}$ m^3 at $7.5 \cdot 10^{-6}$ m^3 s^{-1} to $110 \cdot 10^{-6}$ m^3 at $22.5 \cdot 10^{-6}$ m^3 s^{-1}. As a percentage of the total reactor volume this equals an increase of 45% at $7.5 \cdot 10^{-6}$ m^3 s^{-1} to 64% at $22.5 \cdot 10^{-6}$ m^3 s^{-1}. V_{PFR} is shown as a function of the rotational disc speed, for the measurements at h=$2.0 \cdot 10^{-3}$ m in **Figure 5B**.

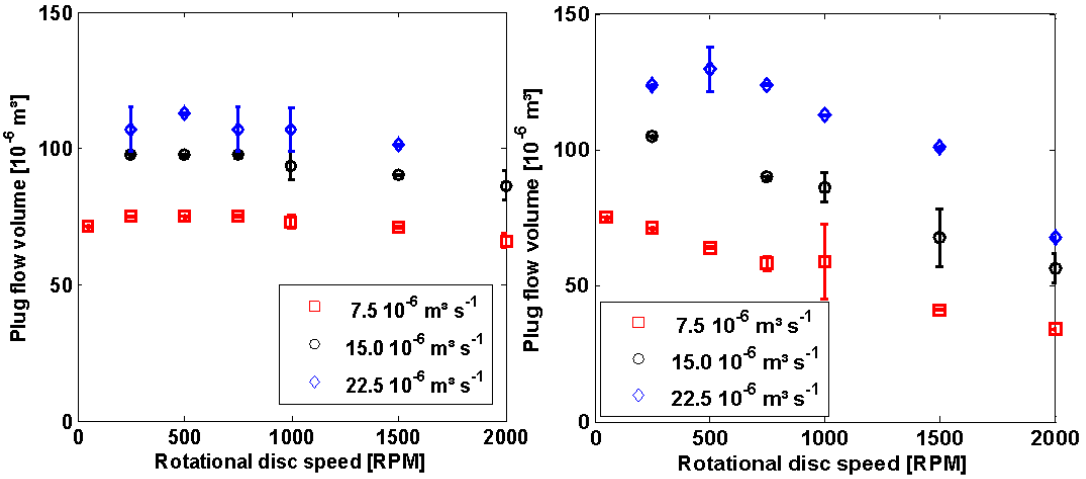

Figure 5. A, left: Plug flow volume versus the rotational disc speed at a disc spacing of $1.0 \cdot 10^{-3}$ m, for different volumetric flow rates. B, right: Plug flow volume versus the rotational disc speed at a disc spacing of $2.0 \cdot 10^{-3}$ m, for different volumetric flow rates.

As observed for h=$1.0 \cdot 10^{-3}$ m, the plug flow volume decreases as a function of the rotational disc speed, whereas it increases with increasing flow rate. The V_{PFR} decrease as a function of the rotational disc speed is larger for the measurements at h=$2 \cdot 10^{-3}$ m than those for h=$1 \cdot 10^{-3}$m. The decrease of V_{PFR} equals 46% for Q=$22.5 \cdot 10^{-6}$ m^3 s^{-1}, 47% for Q=$15.0 \cdot 10^{-6}$ m^3 s^{-1}, and 53% for Q=$7.5 \cdot 10^{-6}$ m^3 s^{-1}.

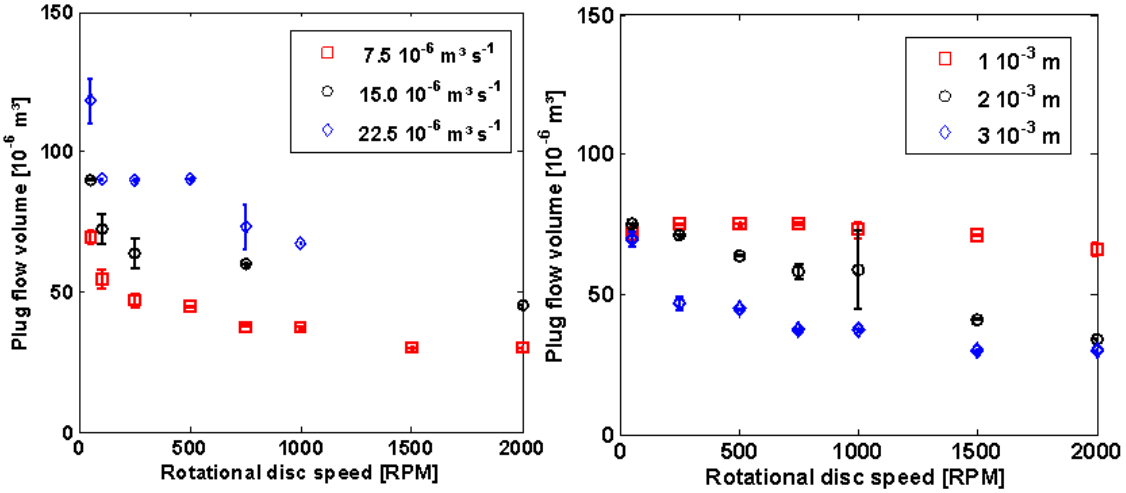

Figure 6. A, left: Plug flow volume versus the rotational disc speed at a disc spacing of $3.0 \cdot 10^{-3}$ m, for different volumetric flow rates. B, right: Plug flow volume versus the rotational disc speed at a volumetric flow rate of $7.5 \cdot 10^{-6}$ m^3 s^{-1}, for varying disc spacings.

V_{PFR} increases with an increase of the flow rate. At 250 RPM, V_{PFR} increases from $71 \cdot 10^{-6}$ m^3 at $7.5 \cdot 10^{-6}$ m^3 s^{-1} to $120 \cdot 10^{-6}$ m^3 at $22.5 \cdot 10^{-6}$ m^3 s^{-1}. As a percentage of the total reactor volume this equals an increase of 24% at $7.5 \cdot 10^{-6}$ m^3 s^{-1} to 41% at $22.5 \cdot 10^{-6}$ m^3 s^{-1}.

Figure 6 shows V_{PFR} as a function of the rotational disc speed, for measurements at $h=3.0 \cdot 10^{-3}$ m. For the disc spacings $h=1.0 \cdot 10^{-3}$ m, $h=2.0 \cdot 10^{-3}$ m and $h=3.0 \cdot 10^{-3}$ m, V_{PFR} is shown as a function of the rotational disc speed in **Figure 6** for measurements performed at $Q=7.5 \cdot 10^{-6}$ m^3 s^{-1}. The decrease in V_{PFR} is strongest for the largest disc spacing.

2.3.3. Transition of plug flow to mixed volume

The SDR can be modeled as a combination of a plug flow volume, V_{PFR}, with a mixed volume, V_{CSTR}. V_{PFR} originates from the through flow governed radial liquid velocity profile. In the mixed volume the radial velocity profile of the liquid is dominated by boundary layer formation. In a rotor-stator configuration two boundary layers exist. The centrifugal von Kármán boundary layer is present at the rotor (von Kármán, 1921). The centripetal Bödewadt boundary layer is present at the stator (Bödewadt, 1940).

The boundary layers are merged for small axial disc spacings (van Eeten et al., 2012). For larger axial disc spacings, these boundary layers are separated by a core with a constant angular velocity, as was suggested by Batchelor (Batchelor, 1951). Daily and Nece identified four single phase flow profiles, depending on the rotational disc speed and the disc spacing (Stewartson, 1953*,* Daily et al., 1960*,* Djaoui et al., 1998). The flow is laminar (Regimes I & II) or turbulent (Regimes III & IV) with either merged boundary layers (Regimes I & III), or with a central core between the boundary layers (Regimes II & IV).

This SDR is always operated in the turbulent regime where boundary layers are merged, i.e. regime III (Djaoui et al., 1998). The transition of laminar flow to turbulent flow in absence of through flow, for the merged boundary layers regime was studied by Cros et al., (Cros et al., 2003*,* Cros et al., 2002*,* Schouveiler et al., 2001). The regime with turbulent flow with merged boundary layers was extensively investigated by Haddadi & Poncet (Haddadi et al., 2008). Boundary layer formation in rotor-stator configurations is determined by the rotational disc speed, Ω (Itoh et al., 1992), disc radius, R, kinematic viscosity, υ, the axial clearance between the rotor and the stators, h (Poncet et al., 2005b), and the superimposed through flow, Q (Poncet et al., 2005a). Also the pre-rotation of the liquid (Debuchy et al., 2010), and the presence and spacing of a cylindrical enclosure are important (Cheah et al., 1994).

Owen and Rogers report that with radial centripetal or centrifugal through flow, near the axis boundary layers break down, and that a through flow governing flow profile remains (Owen et al., 1989). This is consistent with the experimental findings of Haddadi & Poncet (Haddadi et al., 2008). When the centrifugal von Kármán and centripetal Bödewadt boundary layers are fully developed, the parabolic shape of the radial velocity profile is broken down. Both the experimental and modeling results of Haddadi et al., illustrate that the volumetric through flow in the stator boundary layer increases when the rotational Reynolds number is increased from $1.8 \cdot 10^5$ to $5.0 \cdot 10^6$ (Haddadi et al., 2008).

The increase of the radially inward oriented flow in the boundary layer on the stator causes an increase of back mixing and thus a decrease of V_{PFR}. The disc radius where the boundary layer breaks down the flow profile that is governed by through flow depends on the through flow, disc spacing and the rotational disc speed. With an increase of the rotational disc speed, the boundary layer formation is developed closer to the rotational axis. This explains the decrease of V_{PFR} as a function of the rotational disc speed. When, as an approximation, a constant radial velocity profile of the liquid is assumed over the reactor height, the radial liquid velocity is given by equation (2):

$$v_r = \frac{Q}{2\pi R h} \tag{2}$$

According to equation (2), for a through flow of $7.5 \cdot 10^{-6}$ m^3 s^{-1}, the liquid velocity at the entrance, i.e. $R = 26 \cdot 10^{-3}$ m, is more than 5 times higher than at the rim of the disc, i.e. $R = 0.135$ m. At a fixed rotational disc speed and disc spacing, for higher volumetric through flow, the liquid velocity is increased. This leads to an increase of the volume where the boundary layer is suppressed and the through flow is dominating the velocity profile.

Thus V_{PFR} increases. This is in accordance with the trends observed in **Figure 5** and **Figure 6**. Equation (2) also shows that the radial velocity of the liquid decreases when the disc spacing is increased. This decrease in radial liquid velocity implies that the through flow governed profile is broken down at a radius closer to the rotational axis. This means that V_{PFR} decreases.

2.3.4. Mixed volume

The normalized RTD-function is used to describe and compare the mixed volume of different reactors: $E(\theta) = t_m E(t)$, where t_m is the mean residence time and θ the dimensionless time, $t\ t_m^{-1}$. The mean residence time and the variance, σ, around this mean are given by equations (3) and (4). The limits of the integration interval are equal to those used for equation (1) .

$$t_m = \int_0^\infty t\,E(t)\,dt \tag{3}$$

The E(θ)-curve for N tanks-in-series, with equal volumes V_{TANK}, is given by equation (5) (Levenspiel, 1999).

$$\sigma^2 = \int_0^\infty (t-t_m)^2\,E(t)\,dt \tag{4}$$

$$E(\theta) = \frac{N^N \theta^{N-1}}{(N-1)!} e^{-N\theta} = \frac{N^N\,\theta^{N-1}}{\int_0^\infty z^{N-1} e^{-z} dz} e^{-N\theta} \tag{5}$$

The E(θ)-curve of the mixed volume is shown in **Figure 7**, together with a fit of two tanks-in-series with equal volumes. The sum of τ_{PFR} and t_m was compared with the residence time ($\tau = V_R/Q$). Over all measurements, the resulting volume accounted for at least 94% of the total reactor volume. This difference could be caused by a dead volume, as has been observed for the annular centrifugal extractor (Schuur et al., 2012). Such a dead volume can occur due to a non-ideality in the pulse, or due to a stagnant zone which could be located at the point where the horizontal bottom stator is attached to the vertical cylindrical housing.

The error bars in **Figure 5** and **Figure 6**.represent the standard deviation in V_{PFR}. This standard deviation is calculated from the duplicate experiments, and was less than 10% for most measurements, indicating that the experimental approach leads to reproducible results. The number of tanks-in-series, N, with equal volumes can be determined from the variance in equation (4), the mean residence time in equation (3) through equation (6). Increasing the upper integration limit of equation (1) with 0.5τ results in a value of N which is 6% higher. The error due to the integration limit of equation (1) is thus smaller than the reproducibility of the duplicate measurements, and is thus negligible.

$$N = \frac{t_m^2}{\sigma^2} \tag{6}$$

2.3.5. Number of tanks-in-series

The number of tanks-in-series needed to describe the mixed volume for $h=1.0\cdot10^{-3}$ m and for $h=2.0\cdot10^{-3}$ m and for $h=3.0\cdot10^{-3}$ m is shown in **Figure 8.** For all disc spacings, the number of tanks-in-series is not dependent on the rotational disc speed. To model the mixed volume of the reactor, 2 to 3 tanks-in-series are needed. This can be understood when the mixed volume in the reactor is described as three tanks-in-series. This model is schematically shown in **Figure 4A**.

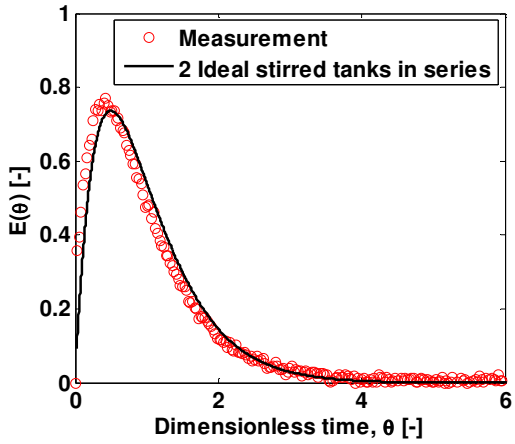

Figure 7. The E(θ)-diagram of the mixed volume of the outlet signal in Figure 3 is given, together with the fit of the two tanks-in-series model (t_m=17.08 s, τ_{PFR}=5.21 s, τ=22.3 s).

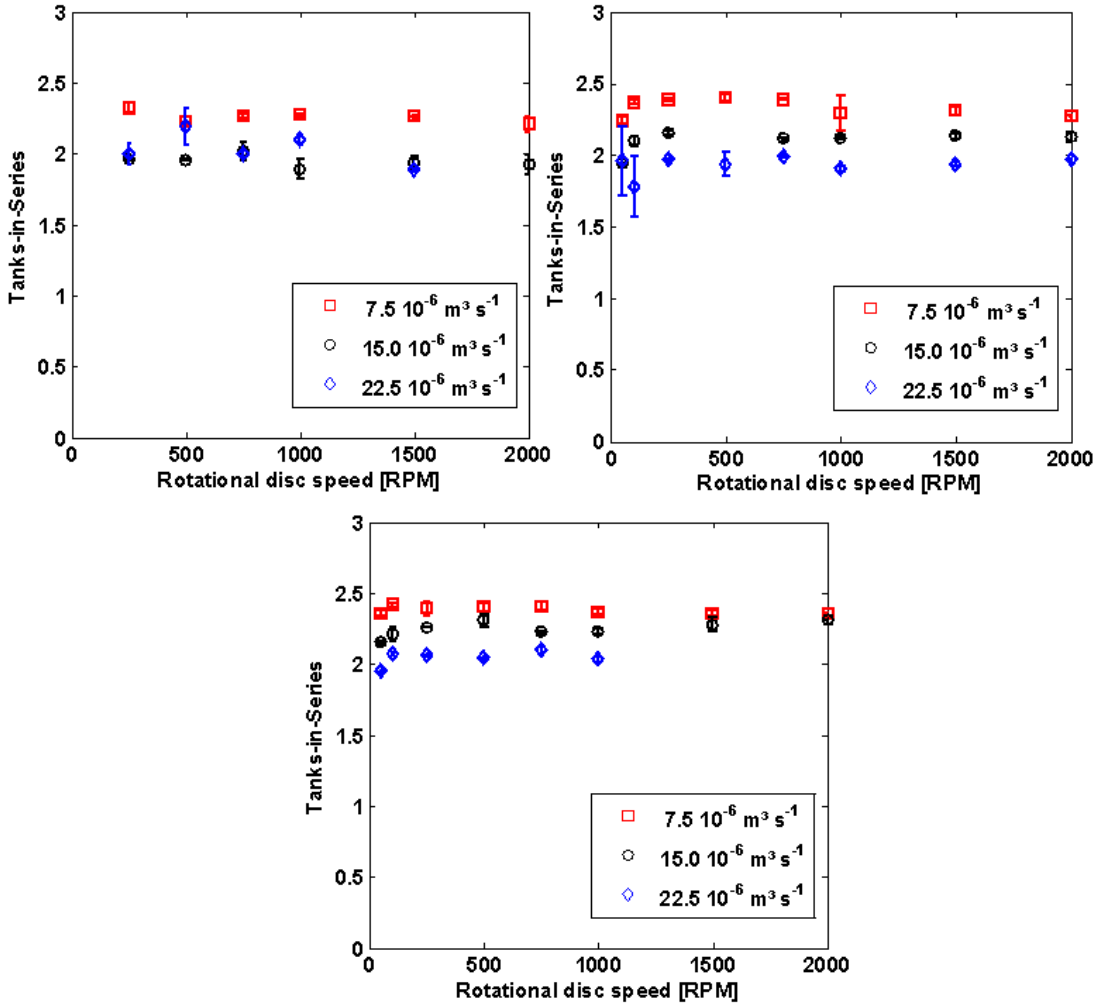

Figure 8. Top left: Number of tanks-in-series versus the rotational disc speed at a disc spacing of $1.0 \cdot 10^{-3}$ m, for different volumetric flow rates. Top right: Number of tanks-in-series versus the rotational disc speed at a disc spacing of $2.0 \cdot 10^{-3}$ m, for different volumetric flow rates. Bottom: Number of tanks-in-series versus the rotational disc speed at a disc spacing of $3.0 \cdot 10^{-3}$ m, for different volumetric flow rates.

One tank is located between the rotor and the top stator (V1). The next tank is formed by the volume aside of the rotor (V2). The last tank is located between the rotor and the bottom stator (V3). For all measurements, the number of tanks-in-series is largest at the lowest flow rate.

For an increasing volumetric flow rate, the interaction of the volumes V1 and V3 with the tank next to the rotor, V2 is increased. Accordingly the influence of V2 decreases, causing the decrease in the number of tanks-in-series with increasing flow rate. The radial position where boundary layer development starts to dominate the radial liquid velocity profile does not change the number of tanks-in-series. Therefore the number of tanks-in-series is not a function of the rotational disc speed.

2.4. Conclusions

This chapter described a reactor model based on single phase residence time distribution measurements in a rotor-stator spinning disc reactor. Measurements are based on the pulse wise injection of a tracer. For the validation of the model the disc spacing between the rotor and the stators was varied from $1.0 \cdot 10^{-3}$ to $3.0 \cdot 10^{-3}$ m, the rotational disc speed was varied from 50 to 2000 RPM, and the volumetric flow rate was varied from $7.5 \cdot 10^{-6}$ to $22.5 \cdot 10^{-6}$ m^3 s^{-1}.

The resulting reactor model consists of a plug flow model in combination with a number of tanks-in-series. The volume of the reactor which can be described by a plug flow model decreases as a function of rotational disc speed. This volume increases with the volumetric flow rate. The mixed volume is described as 2 to 3 tanks-in-series with equal volumes which is determined through the mean residence time and the variance of the RTD curve. This can be understood by assuming the volume above and below the rotor as an ideally mixed volume, in combination with a third ideally mixed volume at the rim of the reactor. The reactor model is explained with the development of turbulence, the formation of von Kármán and Bödewadt boundary layers, and the effect of volumetric flow rates.

Nomenclature

Roman symbols

C	Tracer concentration, mol m^{-3}
E	Residence time function, -
h	Disc spacing, m
N	Number of tanks-in-series with equal volume, -
n	Number of measurement point in RTD-curve,-
Q	Volumetric flow rate, $m^3\ s^{-1}$
R	Rotor radius, m
Re_Ω	Reynolds number, $2\pi(60)^{-1}\Omega R^2 v^{-1}$,-
t	Time, s
t_m	Mean residence time, s
V	Volume of fluid, m^3
v	Radial liquid velocity, m s^{-1}
z	Arbitrary integration variable,-

Greek letters

θ	Dimensionless time, $t\ t_m^{-1}$,-
σ	Variance, -
τ	Residence time, s
υ	Kinematic viscosity, $m^2\ s^{-1}$
Ω	Rotational disc speed, RPM

Sub- and superscripts

CSTR	Continuous Stirred-Tank Reactor
IN	Inlet
PFR	Plug Flow Reactor
R	Reactor
r	Radius

3. Liquid-liquid volume fractions in a rotor-stator spinning disc reactor

This chapter has been published as:

Visscher, F., Bieberle, A., Schubert, M., van der Schaaf, J., de Croon, M.H.J.M., Hampel, U., Schouten, J.C., "**Water and *n*-heptane volume fractions in a rotor-stator spinning disc reactor",** *Industrial & Engineering Chemistry Research*, 2012, 51 (51), pp. 16670-16676.

Abstract

This chapter presents the volume fractions of *n*-heptane and water measured in a rotor-stator spinning disc reactor. The volume fractions were measured using γ-ray tomography and photographic image analysis. The volume fractions were determined as a function of rotational disc speed, flow ratio, position in the reactor, and rotor material. In addition, the effect of the density difference between water and *n*-heptane was determined by dissolving potassium iodide in the water phase. Below a rotational disc speed of 75 RPM the volume fraction measured by tomography and photographic image analysis are within 10% deviation. For low rotational disc speeds, the *n*-heptane volume fraction decreases slightly with increasing rotational disc speed: the centrifugal force accelerates the larger *n*-heptane droplets to the center. At higher rotational disc speeds the droplets become smaller accordingly, the friction between the phases determines the flow and the *n*-heptane volume fraction becomes equal to the *n*-heptane to total flow ratio. An increase in density difference from 0.31 to 0.79 kg dm^{-3} did not influence the volume fractions.

3.1. Introduction

Liquid-liquid extraction and reactive extraction are generally performed in multiphase equipment such as stirred tanks (Hemrajani et al., 2004), packed columns (Jaradat et al., 2011, Su et al., 2010), or rotating disc columns (Al-Rahawi, 2007, Soltanali et al., 2009). The performance of multiphase extraction equipment is dominated by the mass transfer rate. One example of intensified equipment is the rotor-stator spinning disc reactor (SDR). The gas-liquid, liquid-solid, and liquid-liquid mass transfer rates in the SDR are higher when compared to conventional reactors (van der Schaaf et al., 2011, Visscher et al., 2012d). The SDR consists of a rotating disc which is mounted at a small axial distance from the stationary discs (**Figure 1).**

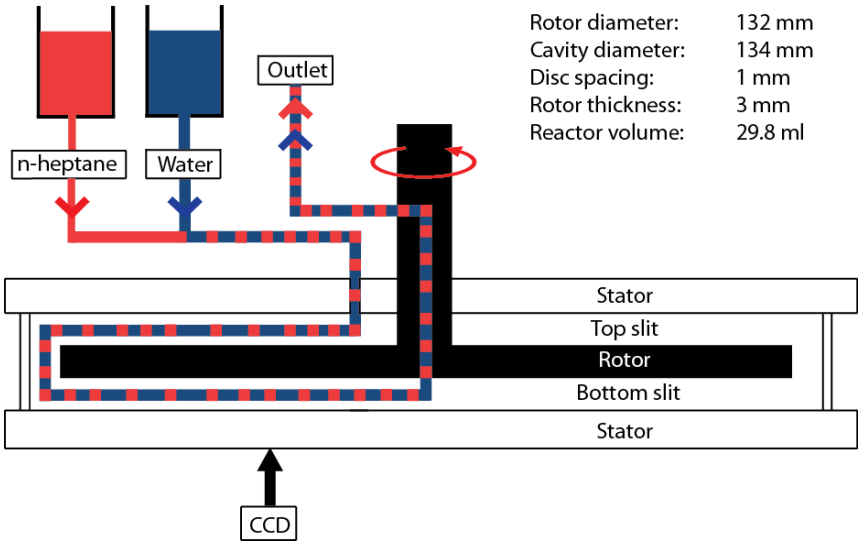

Figure 1. Schematic representation of the rotor-stator spinning disc reactor. The difference in rotational speed between the rotor and the stator induces a shear stress that disperses the liquids inside the reactor.

The axial distance between the rotor and the stator is typically in the order of 1 10^{-3} m. The difference in rotational disc speed over this small disc spacing induces a strong shear force that acts on the liquids in the reactor. This shear force leads to a fine dispersion of the liquids in the reactor. In this dispersion, a high interfacial area is generated. Combined with the turbulence intensity this leads to high liquid-liquid mass transfer rates. For liquid-liquid processes, the volume fraction and the droplet size determine the specific surface area and thus the mass transfer rate (Visscher et al., 2012d). The volume fraction is also essential for safety analysis of a reactor when hazardous chemicals are mixed (Krishna et al., 1994).

In this chapter, the liquid-liquid volume fractions are measured inside a rotor-stator spinning disc reactor using γ-ray computed tomography, with water as aqueous phase and *n*-heptane as organic phase. The organic phase volume fraction is measured in the volume between the rotor and the top and bottom stators, respectively. First, the observed flow patterns in the reactor are described.

Next, the volume fraction is characterized as a function of the rotational disc speed and the *n*-heptane to total flow ratio. Also, the influence of the rotor construction material is described. Furthermore, potassium iodide (KI) is added to the aqueous phase to study the effect of the density difference between water and *n*-heptane on the volume fraction inside the SDR. Additionally, the KI enhanced the contrast between the phases for the γ-ray tomography. Finally, the results obtained from γ-ray tomography are compared to the results obtained through photographic image analysis.

3.2. Methods

3.2.1. Determination of the volume fraction

A common method to measure the liquid volume fraction in a reactor is performing a start-stop experiment (Al-Dahhan et al., 1999, Urrutia et al., 1996). Another indirect possibility is to study the residence time distribution (Madhuranthakam et al., 2009). A drawback of these methods is that no spatial information is gained. Especially for rotating systems, where the centrifugal force varies with radial distance, a strong variation of the volume fraction with radial distance is expected.

More detailed information can be obtained with photographic or video image analysis. The analysis of photographic or video images gives a time-resolved, spatial estimation of the volume fraction. The calculated volume fraction is however underestimated, since the resolution of a camera is often insufficient to detect droplets with a diameter of 0.5 10^{-3} m or less. Furthermore, the thickness of the thin films above and below a droplet cannot be resolved. Also conductivity measurements can be used to measure volume fractions (Steiner et al., 1974, Kumar et al., 1986).

In this research, the volume fraction is measured using γ-ray computed tomography (CT). In tomography, penetrating photons are used to visualize cross-sections of a three dimensional object. Examples of penetrating photons are X-rays, γ-rays, and radio frequency waves.

Such photons are non-intrusive to the 3D object. Computed tomography allows to measure the volume fraction inside a reactor (Schubert et al., 2011, Bieberle et al., 2010a). γ-ray tomography does not affect the volume fraction and does not need additional reactor inlets, outlets, or in-situ sensors. Computed tomography is widely used in medical diagnostics, but is only scarcely applied in the field of chemical engineering. For equipment diagnostics in chemical engineering, the use of gamma radiation with photon energies of more than 500 keV is especially attractive because of its ability to penetrate materials with a high atomic number, e.g. steel or aluminum (Hampel et al., 2007).

3.2.2. Tomography measurements

A CT scan makes various radiographic projections from different angular positions around the scanned object from which the density distribution is reconstructed. Rather than rotating the γ-ray CT measurement system as common in medical CT scans, the SDR was continuously rotated over 360°. A schematic overview of the γ-ray CT measurement system is shown in **Figure 2**.

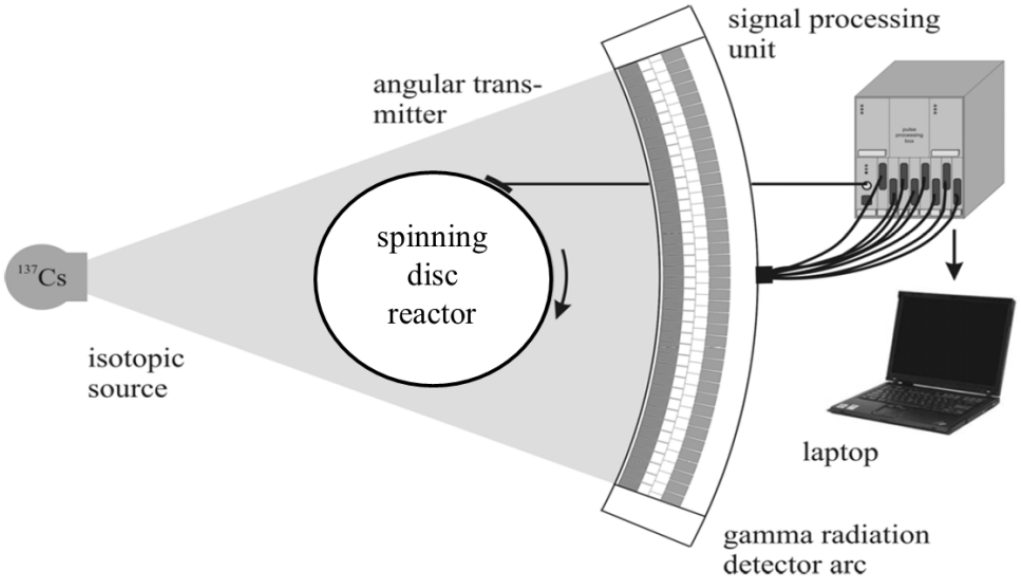

Figure 2. Schematic representation of the computed tomography set-up. The rotor-stator spinning disc reactor is placed on a rotating table. Source and detectors are in a fixed position (Bieberle et al., 2010a).

For every 0.4 degrees a radiographic projection was measured. Hence, a complete CT scan delivers 900 projections. The measuring time was set to 10 minutes for a good material averaging and acceptable radiation statistic, giving a single projection time of about 0.67 s.

3.2.3. Image reconstruction procedure

The result of a computed tomography scan is a so-called sinogram matrix M(d,p) in which the number of counts for each detector *d* is compiled for all 900 projections *p*. Measurements at different flow rates, rotational disc speeds, as well as various ink and KI concentrations lead to liquid-liquid distributions and patterns, and thus different radiation attenuations and also different counting rates in the sinogram matrices occur. To determine volume fraction in a two-phase flow, first two reference states of the SDR are scanned: fully filled with water, M_{aq}, and fully filled with *n*-heptane, M_{org}. Then, two attenuation matrices (E_{MAX} and E_{MEAS}) are calculated from these data, which are the input for CT reconstruction algorithms to obtain two non-superimposed cross-sectional attenuation distributions $\mu_{max}(i,j)$ and $\mu_x(i,j)$ with i and j as matrix/image index.

Here, the filtered back-projection algorithm was used in combination with the Hanning filter (Lyra et al., 2011). The time-averaged local organic volume fraction distribution in the slit, $\varepsilon_{ORG,LOC}$, was determined with equation (3).

$$E_{max}(d,p) = -\log\left(\frac{M_{aq}(d,p)}{M_{org}(d,p)}\right) \quad (1)$$

$$E_{meas}(d,p) = -\log\left(\frac{M_{meas}(d,p)}{M_{org}(d,p)}\right) \quad (2)$$

$$\varepsilon_{ORG,LOC}(i,j) = 1-\left(\frac{\mu_{meas}(i,j)}{\mu_{max}(i,j)}\right) \quad (3)$$

The calculation of the attenuation coefficient and the non-superimposed cross-sectional attenuation distributions is described in more detail elsewhere (Bieberle et al., 2011). An example of a reconstructed scanning plane, with the time-averaged local organic phase volume fraction is shown in **Figure 3**. The local organic volume fraction is averaged over the reactor slit to give the overall volume fraction in the reactor.

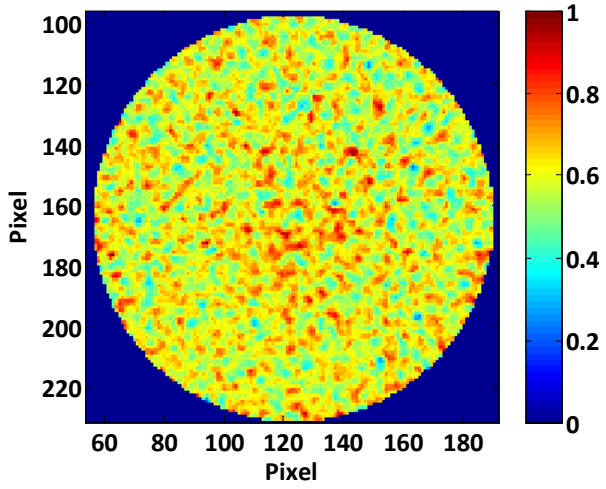

Figure 3. The reconstructed scanning plane image of the reactor, measured at a rotational disc speed of 1000 RPM and Θ = 0.65 m^3_{ORG} : m^3_{TOT}, the colors represent the volume fraction. The mean organic phase volume fraction equals 0.60 m^3_{ORG} m^{-3}_{REAC}.

3.2.4. Photographic image analysis

The flow in the bottom slit of the SDR was digitally recorded by a Canon EOS digital 400D camera with an 18-55 mm EFS lens. All photographs were made via a mirror that was located at a 45° angle below the reactor. The Image Processing Toolbox from Matlab® was used to convert the picture into a black-and-white image. A Matlab® script identified the position of the rotor in the black-and-white image. Water and *n*-heptane were distinguished by a threshold value that was determined automatically by Matlab® for each picture using Otsu's method (Otsu, 1979).

The organic phase volume fraction was estimated by determining the fraction of the surface of the disc where *n*-heptane is present, under the assumption that *n*-heptane droplets completely fill the volume between the rotor and the stators, which results in an overestimation of the organic phase volume fraction. The average volume fraction was determined from ten photographic images for each experimental condition. The error bars represent the standard deviation over ten measurements.

3.3. Experimental section

3.3.1. Set-up

A schematic side view of the SDR set-up is given in **Figure 1**. The cavity of the SDR has an inner diameter of 134 10^{-3} m and is made of poly(methyl methacrylate) (PMMA). This allows visual observation of the flow with a camera. Experiments were performed with a stainless steel rotor and a PMMA rotor. Both rotors are 132 10^{-3} m in diameter. The rotor is located at an axial clearance of 1 10^{-3} m from the stators. The top slit is the space between the rotor and the top stator, the bottom slit is the space between the rotor and the bottom stator. Water and *n*-heptane are premixed in a 3/8" Swagelok T-piece and enter the reactor adjacent to the 10 10^{-3} m wide rotational axis. From the inlet, the liquid flows between the top stator and the rotor towards the volume between the bottom stator and the rotor. From there the liquid mixture flows through a 3 10^{-3} m internal diameter channel inside the rotational axis upwards. This gives an unobstructed view of the entire bottom slit.

Two mechanical seals are used to connect the channel in the rotational axis to a channel in the stationary reactor wall. The total reactor volume is 29.8 10^{-6} m^3. A 200 W DC motor (Maxon) is applied to rotate the shaft by means of a belt driven pulley, up to a maximum rotational disc speed of 1700 RPM. Two M55 Coriolis mass flow controllers (Bronkhorst) were used in combination with two gear pumps (Tuthill). Investigated combinations of flow rates and their ratios are given in **Table 1**.

Table 1. Experimental configurations, with the water flow rate, φ_{AQ}, *n*-heptane flow rate, φ_{ORG} and *n*-heptane to total volumetric flow ratio, Θ, with the units $m^3_{ORG} : m^3_{TOT}$.

PMMA rotor without KI			Stainless steel rotor without KI			Stainless steel rotor with KI		
φ_{AQ} (m^3h^{-1}) /10^3	φ_{ORG} (m^3h^{-1}) /10^3	Θ	φ_{AQ} ($m^3 h^{-1}$) /10^3	φ_{ORG} ($m^3 h^{-1}$) /10^3	Θ	φ_{AQ} ($m^3 h^{-1}$) /10^3	φ_{ORG} ($m^3 h^{-1}$) /10^3	Θ
6.16	7.91	0.56	6.16	7.91	0.56	4.24	7.96	0.65
9.00	8.64	0.49	11.14	7.91	0.42	12.39	7.96	0.39
18.0	7.91	0.31	25.05	7.90	0.24	17.38	7.96	0.31
36.0	7.91	0.18						

3.3.2. Tomography set-up

The organic phase volume fraction within the SDR is determined with the high-resolution γ-ray CT measurement system at the Helmholtz-Zentrum Dresden-Rossendorf, Germany (Bieberle et al., 2010a, Bieberle et al., 2011, Bieberle et al., 2007, Tschentscher et al., 2011, Tschentscher et al., 2012). The γ-ray CT measurement system consists of a collimated isotopic source, a radiation detector arc, a lifting and rotating object table, and an external signal processing unit. As isotopic source Cs-137 with an activity of about 185 GBq and photon energy of 662 keV is used.

The radiation detector arc is positioned 970 10^{-3} m away from the collimated isotopic source, and has a 43° acquisition angle with 320 single detectors. Each of these detectors consists of a scintillation crystal, an avalanche photo diode, and a charge sensitive preamplifier and is operated in pulse mode. Thus, the applied energy discrimination offers very accurate measurements by counting only the non-scattered γ-ray photons (Hampel et al., 2007). The temperature of the entire detector arc is controlled by an external cooling system, which is also important to achieve a high measuring accuracy under varying ambient temperatures (Bieberle et al., 2010b).

The SDR is located onto a rotating table that is placed between the stationary radiation detector arc and the collimated isotopic source such that the radiation fan beam passes through the horizontal scanning plane. The exact location of the slit position between the rotor and the bottom stator was identified by radiographic measurement at different heights covering the entire rotor-stator region. The detector arc was further collimated to a measuring slit height of 2 10^{-3} m by two lead arcs. This ensured a complete covering of the axial clearance of 1 10^{-3} m between the rotor and the stator.

3.3.3. Chemicals

A two-phase system of water and *n*-heptane was selected to study the volume fraction (Visscher et al., 2011, Visscher et al., 2012d). For all experiments, demineralized water was used. Pelikan Royal Blue ink was obtained from BETO Schoolartikelen. *n*-Heptane was obtained at ≥99% purity from Sigma–Aldrich. Potassium iodide was obtained from Merck at 99.5% purity. A stock solution was made by dissolving 4.98 kg KI in 5.5 10^{-3} m^3 of demineralized water. This stock solution was diluted to a solution with a density of 1.45 kg m^{-3}. The density dependence on the concentration of KI is shown in **Figure 4**, and fits the data published by MacInnes et al. and Pawar et al. for very diluted concentrations and at saturation respectively (Pawar et al., 2009, MacInnes et al., 1952). The linear concentration dependency of the aqueous phase density is equal to the trend observed for aqueous solutions of sodium chloride and potassium chloride (Zhang et al., 1996). The effect of the KI concentration on the interfacial tension of water and *n*-heptane is low for KI concentrations below 10 10^{-3} M (Deshpande et al., 2012).

The weight percentage of KI in *n*-heptane was measured by mixing an aqueous KI-solution with *n*-heptane and subsequently drying the *n*-heptane, and found to be less than 0.01 wt%. GC-MS analysis showed that there is no ink dissolved in the *n*-heptane.

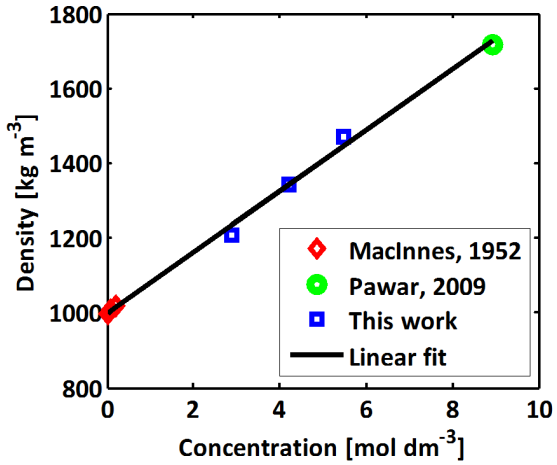

Figure 4. The density of aqueous KI solutions versus the potassium iodide concentration in water. The linear relationship is given by: density = 81.2 x concentration + 998.2.

3.4. Results and discussion

3.4.1. Flow pattern

Figure 5 shows examples of the reconstructed organic phase distribution image at a *n*-heptane to total volumetric flow ratio, Θ, of 0.83 $m^3_{ORG} : m^3_{TOT}$ and a rotational disc speed, N, of 50 RPM together with a photographic image made at 100 RPM. A spiraling behavior is observed for both phases below 150 RPM. In the water spiral, entrained *n*-heptane droplets are present. It was observed that the starting point of the spiral is not constant over various experiments.

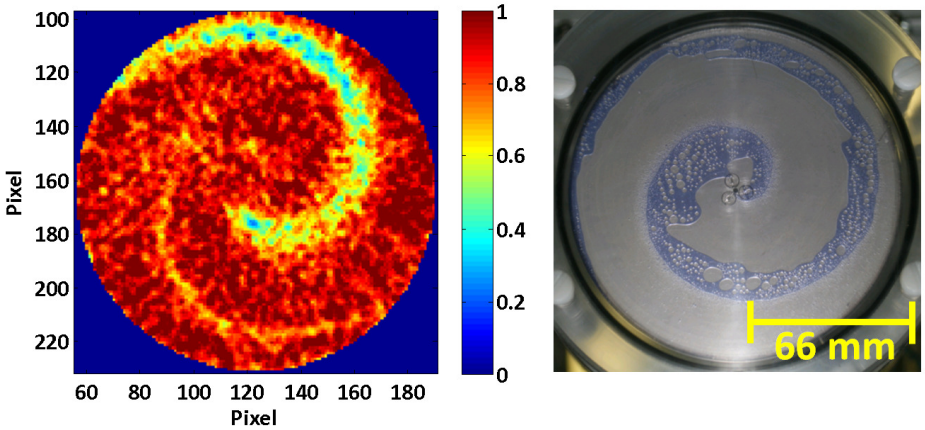

Figure 5. Example of a reconstructed phase distribution (left, SS rotor, φ_{ORG} = 26.4 10^{-6} m^3 s^{-1}, φ_{AQ} = 5.4 10^{-6} m^3 s^{-1}, ratio = 0.83, N = 50 RPM, bottom slit) and an example of a photographic phase distribution image (right, SS rotor, φ_{ORG} = 26.4 10^{-6} m^3 s^{-1}, φ_{AQ} = 5.4 10^{-6} m^3 s^{-1}, ratio = 0.83, N = 100 RPM, bottom slit, and ink added to the aqueous phase). Both show a water spiral in the bottom slit of the reactor.

3.4.2. Rotational disc speed and flow ratio

The effect of the rotational disc speed on the organic phase volume fraction, ε_{ORG}, in the bottom slit is shown as a function of rotor speed in **Figure 6** for the measurements with a PMMA rotor.

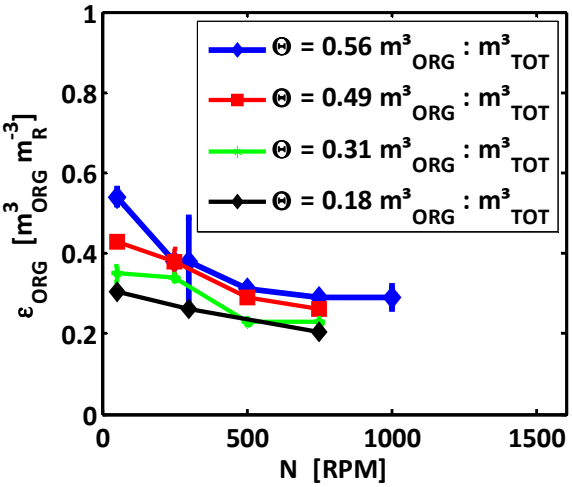

Figure 6. Volume fraction of the organic phase, measured through tomography, with a PMMA rotor. Measurements are made without ink and an aqueous phase density of 0.99 kg dm^{-3}.

Above 150 RPM a radial uniform distribution of the volume fractions is observed; see **Figure 3**. Above 150 RPM the shear stress starts to break up the spiral. The drag force due to the tangential shear stress on the smaller fragments increases and starts dominating the centrifugal force. The winding number for the spiral increases rapidly and leads to a more uniform distribution. Additionally, this also takes place at the top-side of the rotor, which leads to more entry points for the *n*-heptane droplets, thus increasing the uniformity of the dispersion. At all rotational disc speeds, *n*-heptane is the dispersed phase.

ε_{ORG} decreases with rotational disc speed, N, and increases with the *n*-heptane to total volumetric flow ratio, Θ. At 50 RPM and Θ = 0.56 m^3_{ORG} : m^3_{TOT} the difference between ε_{ORG} and Θ is less than 4%. At low rotational disc speeds the difference between ε_{ORG} and Θ is expected to be small. The difference between ε_{ORG} and Θ increases with increasing flow ratio, up to a 75% for Θ = 0.18 m^3_{ORG} : m^3_{TOT}. The flow pattern observed in the bottom slit represents alternating rings with an irregular shape that move radially inwards. With increasing rotational disc speed ε_{ORG} approaches approximately 0.25 m^3_{ORG} m^3_{REAC} for all flow ratios at 750 RPM. Except for Θ = 0.18 m^3_{ORG} : m^3_{TOT}, the asymptotic value of ε_{ORG} is lower than Θ. The organic phase volume fraction is shown as a function of rotational disc speed in **Figure 7** for the measurements with a stainless steel rotor. Up to 500 RPM the organic phase volume fraction, ε_{ORG}, decreases with rotational disc speed, N, and increases with the *n*-heptane to total volumetric flow ratio, Θ.

This was also observed while measuring with the PMMA rotor. Above 500 RPM, opposite behavior was found. ε_{ORG} increases with the rotational disc speed. For Θ = 0.56 m^3_{ORG} : m^3_{TOT}, ε_{ORG} is higher than Θ below 200 RPM. Above 200 RPM ε_{ORG} increases again until it reaches the value of Θ at 1600 RPM. For Θ = 0.24 m^3_{ORG} : m^3_{TOT} an initial decrease of ε_{ORG} is observed with a minimum at 300 RPM. For Θ = 0.24 m^3_{ORG} : m^3_{TOT}, ε_{ORG} is always higher than Θ. The increase of the ε_{ORG} can be explained from the effect of the centrifugal force, F_C, and drag force, F_D, which are given by equations (4) and (5), respectively. The centrifugal force is present due to the rotation of the liquids.

$$F_C = m_{ORG}\, a = \frac{1}{6}\pi d_{ORG}^3 \varrho_{ORG} \omega^2 r \tag{4}$$

$$F_D = \frac{1}{2}\varrho_{AQ} v^2 C_D A_L \tag{5}$$

Due to the density difference and the centrifugal force, the water phase encounters a larger force directed outwards. The radial velocity of *n*-heptane droplets is thus higher. With increasing rotational disc speed the large *n*-heptane droplets break up into smaller droplets due to the increase of the shear stress. Thus the diameter decreases and the number of *n*-heptane droplets increases. As a result the specific surface area of the *n*-heptane droplets increases.

Equation (5) shows that the drag force acts on the *n*-heptane droplets interface that is perpendicular to the flow direction, A_L. Thus the drag force scales with the diameter to the power of 2. Equation (4) shows that the centrifugal force scales with the droplet diameter to the power of 3. As a result, the drag force becomes more dominant for smaller droplets. The radial inward velocity of these droplets decreases. Because more and smaller droplets are generated, and because their radial velocity decreases, the volume fraction increases.

3.4.3. Top and bottom slit

Measurements of ε_{ORG} in the top slit of the reactor, i.e. the volume above the stainless steel rotor, were compared to those in the bottom slit, i.e. the volume below the rotor (**Figure 8).** In both slits, the mean value of ε_{ORG} over the slit is approximately equal. The difference in ε_{ORG} in the top and bottom slit between 0 and 1600 RPM is less than 5% for the measurements at Θ = 0.65 m^3_{ORG} : m^3_{TOT} and Θ = 0.31 m^3_{ORG} : m^3_{TOT}. For co-fed gas-liquid flow, the hydrodynamic regime above and below the rotor was previously reported to be different (Meeuwse et al., 2009). A dispersed regime was observed between the rotor and the bottom stator, a film region was observed in the volume between the rotor and the top stator. For liquid-liquid co-feeding no visual difference is observed for the top and bottom slit. Both slits have a regime in which *n*-heptane is dispersed in the water phase.

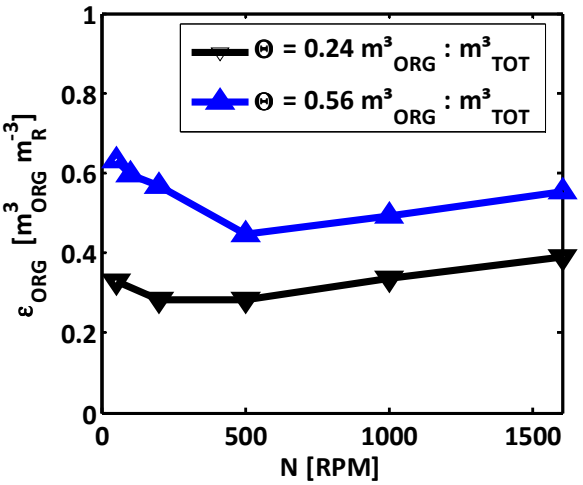

Figure 7. Volume fraction of the organic phase, measured with a stainless steel rotor. Measurements are made without ink and an aqueous phase density of 0.99 kg dm^{-3}.

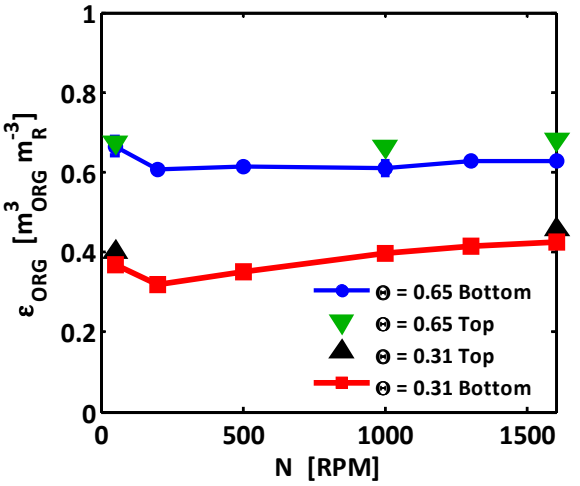

Figure 8. Volume fraction of the organic phase in the top and the bottom slit of the reactor, measured for the stainless steel rotor, low ink concentration and an aqueous phase density of 1.45 kg dm^{-3}.

3.4.4. Rotor material

The influence of the rotor material on the value of ε_{ORG} is shown in **Figure 9**, which shows measurements from **Section 3.4.2**. Both measurements are performed without KI or ink added to the water. The PMMA rotor systematically gives lower values of ε_{ORG} compared to the stainless steel rotor. At 50 RPM this difference is 15%, at 1000 RPM this difference is largest: about a factor 2. For the stainless steel rotor, ε_{ORG} has a minimum of 0.45 m^3_{ORG} m^3_{REAC} at 500 RPM, after which it asymptotically increases to a value of 0.55 m^3_{ORG} m^3_{REAC}. This is close to the theoretical asymptote of Θ = 0.56 m^3_{ORG} : m^3_{TOT}. With the PMMA rotor ε_{ORG} goes asymptotically to a value of 0.29

m^3_{ORG} m^3_{REAC}. The rotational disc speed with the PMMA rotor measurements was limited to 1000 RPM. An increase of ε_{ORG} above 1000 RPM is expected.

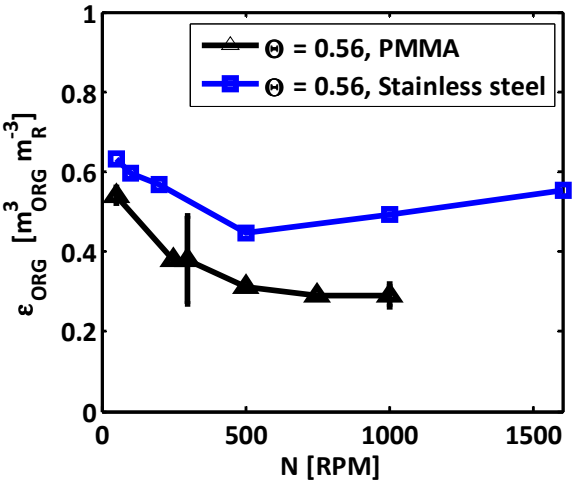

Figure 9. Volume fraction of the organic phase, measured with tomography, for a PMMA rotor and with a stainless steel rotor. Both measurements are made without ink and an aqueous phase density of 0.99 kg dm^{-3}.

3.4.5. Density difference

To study the effect of the density difference between the aqueous phase and the organic phase, KI was dissolved in water. While the density difference for the water/*n*-heptane system is equal to 0.31 kg dm^{-3}, a density difference of 0.79 kg dm^{-3} was adjusted for the system with potassium iodide (here aqueous phase density, ϱ_{AQ}, is equal to 1.45 kg dm^{-3}). The standard deviation of three repetitive measurements is equal for the measurements with and without KI added to the aqueous phase, i.e. less than 5%. **Figure 10** shows ε_{ORG} measured for systems in which the aqueous phase density, ϱ_{AQ}, was increased to 1.45 kg dm^{-3}.

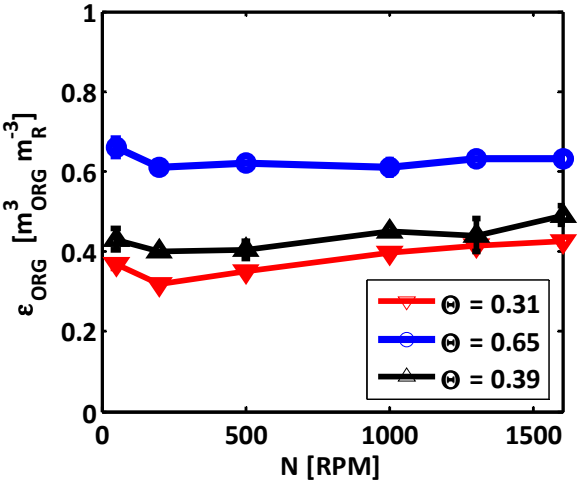

Figure 10. Volume fraction of the organic phase, measured with the stainless steel rotor at low ink concentration and an aqueous phase density of 1.45 kg dm^{-3}.

All measurements were performed with the stainless steel disc and a low ink concentration. Here ε_{ORG} is close to the theoretical value Θ. For Θ = 0.65 m^3_{ORG} : m^3_{TOT}, between 50 and 200 RPM, ε_{ORG} decreases 10%. From 200 to 1600 RPM, ε_{ORG} increases asymptotically towards Θ. For Θ = 0.31 m^3_{ORG} : m^3_{TOT}, the initial decrease of ε_{ORG} also equals 10%, the asymptotic increase however goes to 0.39 m^3_{ORG} m^3_{REAC}, which is 19% above the value of Θ.

The reason for this increase is unclear; a value of ε_{ORG} equal to Θ was expected. Comparing **Figure 7** and **Figure 10** shows that for the measurements with ϱ_{AQ} = 0.99 kg dm^{-3}, the decrease in ε_{ORG} at low rotational disc speed is larger than that for the measurements with ϱ_{AQ} = 1.45 kg dm^{-3}. This can be explained from the influence of the interfacial tension. The interfacial tension of the water-alkane interface increases with the KI concentration (Aveyard et al., 1976*,* Amouei et al., 2008)

This implies that at a lower KI concentration a lower shear force is needed to reduce the droplet diameter. As a result thereof, at a particular rotational disc speed, the droplet diameter is smaller while using ϱ_{AQ} = 1.45 kg dm^{-3} when compared to ϱ_{AQ} = 0.99 kg dm^{-3}. Smaller droplets are more susceptible to the drag force, see Equation (5). For the measurements at ϱ_{AQ} = 1.45 kg dm^{-3} the drag force balances the centrifugal force at lower rational disc speed. The decrease in ε_{ORG} thus becomes smaller when the concentration of KI in the aqueous phase is increased.

3.4.6. Comparison of tomography vs. photographic image analysis

Figure 11 shows a cut-out of the photographic image that was made at Θ = 0.56 m^3_{ORG} : m^3_{TOT} and N = 175 RPM at high ink concentration for the water/*n*-heptane system. High ink concentration was used to enhance the contrast between both phases for photography imaging. The corresponding black-and-white image obtained from this image though the Image Processing Toolbox is also shown. The *n*-heptane is represented by the white area. *n*-Heptane droplets with a diameter smaller than 0.5 10^{-3} m are below the detection limit and are not always taken into account. The organic phase volume fraction is therefore underestimated. The organic phase volume fraction is calculated by multiplying the white area with the bottom slit height and dividing by the total volume of the bottom slit.

This assumes that the *n*-heptane-water boundary has no curvature and that the water film thickness on top and bottom of the *n*-heptane droplet are negligibly thin. Visual comparison of the photograph with the black and white image shows that the detection algorithm is less reliable and severely underestimates the volume fraction. Therefore, volume fraction measurements above 300 RPM are not shown.

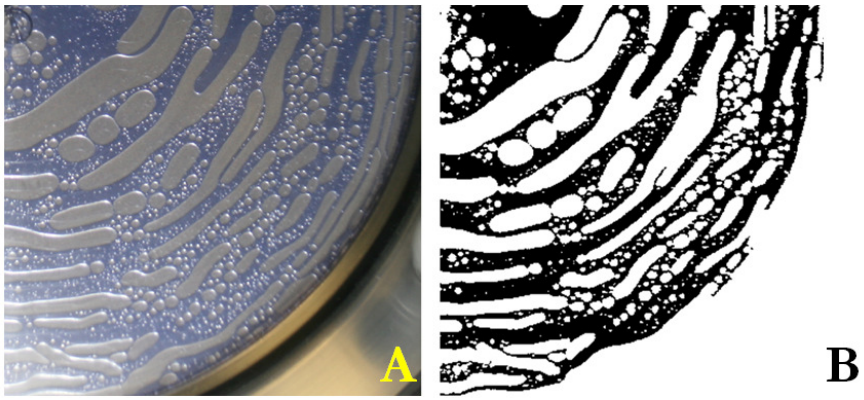

Figure 11. Comparison between the photograph (left) and the resulting black and white image (right). Picture is taken with an aqueous phase density of 0.99 kg dm^{-3}, high ink concentration, stainless steel rotor, Θ = 0.56 m$^3_{ORG}$: m$^3_{TOT}$, and N = 175 RPM.

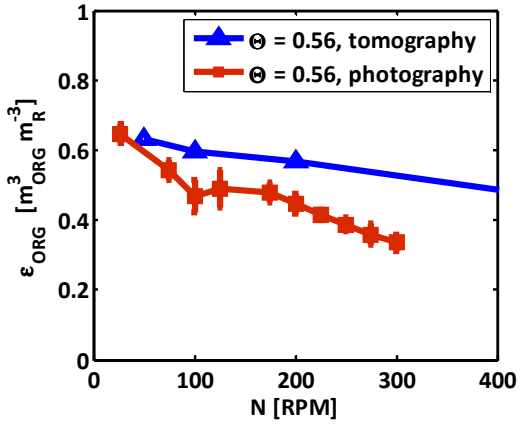

Figure 12. The organic phase volume fraction versus rotational disc speed, as determined from image analysis and tomography measurements. Both measurements are made without ink and an aqueous phase density of 0.99 kg dm^{-3}. Below 50 RPM, the degree of dispersion is minimal, and the results are equal. The tomography data are taken from Figure 9.

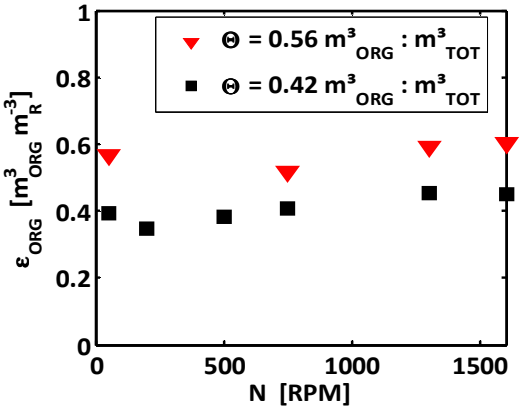

Figure 13. Volume fraction of the organic phase, measured with a stainless steel rotor, with high ink concentration and an aqueous phase density of 0.99 kg dm^{-3}.

Figure 12 shows both the volume fraction found with tomography and photography. At low rotational disc speed, both methods give the same volume fraction. With increasing rotational disc speed, the volume fractions obtained from photography become more biased. This comparison shows that at the low rotational disc speed, i.e. below 75 RPM, all values measured for the organic phase volume fraction, ε_{ORG}, which are obtained from the tomography measurements are equal to those obtained from the photographic analysis.

The comparison also indicates that above 300 RPM tomography yields a more accurate determination of the organic phase volume fraction. To enhance the visual contrast that is needed for the photographic image analysis, water soluble ink was added to the aqueous phase. For mixtures with a low ink concentration in the aqueous phase, the organic phase volume fraction is nearly constant over the total range of rotational speeds (**Figure 10**). For Θ = 0.65 m^3_{ORG} : m^3_{TOT} and Θ = 0.31 m^3_{ORG} : m^3_{TOT}, the volume fraction decreases approximately 10% from 50 to 200 RPM. The increase of ε_{ORG} between a rotational disc speed of 200 and 1600 RPM is largest for Θ = 0.31 m^3_{ORG} : m^3_{TOT}.

For mixtures with a high ink concentration in the aqueous phase, ε_{ORG} is shown as a function of the rotational disc speed in **Figure 13**. For Θ = 0.56 m^3_{ORG} : m^3_{TOT} and Θ = 0.42 m^3_{ORG} : m^3_{TOT}, an equal trend is observed as for the experiments without ink and in which low ink concentrations were used.

3.5. Conclusions

The volume fractions of *n*-heptane and water were measured inside a rotor-stator spinning disc reactor through γ-ray tomography and photography. The organic phase volume fraction was determined as a function of rotor speed, flow ratio, rotor material, and of the position in the reactor. In addition, the effect of density difference was determined by dissolving potassium iodide in the water phase. For low rotational disc speed, the volume fraction decreases slightly with the rotational disc speed: the centrifugal force accelerates the larger droplets to the center. At high rotational disc speeds the droplets become smaller and the friction between the phases determines the flow and the volume fraction becomes equal to the *n*-heptane to total flow ratio. For all measurements, the organic phase volume fraction decreases with an increase of the water flow rate. Measurements in the slit between the rotor and the bottom stator are representative for the slit between the rotor and the top stator, and thus for the entire reactor. Measurements were performed with a stainless steel rotor and a poly(methyl methacrylate) (PMMA) rotor, both with PMMA stators. Below a rotational disc speed of 75 RPM the results of tomography and photographic image analysis are within 10% deviation, indicating the reliability of the γ-ray tomography. With the organic phase volume fraction known, accurate calculations can be made of the liquid-liquid mass transfer rate, and the pressure drop.

Nomenclature

Roman symbols

A_L	Projected area, m^2
a	Centrifugal acceleration, m s^{-2}
C_D	Drag coefficient, -
d	Droplet diameter, m
E	Attenuation matrix
m	Mass, kg
M	Sinogram matrix
N	Rotational disc speed, RPM
R	Disc radius, m
V	Volume, m^3
v	Velocity, m s^{-1}

Greek letters

ε	Volume fraction, m^3_{ORG} m^{-3}_L
ϱ	Density, kg m^{-3}
μ	Non-superimposed cross-sectional attenuation distributions, -
Θ	*n*-Heptane to total flow ratio, m^3_{ORG}:m^3_{TOT}
ω	Angular velocity, rad s^{-1}
φ	Volumetric flow rate, m^{-3} s^{-1}

Sub- and superscripts

AQ	Aqueous phase
C	Centrifugal
D	Drag
d,p	Detector, d, and projections, p
i,j	Matrix/image index
LOC	Local
MAX	Maximal contrast
MEAS	Measurement
ORG	*n*-heptane
TOT	Total

4. Liquid-liquid mass transfer in a rotor-stator spinning disc reactor

This chapter has been published as:

Visscher F., van der Schaaf, J., de Croon, M.H.J.M., Schouten, J.C., **"Liquid-liquid mass transfer in a rotor-stator spinning disc reactor",** *Chemical Engineering Journal*, 2012, 185-186, pp. 267-273.

Abstract

This chapter presents the liquid-liquid flow behavior and the overall liquid-liquid mass transfer rates for a rotor-stator spinning disc reactor, with an axial disc spacing of 1.0 10^{-3} m, a rotor radius of 0.066 m, and rotational disc speeds up to 1600 RPM. The overall liquid-liquid mass transfer rate is determined from extraction experiments of benzoic acid from *n*-heptane to water. For the calculation of the overall mass transfer rate the dimerization and acid dissociation equilibria are taken into account. Three flow patterns are characterized. Up to 100 RPM continuous radially inwards spiraling *n*-heptane patterns are observed. Between 100 RPM and 300 RPM this continuous spiral changes to spiraling *n*-heptane droplets. Above 300 RPM fully dispersed phase flow is observed. The overall mass transfer rate increases from 0.17 m^3_{ORG} m^{-3}_R s^{-1} at 100 RPM and a water flow rate of 2.5 10^{-6} m^3_{AQ} s^{-1} (water : *n*-heptane = 1.1:1) to 51.47 m^3_{ORG} m^{-3}_R s^{-1} at 1600 RPM and a water flow rate of 12.5 10^{-6} m^3_{AQ} s^{-1} (water : *n*-heptane = 5.6:1). These mass transfer rates are at least 25 times higher compared to those in packed columns, and at most 15 times higher compared to mass transfer rates in state of the art microchannels.

4.1. Introduction

Liquid-liquid processes are widely encountered in chemical industry. Examples of liquid-liquid reactions that are relevant on industrial scale are, e.g., the exothermic nitration of aromatic compounds (Zaldívar et al., 1996), the production of benzaldehyde, hydroformylation of propene and polymerization reactions like the Shell Higher Olefin Process (Wiseman, 1979). Most contactors used for liquid-liquid processes, like the Kuhni column, the rotating disc column, or the pulsed perforated plate column, are space consuming, requiring a significant processing time, and involving severe safety challenges. Therefore equipment with a larger productivity is desired. Such a productivity increase can be obtained by increasing mass transfer rates for processes in which the mass transfer rate is limiting. This is the case for most liquid-liquid processes.

This chapter investigates the liquid-liquid flow behavior and the overall liquid-liquid mass transfer rates in a co-current operated rotor-stator spinning disc reactor. This multiphase reactor is shown in **Figure 1** and consists of a rotating disc, the rotor, which is enclosed by two stationary discs, the stators, and a stationary cylindrical housing. The velocity gradient over the volume between the rotor and the stator causes an intense shear force to act on the reactor contents. The resulting turbulent intensity causes a strong dispersion of the reactor contents, and thus a high surface area. The application of this multiphase reactor for gas-liquid systems was described before. There it was shown with oxygen desorption experiments that the volumetric mass transfer coefficient per gas volume is about 40 times higher than for a bubble column (Meeuwse et al., 2010b). The liquid-solid mass transfer coefficient was determined to vary from 0.02 to 0.22 $m^3_L\ m^{-3}_R\ s^{-1}$ (Meeuwse et al., 2010a).

In this study the overall liquid-liquid mass transfer rates are determined by extracting benzoic acid from *n*-heptane to water. This extraction system was described before by Visscher et al., (Visscher et al., 2011). This system is applicable for experimental set-ups which consist of poly(methyl methacrylate), a common construction material. Benzoic acid is strongly UV-active which gives the possibility to measure the solute concentration in both *n*-heptane and water, up to low concentrations.

Upon rotation of the rotor the shear forces between the rotor and the stators will cause a dispersion of *n*-heptane in water. This results in high overall liquid-liquid mass transfer rates. The overall liquid-liquid mass transfer coefficients in the rotor-stator spinning disc reactor are much higher than those reported for conventional equipment. These high mass transfer rates therefore allow for an intensification of the process, i.e. a considerable reduction of process equipment volume.

4.2. Experimental section

4.2.1. Experimental set-up

The rotor-stator spinning disc reactor used is described in detail before (Meeuwse et al., 2010b), and is graphically depicted in **Figure 1**. The 0.132 m wide rotor (stainless steel) is located at 1.0 10^{-3} m from the top and bottom stators, which are both from poly(methyl methacrylate). The stationary cylindrical housing is located at 10 10^{-3} m from the rim of the rotor. The reactor volume is 49.7 10^{-6} m^3.

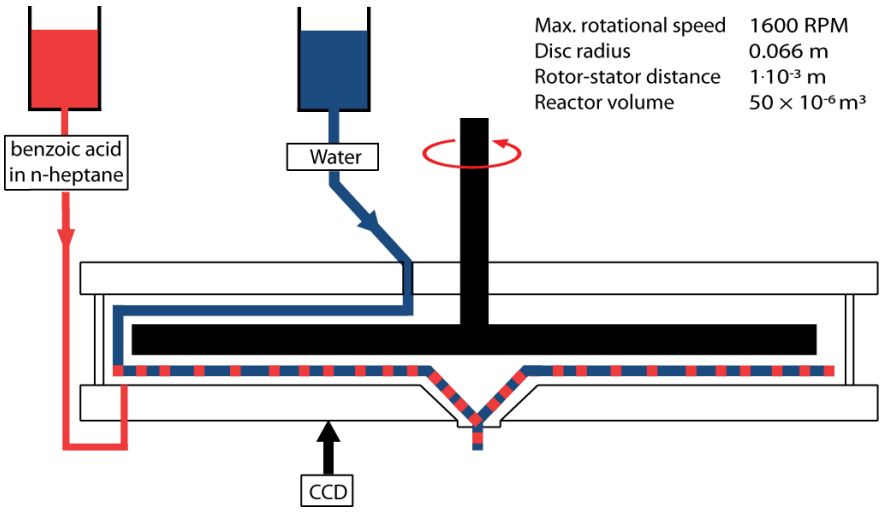

Figure 1. Schematic drawing of the rotor-stator spinning disc set-up. The rotor is located at 1.0 10^{-3} m from the top and bottom stator. Water is fed to the top of the reactor near the axis. *n*-Heptane with benzoic acid is fed through an inlet in the bottom stator near the rim of the disc.

The water phase is fed to the top of the reactor through an inlet in the top stator by a pump (Siemens, 1LA6) combined with a Coriolis mass flow controller (Bronkhorst, M55). The inlet is located next to the rotating axis. *n*-Heptane with dissolved benzoic acid is fed to the reactor by a calibrated peristaltic pump (Cole-Palmer Masterflex) through an orifice in the bottom stator.

The orifice has a diameter of 1.4 10^{-3} m, which is located at 62 10^{-3} m from the axis in the bottom stator. These experiments were performed for rotational disc speeds up to 1600 RPM and an *n*-heptane flow of 2.2 10^{-6} m^3_{ORG} s^{-1}. The water flow rate ranged from 2.5 10^{-6} m^3_{AQ} s^{-1} to 15.0 10^{-6} m^3_{AQ} s^{-1}. Measurements of the steady state concentrations were repeated at least three times for each experimental condition. The average values of the measured concentrations were used to calculate the overall mass transfer rate.

4.2.2. Materials

The water/*n*-heptane benzoic acid system was selected as the extraction system. For all experiments demineralized water was the continuous phase. In the experiments demiwater, *n*-heptane (99% from Sigma-Aldrich) and benzoic acid (99.5% from Merck) was used. The demiwater was demineralized with a Millipore Elix UV-10. The water content in the benzoic acid was measured by weighing a specific amount of benzoic acid before and after a 24 hour period of drying at 373 K, and was determined to be less than 1 wt%. Pelikan Royal Blue ink was used as a dye for the water phase in the visualization experiments. No further purification was performed on the chemicals. All experiments were performed at ambient temperature.

4.2.3. Image analysis

The flow pattern between the rotor and the bottom stator was digitally recorded by a Canon EOS digital 400D camera. All photographs were made via a mirror that was located at a 45^{o} angle, below the reactor to prevent leaking on the camera. The water phase was colored blue by Pelikan Royal Blue ink. The phases could be distinguished based on the grey value. The Image Processing Toolbox from Matlab® was used, in combination with Adobe® Photoshop CS4, for determination of the *n*-heptane volume fraction. The volume fraction was estimated by determining the fraction of the surface of the disc where *n*-heptane is present. For each experimental condition the volume fraction was determined from eight photographic images. The rotational discs speed ranged from of 50 to 1600 rpm. The *n*-heptane flow was 2.2 10^{-6} m^3_{ORG} s^{-1} and the water flow rate ranged from 2.5 10^{-6} m^3_{AQ} s^{-1} to 15.0 10^{-6} m^3_{AQ} s^{-1}. Therefore the aqueous to organic flow ratio, θ, ranges from 1.1 to 6.8.

4.2.4. Mass transfer experiments

At time t = 0, the volumetric through flow of *n*-heptane + benzoic acid was started. Samples of approximately 10 10^{-6} m^3_L were withdrawn from the reactor outlet at time intervals of 10 seconds. These samples separated quickly, typically within two seconds. From these samples 4 10^{-6} m^3_L of both phases was collected in sealed flasks. Each of these samples was diluted by a factor 25 by using a 0.5 10^{-6} m^3 Finn pipette.

The benzoic acid concentration was determined for water and *n*-heptane by UV-VIS spectroscopy. Based on these measurements in time, the steady state concentrations were determined for both phases. The absorption spectra of all samples were measured on a Shimadzu UV-1650PC UV-VIS spectrophotometer. All samples were measured in quartz cuvets, type 100-QS, with a path length of 10 mm. For *n*-heptane the peak at 275 nm is used for determination of the benzoic acid concentration, for water the peak at 269 nm has been selected. The molecular absorption coefficient of benzoic acid in *n*-heptane at 275 nm was determined from the calibration curve to be 996 dm^3 mol^{-1} cm^{-1}, which is close to the value of 1000 dm^3 mol^{-1} cm^{-1} that was reported before (Hosoya et al., 1962).

The absorption coefficient of benzoic acid in water at 269 nm was determined to be 541 $dm^3\ mol^{-1}\ cm^{-1}$, which is close to the value of 560 $dm^3\ mol^{-1}\ cm^{-1}$ that was reported before (Hosoya et al., 1961). Measurements for which the measured concentrations would yield a mass balance that was more than 5% deviated, were discarded from further calculations.

4.3. Results and discussion

4.3.1. Flow patterns

Figure 2 shows the flow pattern between the rotor and the bottom stator as a function of the rotational disc speed, N. For the given system three different flow patterns are observed as a function of the rotational disc speed. First, up to 100 RPM, a radial inward flow of the *n*-heptane is observed as a continuous spiral without back mixing. This *n*-heptane spiral is entwined with a continuous water spiral that contains *n*-heptane droplets. These droplets are formed at low water flow rates from a spill of *n*-heptane to the top of the rotor at the injection point.

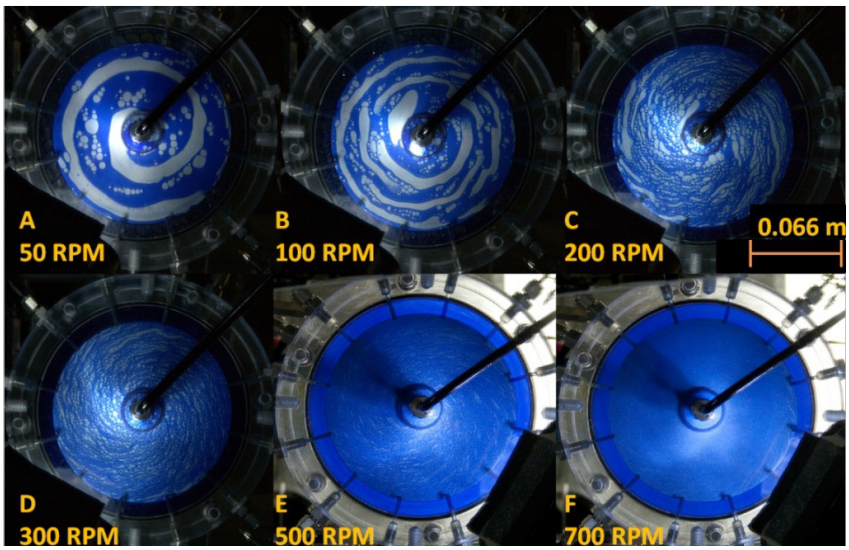

Figure 2. The influence of rotational disc speed on the volume fraction inside the reactor. Pictures are made through the bottom stator, with a total flow rate of 4.7 10^{-6} $m^3\ s^{-1}$. Water appears blue by the ink, the *n*-heptane appears white.

For this case, both *n*-heptane and water are assumed to have plug flow behavior. Second, above 100 RPM, the continuous *n*-heptane spiral breaks up into droplets due to the enlarged shear force that is present between the rotor and the bottom stator. The droplets move along a spiral path to the center. No back mixing is observed, therefore all *n*-heptane droplets have an equal residence time. Also in this case both phases are assumed to have plug flow behavior. Third, above 300 RPM, the *n*-heptane droplets become dispersed in the water phase, such that the droplet diameter becomes smaller than the axial clearance between the rotor and the stator, 1.0 10^{-3} m. Due to the formation of boundary layers on the rotor and the stator (Schlichting et al., 1999, Poncet et al., 2005b), back mixing occurs of both *n*-heptane and water.

In this case both phases are assumed to behave as mixed flow. During the experiments *n*-heptane was also observed between the top stator and the rotor. This is only possible for mixed flow. **Figure 3** shows the flow pattern for an increased value of the aqueous to organic flow ratio, Θ, at 50 RPM. When operating at a flow ratio, Θ, of 1.1, a continuous spiral of *n*-heptane is observed that needs approximately 1.5 rounds from the *n*-heptane inlet near the rim of the rotor, to the reactor outlet at the center of the bottom stator. At Θ = 2.3 this same spiral exists but the length of the spiral has decreased to a single swirl around the center.

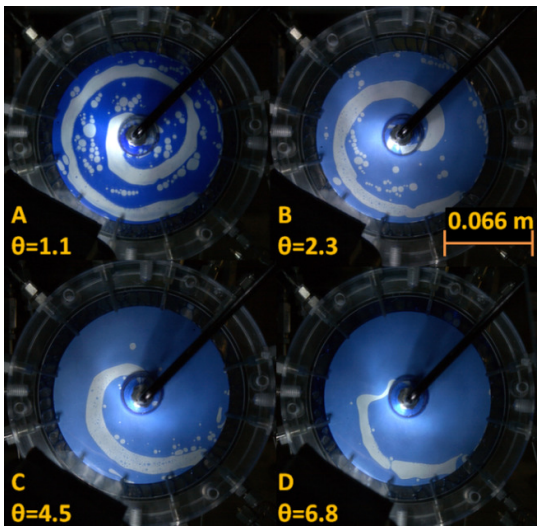

Figure 3. The influence of the flow ratio, θ, on the *n*-heptane volume fraction, ε_{ORG}, at 50 RPM. Water is colored blue by the ink, the *n*-heptane appears white. It is observed that the residence time of *n*-heptane in the reactor decreases with an increasing water flow rate: the number of swirls around the axis decreases.

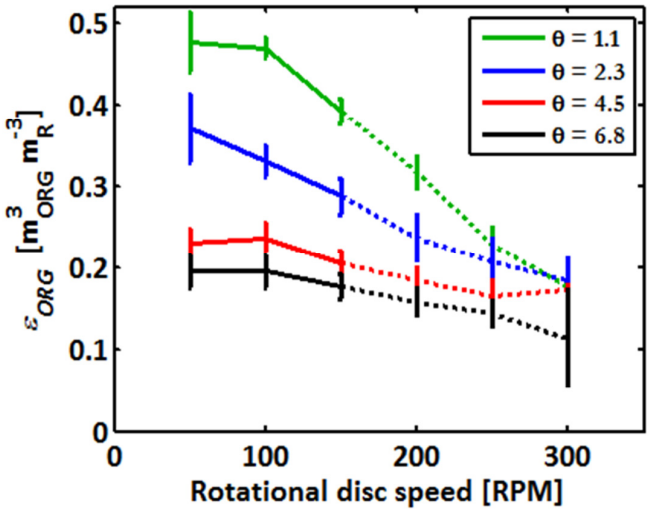

Figure 4. Influence of rotational disc speed and flow ratio on the *n*-heptane volume fraction. The *n*-heptane volume fraction decreases for an increasing rotational disc speed and for an increasing flow ratio. The dotted lines represent the *n*-heptane volume fraction, without taking droplets smaller than 1 10^{-3} m into account.

The number of *n*-heptane droplets from the spill has decreased too. At θ = 4.5 the spiral decreases to a half swirl around the center, and at θ = 6.8 the swirl becomes shorter and less thick when compared to θ = 4.5. This causes a shorter spiral, and thus a lower *n*-heptane volume fraction. The formation of droplets from a spill is not observed anymore. The irregular shape of the *n*-heptane spiral is caused by the pulsed injection of *n*-heptane by the Masterflex® pump.

4.3.2. *n*-Heptane volume fraction

The photographs in **Figure 2** and **Figure 3** were analyzed with MatLab® software, using the Image Processing Toolbox. Based on this analysis the *n*-heptane volume fraction, ε_{ORG}, was found to decrease as a function of rotational disc speed from 0.47 $m^3_{ORG}\,m^{-3}_R$ at 50 RPM towards 0.18 $m^3_{ORG}\,m^{-3}_R$ at 300 RPM and θ = 1.1.

Also the *n*-heptane volume fraction decreased (at a constant rotational disc speed of 50 RPM) from 0.47 $m^3_{ORG}\,m^{-3}_R$ to 0.19 $m^3_{ORG}\,m^{-3}_R$ with θ ranging from 1.1 to 6.8. The reproducibility of these numbers is high, i.e. less than 10% error. This is shown in **Figure 4**. At rotational disc speeds above 150 RPM the *n*-heptane volume fraction becomes biased because some droplets have a diameter smaller than the disc spacing of 1.0 10^{-3} m. These smaller droplets have a low contrast, and are not always detected by the MatLab® script. Thus, the percentage of disc area that is determined by the software underestimates the *n*-heptane volume fraction for rotational disc speeds larger than 150 RPM. Above 300 RPM almost all droplets are smaller than 1.0 10^{-3} m, and the *n*-heptane volume fraction cannot be determined anymore.

Therefore the *n*-heptane volume fractions in **Figure 4** are represented as dotted lines for rotational disc speeds larger than 150 RPM. For an increase of the water flow rate, the *n*-heptane swirl is forced more strongly to the reactor outlet in the center of the reactor. This results in a decrease of the swirl length from the rim towards the center. This can be seen in **Figure 3**. This implies that the volume fraction of the organic phase decreases with the increasing water flow, and thus with an increasing aqueous to organic flow ratio.

The value for the *n*-heptane volume fraction is needed for the determination of the overall liquid-liquid mass transfer coefficient. Since the volume fractions are biased for rotational disc speeds higher than 300 RPM, this would mean that the overall mass transfer rate could not be determined accurately above 300 RPM.

4.3.3. Liquid-liquid extraction system

For the water/*n*-heptane/benzoic acid system three equilibriums are present: the acid-base equilibrium of benzoic acid in the water, the dimerization of benzoic acid in *n*-heptane, and the mass transfer of benzoic acid over the water/*n*-heptane interface (Visscher et al., 2011).

The observed partition coefficient is equal to the ratio of the total concentration, C^{TOT}, in both phases. The total concentration in water is equal to the sum of the dissociated and the non-dissociated benzoic acid, as is shown in equation (1). The total concentration in *n*-heptane is equal to the sum of the monomeric and dimeric species of benzoic acid, as is shown in equation (2). Assuming that only the non-dissociated monomeric species can partition over the water/*n*-heptane interface, the partition coefficient relevant for the mass transfer is given by equation (3).

$$C_{AQ}^{TOT} = C_{AQ}^{HA} + C_{AQ}^{A^-} \quad (1)$$

$$C_{ORG}^{TOT} = C_{ORG}^{MON} + 2C_{ORG}^{DIM} \quad (2)$$

$$K_P^{MON} = \frac{C_{ORG}^{MON}}{C_{AQ}^{HA}} \quad (3)$$

Following the two-film theory, the overall liquid-liquid mass transfer coefficient can be described as a result of the resistance to mass transfer in the aqueous phase, k_{AQ}, and the resistance to mass transfer in the organic phase, k_{ORG}. Each resistance originates from the diffusion of the solute through a laminar boundary layer near the water/*n*-heptane interface. The resistances to mass transfer combine into an overall resistance to mass transfer, k_L, and are interrelated by the monomeric partition coefficient, K^P_{MON}, of benzoic acid over the water/*n*-heptane interface:

$$\frac{1}{k_L} = \frac{1}{k_{ORG}} + \frac{K_P^{MON}}{k_{AQ}} \quad (4)$$

The product of the overall liquid-liquid mass transfer coefficient, k_L, with the specific liquid-liquid interfacial area, a_L, and the *n*-heptane volume fraction, ε_{ORG}, yields $k_L a_L \varepsilon_{ORG}$ and expresses the overall mass transfer rate in units of $m^3_{ORG}\, m^{-3}_R\, s^{-1}$.

4.3.4. Determination of the steady state concentrations

The concentration profiles in both phases are shown as a function of time and flow ratio for 1200 RPM in **Figure 5**. The point t = 0 represents the situation at which the *n*-heptane with benzoic acid flow enters the reactor. Based on the reactor volume of 49.7 10^{-6} m^3, the overall residence time equals 10.6 s (for Θ = 1.1), 6.9 s (for Θ = 2.3), and 2.8 s (for Θ = 5.6).

By plotting the outlet concentrations vs. time it can be seen that a steady state situation is obtained after approximately 37 s for Θ = 1.1, 24 s for Θ = 2.3 s, and 10 s Θ = 5.6. These times to steady state correspond to approximately 3.5 times the overall residence time for all flow ratios. With an increase of the water flow rate, the overall residence time decreases, and thus the system is further away from the equilibrium composition. The steady state concentrations in both phases were determined for rotational disc speeds ranging from 0 to 1600 RPM.

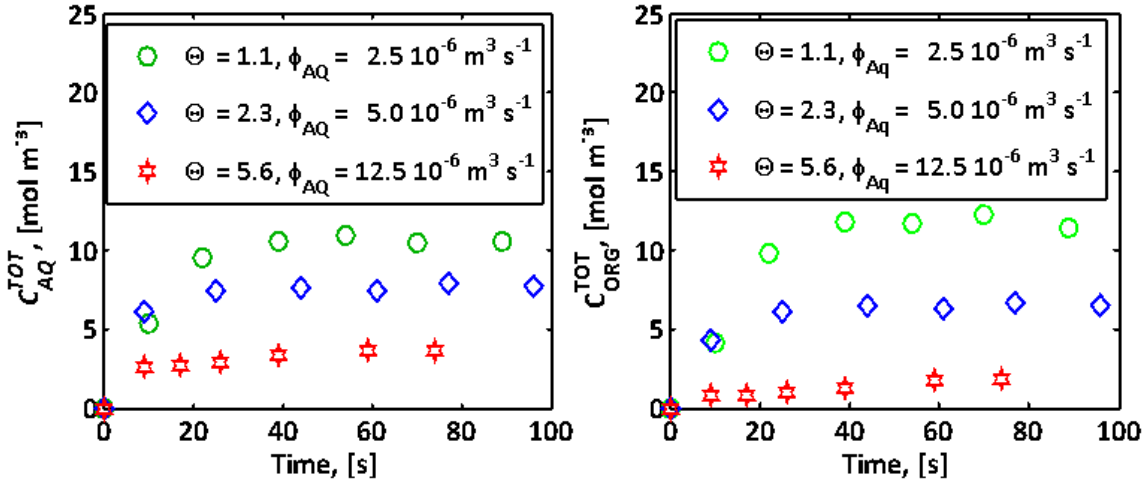

Figure 5. A, left: Total concentration of benzoic acid in the water phase versus time at 1200 RPM and an *n*-heptane flow rate, φ_{ORG}, of 2.2 10^{-6} m^3 s^{-1}. The reactor is initially filled with water only. At t = 0 the *n*-heptane flow is started. The initial concentration in the reactor is 0 mol m^{-3}. B: right: Total concentration of benzoic acid in *n*-heptane versus time at 1200 RPM and an *n*-heptane flow rate, φ_{ORG}, of 2.2 10^{-6} m^3 s^{-1}. The reactor is initially filled with water only. At t = 0 the *n*-heptane flow is started. The inlet concentration of benzoic acid in *n*-heptane is 24 mol m^{-3}.

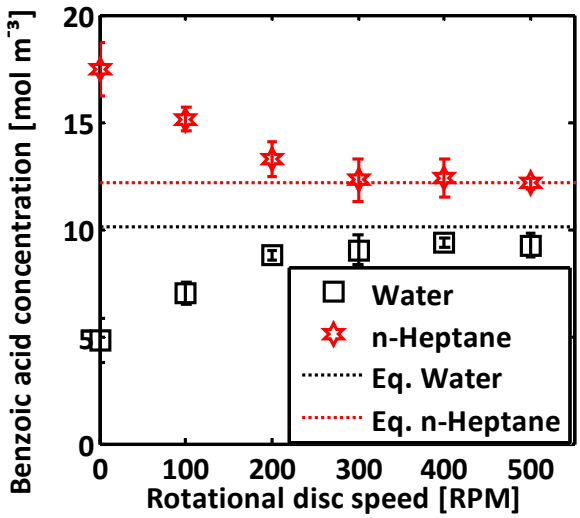

Figure 6. Steady state benzoic acid concentrations for water and *n*-heptane, as a function of the rotational disc speeds at Θ = 1.1. The equilibrium concentrations in both phases are shown as dotted lines for the givens system.

Figure 6 shows the measured steady state concentrations as a function of the rotational disc speed, and the equilibrium concentrations for Θ = 1.1. Above 600 RPM, the steady state concentrations do not change anymore, because the concentrations at the outlet are in equilibrium; an accurate determination of the $k_LA\varepsilon_{ORG}$ values is therefore not possible. The $k_LA\varepsilon_{ORG}$ values for higher rotational disc speeds could therefore only be determined for flow ratios higher than 1.1.

4.3.5. Modeling mass transfer

With the steady state concentrations and the flow behavior known, the overall mass transfer rate can be calculated from the mass balance over the reactor. Based on the flow patterns observed in **Figure 2** and **Figure 3**, plug flow behavior is assumed for both phases for rotational disc speeds up to 300 RPM. Above 300 RPM mixed flow behavior is assumed for both phases.

By assuming plug flow behavior, the general mole balance can be written in the form of equations (5) and (6), where $k_L a_L \varepsilon_{ORG}$ is the overall mass transfer rate with the units $m^3_{ORG}\ m^{-3}_{R}\ s^{-1}$, and K_P^{MON} the monomeric partition coefficient of the non-dissociated monomer between water and *n*-heptane with the units $m^3_{AQ}\ m^{-3}_{ORG}$.

$$\frac{dC_{AQ}^{TOT}}{dV} = -\frac{k_L a_L \varepsilon_{ORG}}{\varphi_{v,AQ}}\left(C_{ORG}^{MON} - K_P^{MON} C_{AQ}^{HA}\right) \tag{5}$$

$$\frac{dC_{ORG}^{TOT}}{dV} = \frac{k_L a_L \varepsilon_{ORG}}{\varphi_{v,ORG}}\left(C_{ORG}^{MON} - K_P^{MON} C_{AQ}^{HA}\right) \tag{6}$$

The concentration difference in equations (5) and (6) is the driving force for mass transfer. In equations (5) and (6), C_{ORG}^{MON} represents the concentration of benzoic acid monomer in *n*-heptane, and C_{AQ}^{HA} the non-dissociated benzoic acid concentration in water.

The relevant concentrations for mass transfer, that are needed to solve equations (5) and (6), can be calculated as a function of the total concentration in each phase by using the acid-base equilibrium constant and the dimerization constant. This is shown in the equations (7) and (8).

$$C_{ORG}^{MON} = \frac{-1 + \sqrt{1 + 8K_D C_{ORG}^{TOT}}}{4K_D} \tag{7}$$

$$C_{AQ}^{HA} = \frac{\left(-\frac{1}{2}K_A + \frac{1}{2}\sqrt{K_A{}^2 + \left(4C_{AQ}^{TOT}K_A\right)}\right)^2}{K_A} \tag{8}$$

To solve the equations (7) and (8), K_P^{MON} and K_D were used as reported before. They were determined from a fit of the equilibrium line and equal $K_P^{MON} = 0.21 \pm 0.05\ m^3_{AQ}\ m^{-3}_{ORG}$ and $K_D = 1.3 \pm 0.7\ m^3\ mol^{-1}$ (Visscher et al., 2011). With these constants known, the differential equations from equations (5) and (6) are numerically solved for different flow rates. Solving these balances for various values of $k_L a_L \varepsilon_{ORG}$ resulted in different steady state concentrations for each phase. The steady state concentrations are shown as a function of $k_L a_L \varepsilon_{ORG}$ in **Figure 7**.

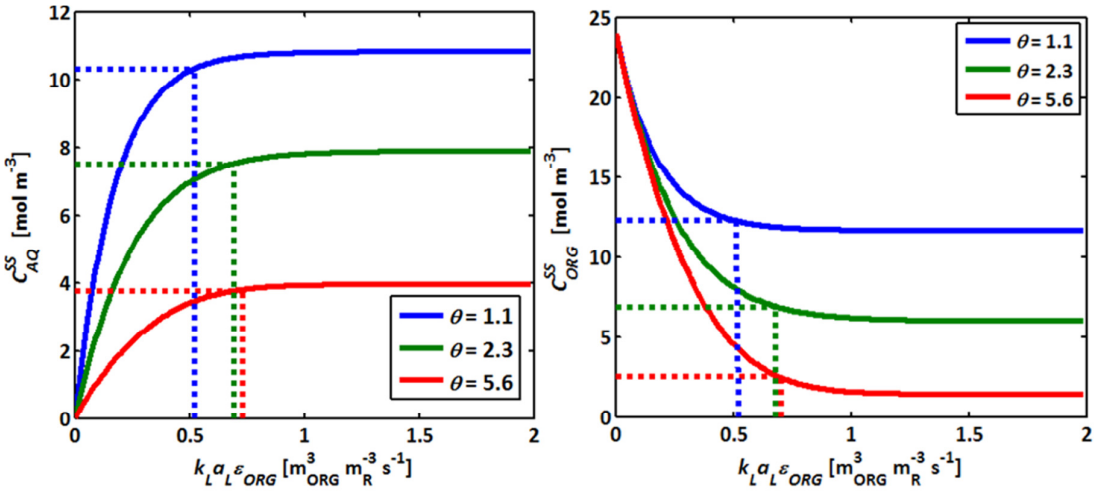

Figure 7. A, Left: Simulation results of the steady state concentrations in the water phase as a function of $k_L a_L \varepsilon_{ORG}$. The continuous lines show the steady state concentrations, the dotted lines show the steady state concentrations at which the concentration is 95% from equilibrium. B, right: Simulation results of the steady state concentrations in *n*-heptane as a function of $k_L a_L \varepsilon_{ORG}$. The continuous lines show the steady state concentrations, the dotted lines show the steady state concentrations at which the concentration is 95% from equilibrium.

For an increasing flow ratio a lower steady state concentration is reached. This is consistent with the experimental observations that were shown in **Figure 5**. For the outer limits of the 95% confidence interval of K_P^{MON} the corresponding values of K_D were calculated. The effect of these different constants on $k_L a_L \varepsilon_{ORG}$ was modeled and is less than 10%. Near equilibrium, the $k_L a_L \varepsilon_{ORG}$ value is sensitive for errors in the steady state concentration measurement. Therefore, an arbitrary limit of 95% was set for the highest allowable extraction efficiency that can be used for the calculation of the $k_L a_L \varepsilon_{ORG}$ values. The 95% extraction efficiency limit, following from equation (9) is represented in **Figure 7** by the dotted horizontal lines. This extraction efficiency is defined as:

$$E(\%) = \frac{C_{ORG}^{SS} - C_{ORG}^{INIT}}{C_{ORG}^{EQ} - C_{ORG}^{INIT}} \times 100\% \qquad (9)$$

4.3.6. Calculation of the $k_L a_L \varepsilon_{ORG}$-values

Figure 8 shows the $k_L a_L \varepsilon_{ORG}$ values for a rotational disc speed ranging from 0 to 300 RPM, and for the θ = 1.1 and θ = 6.8. Calculations are based on plug flow behavior of both phases and on the steady state concentrations in the water phase. For θ = 1.1 the overall mass transfer rate, $k_L a_L \varepsilon_{ORG}$ increases from 0.13 to 0.36 $m^3_{ORG}\, m^{-3}_R\, s^{-1}$. For θ = 6.8, $k_L a_L \varepsilon_{ORG}$ increases from 0.34 to 0.39 $m^3_{ORG}\, m^{-3}_R\, s^{-1}$. For rotational disc speeds up to 100 RPM the specific surface area with units $m^2_{INT}\ m^{-3}_L$, can be estimated from the photographic images using Photoshop CS4. For N = 50 rpm and θ = 1.1, shown in photograph A of **Figure 2**, this equals at least 600 $m^2_{INT}\ m^{-3}_L$. From **Figure 8**, $k_L a_L \varepsilon_{ORG}$ equals 0.13 $m^3_{ORG}\, m^{-3}_R\, s^{-1}$ and from **Figure 4** ε_{ORG} is about 0.5 $m^3_{ORG}\, m^{-3}_R$. This yields $k_L a_L$ = 0.26 s^{-1}.

With a_L equal to 600 m^2_{INT} m^{-3}_L this makes the overall resistance to mass transfer at least in the order of 10^{-3} m^3_L m^{-2}_{INT} s^{-1} which is a factor 10 higher than the values reported for microchannels (Ghaini et al., 2010).

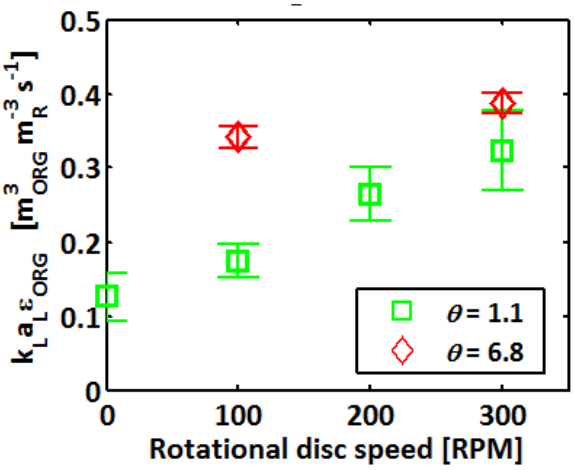

Figure 8. $k_La_L\varepsilon_{ORG}$ as a function of rotational disc speed. The $k_La_L\varepsilon_{ORG}$ values are increasing with the aqueous to organic flow ratio. When corrected for the ε_{ORG} values from Figure 4, the influence of the aqueous to organic flow ratio on the k_La_L is small.

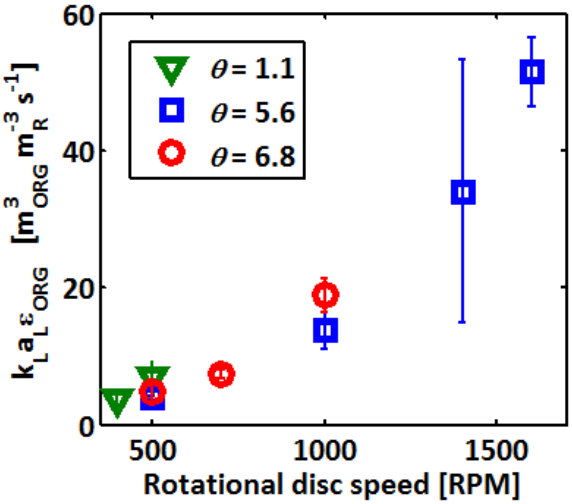

Figure 9. $k_La_L\varepsilon_{ORG}$ as a function of the rotational disc speed, calculated according to mixed flow behavior for both phases in the reactor.

The latter might be due to the surface renewal rate at the liquid-liquid interface. This is also the governing mass transfer mechanism reported for liquid–liquid two-phase flow in micro structured reactors (Ghaini et al., 2010, Ghaini et al., 2011, Kashid et al., 2010), and leads to high mass transfer rates due to the fast refreshment of the film volume. The formation of boundary layers on the rotor and the stator at higher rotational disc speeds (Poncet et al., 2005b, Schlichting et al., 1999), might facilitate this surface renewal. The difference in the flow pattern between 300 and 400 RPM is based on the back mixing due to the boundary layers that are formed. The difference in mass transfer rate of the two flow patterns is about a factor 10, as is seen from the difference between **Figure 8** and **Figure 9**.

Figure 9 shows an increase in $k_{LaL}\varepsilon_{ORG}$ from 3.79 $m^3_{ORG}\,m^{-3}_R\,s^{-1}$ at 400 rpm and θ = 1.1 to 51.47 $m^3_{ORG}\,m^{-3}_R\,s^{-1}$ at 1600 rpm and θ = 6.8. Mixed behavior for both phases was assumed for these conditions. The increase in $k_{LaL}\varepsilon_{ORG}$ for θ = 5.6 from 500 to 1600 rpm and for θ = 6.8 from 500 to 1000 rpm is non-linear. The high overall mass transfer rate reported at rotational disc speeds higher than 300 rpm is most likely due to the increased turbulence intensity in the system, and the increased specific surface area, which are both caused by the increased shear force between the rotor and the stator.

4.3.7. Performance comparison to other liquid-liquid contactors.

The overall liquid-liquid mass transfer rates found in this study are high, when compared to conventional equipment. An extensive list with typical k_La_L values and the power input for equipment used for liquid-liquid extraction is given elsewhere (Dehkordi, 2002, Kashid et al., 2011). They report maximum k_{La} values of 0.027 s^{-1} for the rotating disc column (Dehkordi, 2002), 0.011 s^{-1} for a packed column (Dehkordi, 2002), 0.032 s^{-1} for a static mixer (Merchuk et al., 1980), and 0.08 s^{-1} for an agitated vessel (Fernandes et al., 1967).

More modern reactor types like a T-junction microchannel gives mass transfer rates up to 17.35 s^{-1} (Zhao et al., 2007), 0.95 s^{-1} for liquid-liquid slug flow in a capillary (Kashid et al., 2007a), and up to 14.5 s^{-1} for a packed bed microchannel (Su et al., 2010). With the *n*-heptane volume fraction from Figure **4** the mass transfer rates, k_{La}, for the rotor-stator spinning disc reactor are at least 10 times higher than for the rotating disc column and at least 25 times higher than for a packed column.

A conservative estimation of ε_{ORG} using **Figure 4** yields $\varepsilon_{ORG} \approx 0.2$ m^3_{ORG} m^3_R for rotational disc speeds above 300 rpm. Using this *n*-heptane volume fraction, k_La_L can be calculated from $k_{LaL}\varepsilon_{ORG}$. At 1000 rpm k_{La} equals 75 ± 10 s^{-1}. This is already a factor 5 higher than to the maximum values reported for microchannels.

At 1600 rpm, this gives k_{La} of 250 ± 25 s^{-1}, a factor 10-20 higher than the maximum value reported for microchannels. When the volume fractions are used reported in **Chapter 3**, still the liquid-liquid mass transfer rates are high.

The reactor volume for a single stage in the rotor-stator spinning disc reactor equals 50 10^{-6} m^3. This volume can be enlarged by stacking multiple discs, which is more energy efficient than increasing the disc diameter (Meeuwse et al., 2012, Meeuwse et al., 2012). It gives the opportunity of enlarging the residence time in the reactor when needed.

The maximum allowable throughput can also be further enlarged, which is useful when a larger volumetric productivity is desired. This high mass transfer rate combined with the tunable residence times, make that the rotor-stator spinning disc reactor is a promising alternative for mass transfer limited co-current liquid-liquid processes. The reactor allows for further improvements in terms of process efficiency, operating expenses, waste reduction, and process safety (de Vries, 2008).

4.4. Conclusions

The liquid-liquid flow behavior and mass transfer rates in the rotor-stator spinning disc reactor were determined from extraction experiments in which benzoic acid was extracted from *n*-heptane to water. Photographic analysis of the flow pattern between the rotor and the stator showed three possible patterns: continuous spiraling flow, spiraling droplet flow and fully dispersed flow. The flow pattern has a strong influence on the liquid-liquid mass transfer rate.

The overall liquid-liquid mass transfer rate increased from 0.17 $m^3_{ORG}\ m^{-3}_{R}\ s^{-1}$ at 100 rpm and a water flow rate of 2.5 $10^{-6}\ m^3_{AQ}\ s^{-1}$ (water : *n*-heptane = 1.1:1) to 51.47 $m^3_{ORG}\ m^{-3}_{R}\ s^{-1}$ at 1600 rpm and a water flow rate of 12.5 $10^{-6}\ m^3_{AQ}\ s^{-1}$ (water : *n*-heptane = 5.6:1). The liquid-liquid mass transfer rates are at least 25 times higher compared to packed columns, and 10-15 times higher compared to microchannels. The reported increased liquid-liquid mass transfer rates will contribute to a better control over selectivity and yield and a shorter time-to-process.

Nomenclature

Roman symbols

a_L	Specific liquid-liquid interfacial area, $m^2_{INT}\ m^{-3}_L$
D	Diffusion coefficient, $m^2\ s^{-1}$
E	Extraction efficiency, %
h	Rotor-stator distance, m
k_L	Mass transfer coefficient, $m^3_L\ m^{-2}_{INT}\ s^{-1}$
K_A	Acid dissociation constant
K_D	Dimerization constant, $mol\ m^{-3}_{ORG}$
K_P	Partitioning constant, $m^3_{AQ}\ m^{-3}_{ORG}$
N	Rotational speed, RPM
V	Volume, m^3

Greek Letters

ε_L	Volume fraction, $m^3_L\ m^3_R$
θ	Aqueous to organic flow ratio, -
φ	Volumetric flow rate, $m^3\ s^{-1}$

Sub and superscripts

AQ	Water phase
EQ	Equilibrium situation
HA	Non-dissociated species
INIT	Initial value
INT	Interface of the liquids
MON	Monomeric species
ORG	*n*-heptane phase
R	Reactor
SS	Steady state
TOT	Total

5. Liquid-liquid flow in an impeller-stator spinning disc reactor

This chapter has been published as:

Visscher F., Nijhuis, R.T.R. van der Schaaf, J. de Croon, M.H.J.M., Schouten, J.C., **"Liquid-liquid flow in an impeller-stator spinning disc reactor",** *Chemical Engineering and Processing: Process Intensification*, DOI 10.1016/j.cep.2013.01.015.

Abstract

Liquid-liquid flow patterns in an impeller-stator spinning disc reactor are qualitatively described. The liquid-liquid flow is studied by contacting water and *n*-heptane at rotational speeds up to 900 RPM, an axial disc spacing of 1 10^{-3} m, and aqueous volume fractions between 0 and 1 m^3_{AQ} m^{-3}_{L}. The liquid-liquid flow is characterized by six different flow regimes. Each regime is characterized by its continuous liquid phase and the degree of dispersion of the dispersed liquid phase. Regime transitions depend on the formation of boundary layers on the impeller and the stator, the shear stress intensity and the aqueous volume fraction. The impeller is able to selectively pump *n*-heptane through the reactor, whilst it is intensively mixed with water that remains in the reactor. Combining mixing and separation in one compact reactor is an important step toward a countercurrent operated impeller-based centrifugal extractor.

5.1. Introduction

The multiphase flow behavior in a chemical reactor has a major influence on the selectivity and conversion of a given process. Understanding of and control over this flow behavior is therefore essential when a novel multiphase reactor is developed for liquid-liquid processes (Steensma et al., 1988). An example of such a reactor is the rotor-stator spinning disc reactor (SDR). Due to the rotation of the rotor, a velocity gradient is present between the rotor and the stator. The velocity gradient causes a shear force to act upon the liquids between the rotor and the stator. This causes an increase of the liquid-liquid interfacial area and of the turbulence intensity. Accordingly, the liquid-liquid mass transfer rate is increased (Visscher et al., 2012d). The behavior of liquid-liquid and gas-liquid flow in a rotor-stator spinning disc reactor was reported previously (Visscher et al., 2012d, Meeuwse et al., 2010b, van der Schaaf et al., 2011, Visscher et al., 2012b).

This chapter describes the flow behavior of water and *n*-heptane in an impeller-stator spinning disc reactor. In this reactor an impeller is used instead of the solid rotor in the SDR. The impeller has comparable geometry as the impeller in a centrifugal pump. In a centrifugal pump, rotation of the impeller will transfer energy from the motor to the fluid. Thereby the fluid is accelerated radially outward from the centre of rotation. In the impeller-stator spinning disc reactor, the impeller has the same function. The impeller is used to transport liquids radially outwards, from the center of rotation to the rim of the impeller. A side view of the impeller-stator spinning disc reactor is given in **Figure 1**. The direction of liquid flow in the impeller-stator configuration is shown in the close up of the impeller in **Figure 1**.

Using an impeller instead of a solid rotor, allows for the selective through flow of the liquid with lower density while the liquid with higher density remains in the reactor (van der Schaaf et al., 2012). This is schematically shown in **Figure 2**. Accordingly, a consecutive sequence of mixing and separation is described (Visscher et al., 2012a). This is an important step toward counter-current liquid-liquid extraction (Trambouze et al., 2002). Information about the liquid-liquid flow behavior in the impeller-stator configuration allows for a qualitative estimation of the liquid-liquid mass transfer rate in impeller based centrifugal extractors (Visscher et al., 2012a).

This chapter describes the liquid-liquid flow behavior in the impeller-stator spinning disc reactor by six flow regimes. These regimes are qualitatively described as a function of the rotational speed of the impeller and the aqueous volume fraction. The regime transitions are dependent on the formation of boundary layers on the impeller and the stator, the shear stress intensity and the aqueous volume fraction. Also, the requirements for selective through flow of *n*-heptane are discussed.

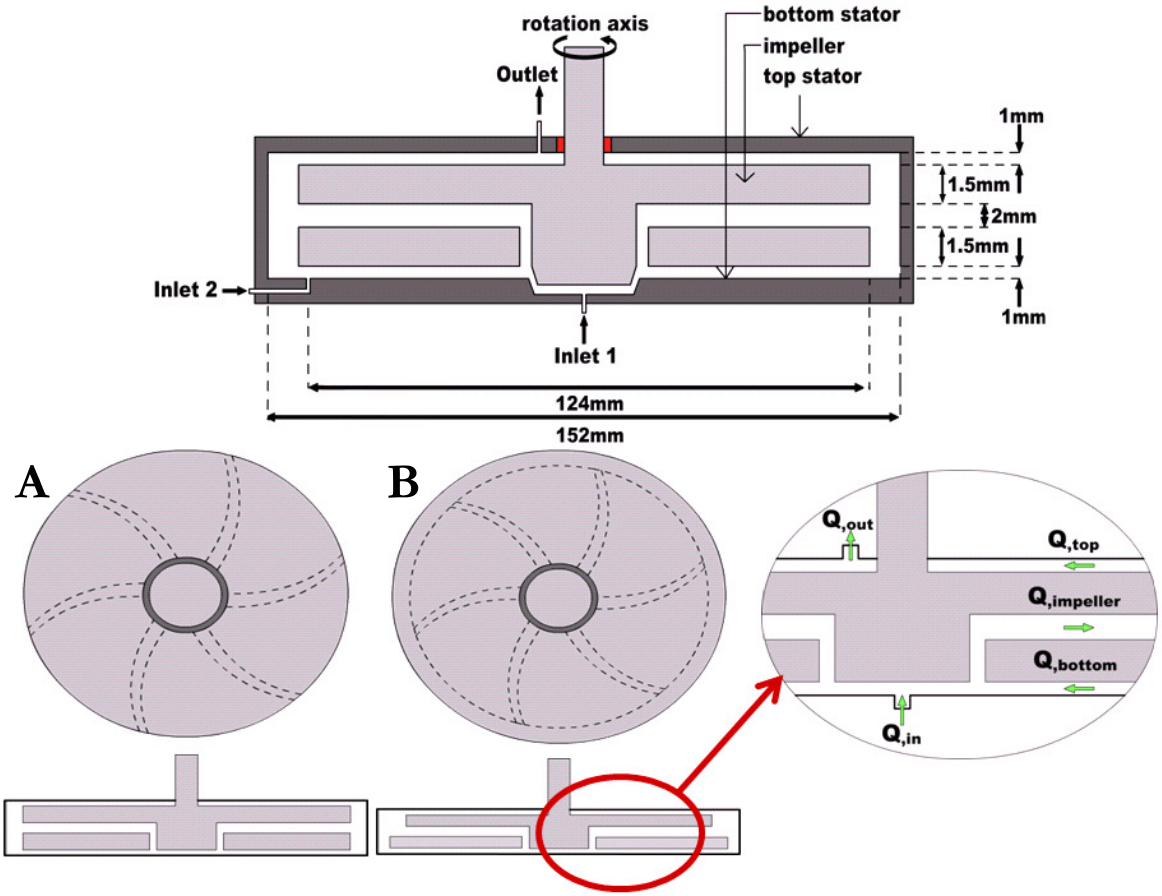

Figure 1. Top: schematic side view of the impeller-stator spinning disc reactor. Bottom: side view and top view of the impeller-stator spinning disc reactor. The side view of the reactor is enlarged, showing the direction of liquid flow. In impeller A the opening for radial outflow is located at the rim (radius 66 10^{-3} m). For impeller B the top plate (radius 63 10^{-3} m) is smaller than the bottom plate (radius 73 10^{-3} m).

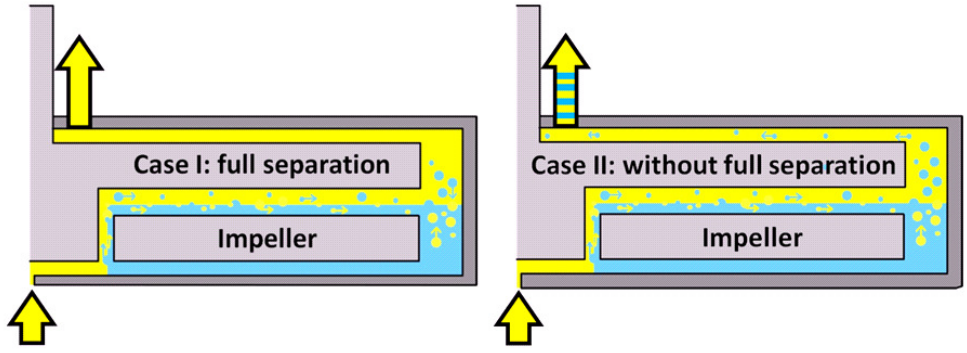

Figure 2. Schematic representation of Case I: *n*-heptane (yellow) is continuously fed to the reactor through inlet 1 (Figure 1) and flows through the impeller ($Q_{impeller}$ in Figure 1). At the rim of the impeller, the density difference prohibits the water droplets (in blue) to flow with the *n*-heptane flow. Accordingly, *n*-heptane flows selectively through the reactor. In Case II: The turbulence intensity at the rim of the impeller overcomes the gravitational force and induces a drag force that drags the water droplets to the reactor outlet. Water and *n*-heptane are not separated. There is no selective through flow of *n*-heptane through the reactor.

5.2. Experimental section

5.2.1. Experimental set-up

The reactor consists of a cylindrical transparent poly(methyl methacrylate) (PMMA) housing with an inner diameter of 0.152 m and an internal height of 7.0 10^{-3} m. Both above and below the impeller the axial clearance between the impeller and the stators equals 1.0 10^{-3} m (Figure 1).

This distance is further denoted as disc spacing. The impeller is constructed out of two concentric circular plates connected by six vanes. Two different impellers were used; their top and side views and the flow directions are schematically shown in **Figure 1**. The constructional details of the impellers are given in **Table 1**. Impeller A is constructed out of stainless steel and has an equal radius for the top and bottom plates, both with a radius of 66 10^{-3} m. Impeller B is constructed out of stainless steel and has a radius of 73 10^{-3} m for the bottom plate, while the top plate has a radius of 63 10^{-3} m. The total liquid volume in the reactor, V_R, equals 66 10^{-6} m³ for impeller A, and 63 10^{-6} m³ for impeller B.

Table 1. Constructional details of the impeller configurations.

Property	Unit	A	B
Material		SS	SS
Radius top disc	M	66.0 10^{-3}	63.0 10^{-3}
Radius bottom disc	M	66.0 10^{-3}	73.0 10^{-3}
Height single disc	M	1.5 10^{-3}	1.0 10^{-3}
Height radial outflow	M	2.0 10^{-3}	2.0 10^{-3}
Empty reactor volume	m^3	66 10^{-6}	63 10^{-6}

The reactor is equipped with two inlets and one outlet. The first inlet is located in the centre of the bottom stator, and is equipped with a ¼" Swagelok® connection. The second inlet is located at 62 10^{-3} m from the centre of the bottom stator as an orifice with a diameter of 1.4 10^{-3} m and a Swagelok® connection of ⅛". The reactor outlet is situated in the top stator at a radius of 33 10^{-3} m from the centre with a ¼" Swagelok® connection.

A calibrated gear pump (E-7500-09, Bronkhorst®) is used to feed the liquids to the reactor, with a maximum flow rate of 15 10^{-5} m^3 s^{-1}. The impeller is propelled with a Re162 lab stirrer from IKA® laboratories. The maximum rotational speed is 1700 RPM. The rotational Reynolds number is defined as $Re_\Omega = \omega r^2 v^{-1}$, and thus is maximized to 7.98 10^5.

5.2.2. Other equipment

Visual observations of the fluid flow were obtained through the bottom stator and show the space of the reactor between rotor and stator. For photographic analysis a Canon® EOS 400D camera was used in combination with a Philips® PR 9113 stroboscope. For milliseconds timescale analysis a MotionPRO® IDT Y-series high-speed camera was used with a maximal frame rate of 1800 frames per second. Light intensity was enhanced by using 4 Dedocool high-intensity light sources.

5.2.3. Chemicals

n-Heptane (99% from Sigma-Aldrich) was used as liquid with the lower density. PMMA is resistant to *n*-heptane. Water was demineralized using a Millipore Elix UV-10 and used as liquid with the higher density. For visualization purposes, 5 10^{-6} m^3 water soluble blue ink was added to 2.2 10^{-3} m^3 of water. Pelican® 4001 royal blue fountain pen ink was used. GC-MS analysis showed that the water soluble ink does not dissolve into *n*-heptane. All experiments were performed at ambient lab temperature, 293 ± 2 K. The density, viscosity, and surface tension of *n*-heptane and water at 293 K are shown in **Table 2** (Visscher et al., 2011).

Table 2. Density, ϱ / kg m^{-3}, viscosity, μ / kg m^{-1} s^{-1}, surface tension, σ / mN·m^{-1}, and interfacial tension, γ_{org-aq} / mN·m^{-1}, of water, *n*-heptane, water+ethylene glycol, and *n*-dodecane at 293 K. The presence of ink is not taken into account for these data (Visscher et al., 2011, Tsierkezos et al., 1998, Caudwell et al., 2004, Goebel et al., 1997).

Property	Water	*n*-Heptane	Water+ 30v% ethylene glycol	*n*-Dodecane
Density	0.99 10^3	0.68 10^3	1.04 10^3	0.75 10^3
Viscosity	1.02 10^{-3}	0.39 10^{-3}	1.99 10^{-3}	1.34 10^{-3}
Surface tension	72.58	20.05	62.29	25.30
Interfacial tension		51.90		53.70

5.2.4. Experimental procedure selective through flow

To study the selective through flow of *n*-heptane through the reactor that was explained in **Figure 2**, the reactor was initially completely filled with *n*-heptane. After addition of a predefined water volume, the *n*-heptane flow is set to 12.6 10^{-6} m^3_{ORG} s^{-1}. The *n*-heptane flow is fed to the reactor through inlet I in the bottom stator and flows out of the reactor though the outlet in the top stator. The rotational speed was increased from 0 to 400 RPM (Re_Ω= 0.188 10^6) by steps of 50 RPM. Rotation of the impeller induces a flow of liquid through the impeller: both *n*-heptane and water will flow through the impeller. At the impeller outlet, at the rim of the impeller, there are two possibilities which are schematically shown in **Figure 2**. In Case I the density difference between water and *n*-heptane causes separation of the water droplets and the *n*-heptane. In Case II, the water droplets are entrained in the *n*-heptane. Thus, either selective through flow of *n*-heptane is accomplished (Case I, **Figure 2)** or *n*-heptane with entrained water droplets flows out of the reactor (Case II, **Figure 2**).

5.2.5. Experimental procedure liquid-liquid flow

To study the liquid-liquid flow between the impeller and the bottom stator, the reactor was completely filled with *n*-heptane in absence of rotation. The aqueous volume fraction is equal to 0 m^3_{AQ} m^{-3}_{L}. Then a predefined amount of water was added to the reactor through inlet 2 (**Figure 1**). The aqueous volume fraction in the reactor was calculated from the reactor volume and the injected water volumes. At a given aqueous volume fraction the rotational speed was increased stepwise from 0 to 300 RPM (Re_{Ω}= 1.41 10^5), with an increase of 25 RPM per step. At each rotational speed of the impeller, twenty minutes were taken to ensure that a stable flow regime was obtained.

5.2.6. Experimental procedure pump curve

The pumping capacity of the impeller was determined as is shown in **Figure 3A**, for rotational speeds up to 900 RPM. The height between the level in the feeding vessel and the point of outflow was kept constant at 85 10^{-3} m. At different rotational speeds liquid was collected in a graduated cylinder over a time span of 60 seconds. By assuming a steady state flow, an average volumetric flow rate was determined. For the determination of the head, the setup of **Figure 3B** was used. The maximum head delivered by the impeller was determined by measuring the liquid level in the hose connected to the reactor outlet.

A plot of the pumping capacity versus the head is called a pump curve, and is commonly used to represent pump performance (Coulson et al., 2007). For this set-up the pump curve was obtained by measuring the head and the pumping capacity at a given rotational speed. For these experiments the reactor was filled with different aqueous volume fractions, ranging from 0 to 0.8 m^3_{AQ} m^{-3}_{L}. An *n*-heptane flow of 0.126 10^{-3} m^3 s^{-1} was fed to the reactor through inlet 1 in the bottom stator (see **Figure 1**).

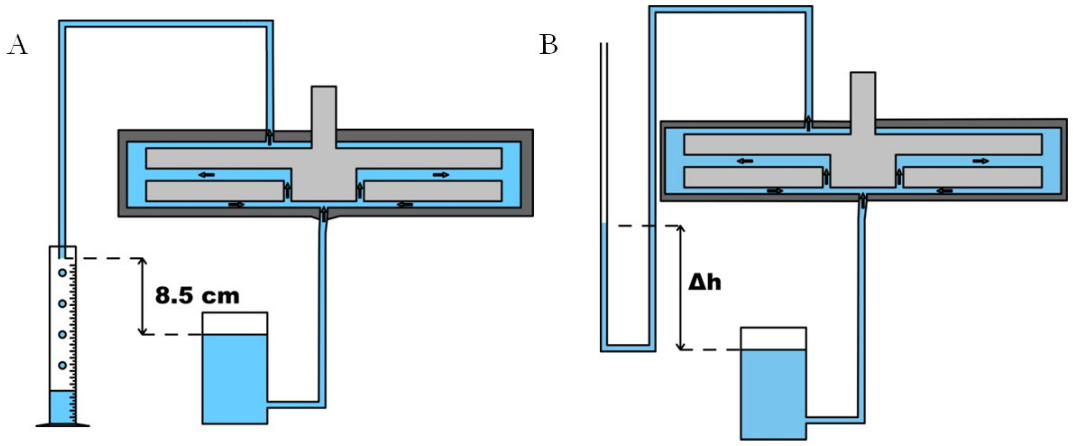

Figure 3. The experimental set up used to determine the maximum pumping capacity (in m^3 s^{-1}) (A) and the maximum head (B) that can be generated from the impeller.

5.3. Results and discussion

5.3.1. Selective pumping of the impeller

Selective through flow of *n*-heptane through the reactor is obtained depending on the rotational speed and the aqueous volume fraction. The flow and pressure generated can be described by common pump affinity laws. **Figure 4** shows the critical rotational speed at which the selective through flow of *n*-heptane is no longer possible, as a function of the aqueous volume fraction.

This critical rotational speed decreases with an increasing aqueous volume fraction. Selective pumping is possible up to rotational speeds of 400 RPM (Re_{Ω}= 1.88 10^5) when an aqueous volume fraction of 0.08 m^3_{AQ} m^{-3}_{L} is present in the reactor. For an aqueous volume fraction of 0.6 m^3_{AQ} m^{-3}_{L} this is possible up to 160 RPM.

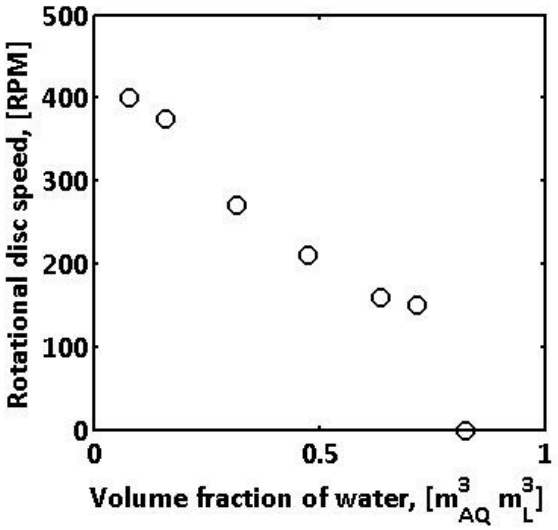

Figure 4. The rotational speed (at which water is dragged along to the reactor outlet with a superimposed through flow of *n*-heptane) versus the aqueous volume fraction.

Increasing the rotational speed of the impeller increases the volumetric flow rate through in the impeller ($Q_{IMPELLER}$, **Figure 1**). Also the mixing intensity at the rim of the impeller is increased. Separation of the two liquids becomes more difficult to achieve. When the *n*-heptane-water interface is located at the same height as the impeller outlet, separation of the liquids is no longer possible. The selective *n*-heptane pumping cannot be achieved anymore. This phenomenon is observed at an aqueous volume fraction of 0.8 m^3_{AQ} m^{-3}_{L}.

5.3.2. Flow regimes

Six different flow regimes were observed in the space between the impeller and the bottom stator, as a function of the rotational speed and the aqueous volume fraction. In all experiments the volume between the impeller and top stator was selectively filled with *n*-heptane. This is due to the density difference, which causes the more dense liquid (water) to be located preferentially below the lighter phase (*n*-heptane).

For the experiments with continuous through flow in the rotor-stator SDR, the volume fraction of *n*-heptane were close (+/- 10%) to the ratio of the volumetric *n*-heptane flow rate over the total volumetric flow rate (Visscher et al., 2012b).

The observed flow regimes in this impeller-stator spinning disc reactor were distinguished by the liquid that is present as the continuous phase and by the degree of dispersion of the dispersed phase. The representation of the flow regimes as a function of the rotational speed and the aqueous volume fraction is further denoted as the flow map. The characteristics of the flow regimes that are shown in the flow map in **Figure 5** are given in **Table 3**. In the following section each flow regime is described in more detail. The graphical representation of each regime consists of a photographic image, a schematic bottom view and a schematic side view.

5.3.2.1. Full water regime

A known amount of water was fed to the reactor through inlet 2 after completely filling the reactor with *n*-heptane. Upon the addition of water to the reactor, the space between the impeller and the bottom stator fills up with water. When observed from the bottom side, *n*-heptane is only visible at the rim of the reactor (**Figure 6)**. There is no dispersion of *n*-heptane in water when the impeller rotation is absent or low. Both, the space between the impeller and the bottom stator, and the space inside the impeller fill up with water when the aqueous volume fractions exceeds 0.21 m^3_{AQ} m^{-3}_{L} (impeller A) or 0.27 m^3_{AQ} m^{-3}_{L} (impeller B) (**Figure 7**). For both situations the *n*-heptane phase is located above the water layer.

5.3.2.2. Stagnant ring regime

The injected volume of water forms a symmetrical ring below the impeller located around inlet 1 when the aqueous volume fraction is lower than 0.22 m^3_{AQ} m^{-3}_{L} and the rotational speed is lower than 50 RPM (Re_Ω= 23.5 10^3) **(Figure 8)**. The radial position of the ring depends on the rotational speed. The water ring is attached to the rim of the impeller when the rotational speed is lower than 25 RPM (Re_Ω= 11.7 10^3). The ring moves radially inwards until it reaches a steady state end position when the rotational speed is increased.

5.3.2.3. Water droplet regime

The water droplet regime is observed when the rotational speed is higher than 225 RPM (Re_Ω= 0.106 10^6) and the aqueous volume fraction is below 0.2 m^3_{AQ} m^{-3}_{L}. At this rotational speed, the shear force between the impeller and the stator disperses water into the *n*-heptane (**Figure 9**). The water droplet diameter is smaller than 1 10^{-3} m at 300 RPM (Re_Ω= 0.141 10^6). With increasing rotational speed, the water droplet diameter decreases further. The droplet diameter could not be determined sufficiently accurate below 1 10^{-3} m.

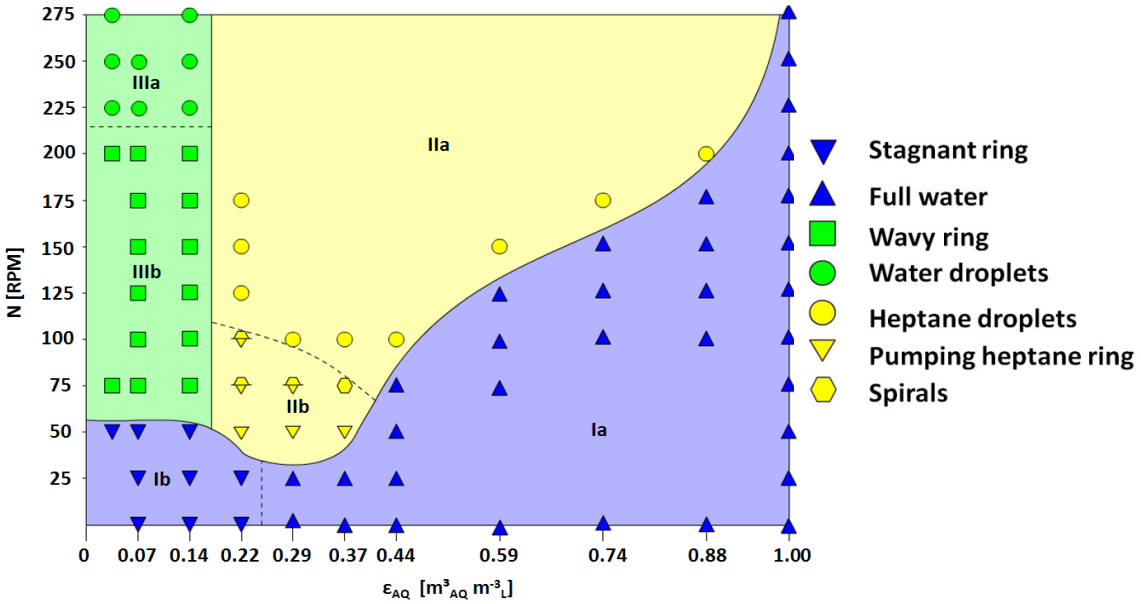

Figure 5. Flow regimes for impeller A (Figure 1), for the *n*-heptane-water mixture, as a function of the aqueous volume fraction (ε_{AQ}) and the rotational speed (N). The regimes are listed in Table 3.

Table 3. Flow regime characteristics for the *n*-heptane-water flow.

Regime name	Continuous Phase	Appearance	Symbol
Full water	Both	Homogenous	▲
Stagnant ring	Both	Ring	▼
Heptane droplets	Water	Droplets	○
Heptane spiral & ring	Water	Spiral & ring	▽/⬡
Water droplets	*n*-Heptane	Droplets	●
Wavy ring	*n*-Heptane	Ring	■

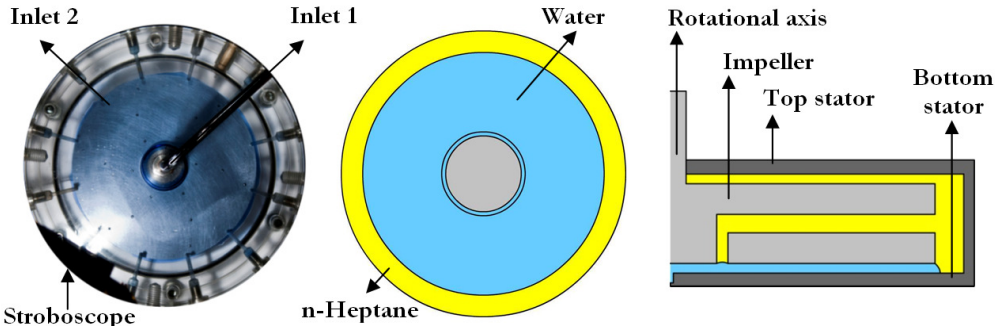

Figure 6. Photograph of the bottom view and schematic representations of the bottom view and the side view for the full water regime. In the schematic representation water appears blue and *n*-heptane yellow.

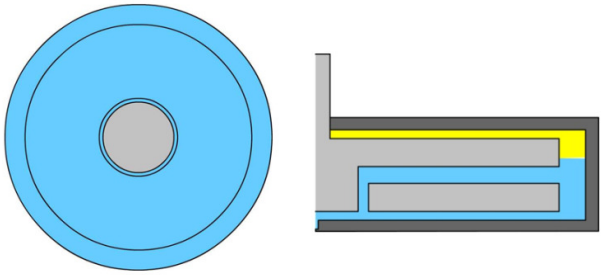

Figure 7. Schematic representations of the bottom view and the side view for the full water regime. Water: blue; *n*-heptane: yellow.

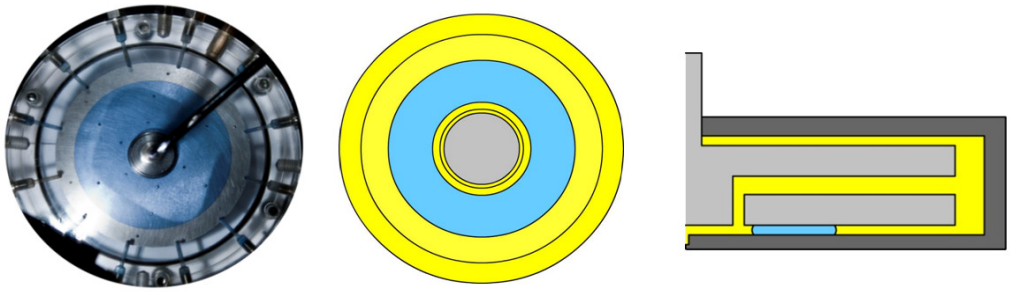

Figure 8. Photograph of the bottom view and schematic representations of the bottom view and the side view for the stagnant ring regime. In the schematic representation water appears blue and *n*-heptane yellow.

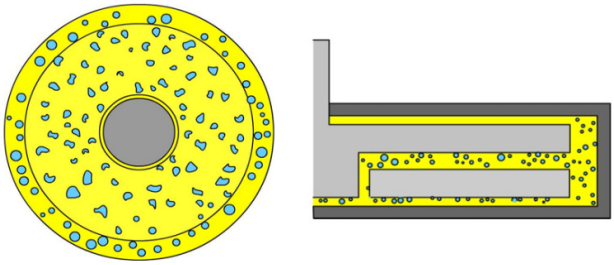

Figure 9. Schematic representations of bottom view and side view of the water droplets regime. Water: blue; *n*-heptane: yellow.

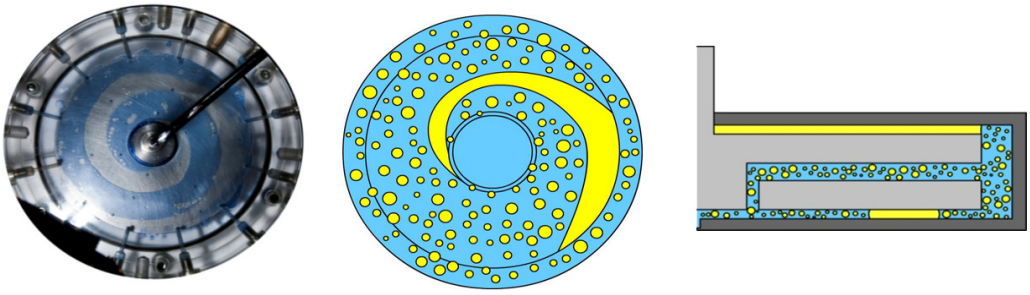

Figure 10. Photograph of the bottom view and schematic representations of the bottom view and the side view for the *n*-heptane spiral and ring regime. In the schematic representation water appears blue and *n*-heptane yellow.

5.3.2.4. Heptane spiral and ring regime

A flow regime with two alternating flow patterns is observed for intermediate values of the rotational speed and the aqueous volume fractions between 0.22 and 0.44 m^3_{AQ} m^{-3}_{L}. In both patterns water acts as the continuous phase. In the first pattern, *n*-heptane is present as spirals (**Figure 10**). In the second pattern, *n*-heptane is present a ring (**Figure 11**). Alternating flow patterns like this will lead to a spread in the measured liquid-liquid mass transfer rates at the given experimental condition. In the ring pattern, initially *n*-heptane is observed as a moving ring. This ring starts near the rim of the impeller and moves symmetrically radially inwards.

This behavior is also observed during the formation of the stagnant ring regime. While moving radially inwards, the ring breaks up at one location and forms an *n*-heptane spiral. *n*-Heptane flows to the impeller inlet through this *n*-heptane spiral, and is pumped to the rim of the impeller where either a new ring or a new spiral is formed. The *n*-heptane ring has a constant thickness. Facing toward the rotational axis, a sharp defined interface is present between the two liquids. At the outside of the ring, facing the rim of the impeller, a diffuse interface exists. A photographic image is shown in close-up in **Figure 11**.

The diffuse interface originates from overlapping boundary layers that exist on the impeller and the stator. The formation of centripetal oriented boundary layer on the rotor and centrifugal oriented boundary layer on the stator has been extensively studied for single phase rotor-stator systems (Harmand et al., 2013*,* Haddadi et al., 2008*,* Poncet et al., 2005b*,* Poncet et al., 2005c*,* Nour et al., 2011*,* van Eeten et al., 2012). With decreasing radius the rotational Reynolds number will decrease. For rotor-systems with through flow this causes the boundary layers near the rotational axis to break down and disappear. In the boundary layer on the impeller, water is forced radially outwards along the impeller. This boundary layer is located above a radial inwards oriented boundary layer in which *n*-heptane is flowing.

5.3.2.5. *n*-Heptane droplet regime

An increase of the rotational speed causes dispersion of *n*-heptane droplets into water when the reactor is operated in the full water regime. This regime is shown in **Figure 12**. The droplet diameter is decreasing with increasing rotational speed. This behavior is similar as is observed for gas-liquid and liquid-liquid flow in the rotor-stator spinning disc reactor (Visscher et al., 2012d). Upon rotation of the impeller, water is pumped through the impeller, as is indicated by the green arrows in the side view that is shown in the close up shown in **Figure 1.** This induces a liquid recycle flow from the bottom center of the reactor toward the rim of the impeller. Due to the density difference of water and *n*-heptane, only water is recycled.

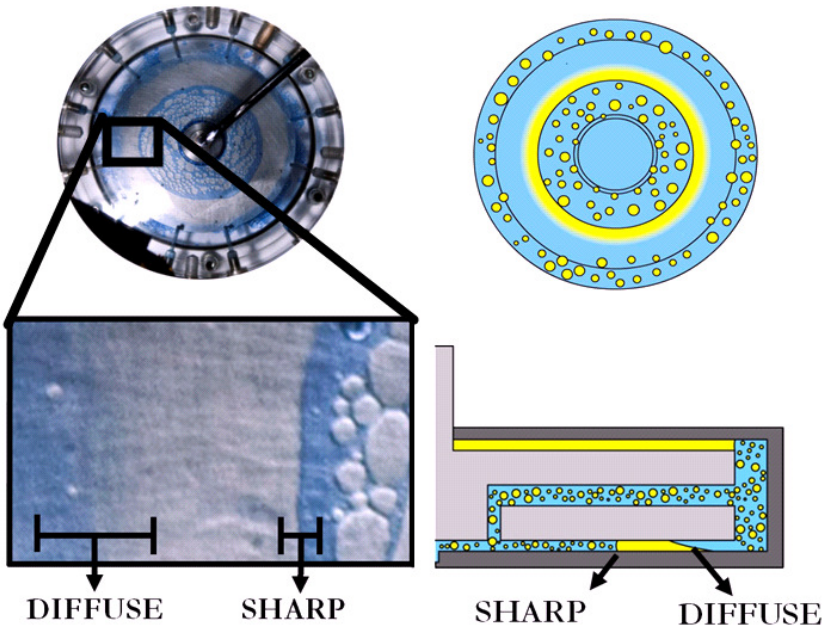

Figure 11. Photographs of the bottom view and a close-up of the water-*n*-heptane-water interface. Also a schematic representation of the bottom view and the side view for the *n*-heptane spiral and ring regime is given. In the schematic representation water appears blue and *n*-heptane yellow. A diffuse interface exists on the side facing the rim of the impeller. A sharp interface exists on the side facing the rotational axis.

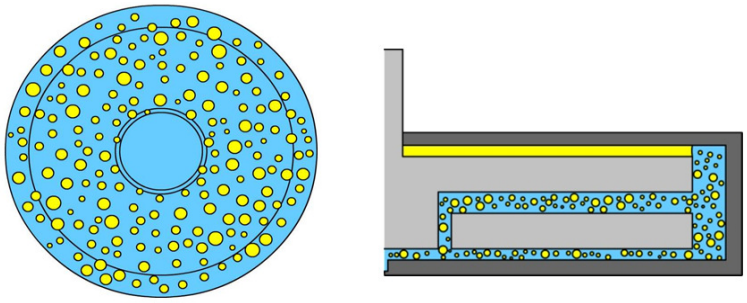

Figure 12. Schematic representations of the bottom view and the side view for the *n*-heptane droplets regime. Water: blue; *n*-heptane: yellow.

The drag force induced by the recycle overcomes the coalescing forces below a critical rotational speed. The drag force acts on the *n*-heptane droplets interface that is perpendicular to the flow direction, accordingly the drag force scales with the *n*-heptane droplet diameter to the power of 2. *n*-Heptane droplets are sheared off at the *n*-heptane/water interface and become dispersed into the water stream. The *n*-heptane droplets are entrained the recycle flow, into the volume between the impeller and the bottom stator. The entrained *n*-heptane droplets in the water flow were confirmed by visual observations in a transparent impeller with equal dimensions as impeller B.

5.3.2.6. Wavy ring regime

A wavy ring regime is observed when the aqueous volume fractions is lower than 0.22 m^3_{AQ} m^{-3}_{L} and the rotational speed is between 50 and 250 RPM (Re_{Ω} between 2.25 10^4 and 1.17 10^5). In this wavy ring regime, *n*-heptane is present at the center the reactor (**Figure 13**, Top). A wavy structure is present at the rim of the impeller, similar to the wavy *n*-heptane-water interface that is observed in the *n*-heptane spiral and ring regime. The radial position at which the wavy ring is formed depends on the rotational speed. The transition radii are shown (**Figure 13**, Bottom) as a function of the rotational speed.

The dependence on the rotational speed can be explained from two competitive mechanisms. At low rotational speeds the boundary layers are formed on both the impeller and on the stator. These layers cause a wavy regime, similar as observed for the *n*-heptane spiral and ring regime. The volumetric flow through the impeller increases with increasing rotational speed. Due to this increased flow inside the impeller, the radial inward oriented flow between the impeller and the bottom stator is also increased. The increased through flow causes the boundary layers to break down at a radius closer to the rim of the impeller (Harmand et al., 2013, Visscher et al., 2012c). This is in accordance with previously published results on boundary layer formation that was observed for single phase flow (Visscher et al., 2012c).

5.3.3. Phase inversion

Six different flow regimes were described as a function of the rotational speed and the volume fraction of water. Both water and *n*-heptane occur as continuous phase. The transition in continuous phase is called phase inversion and occurs at a critical aqueous volume fraction, as is shown in **Figure 14** (Arirachakaran et al., 1989, Norato et al., 1998, Yeo et al., 2000). Phase inversion of the *n*-heptane-water system is a known phenomenon and is not dependent on the rotational speed, which is in accordance with results obtained for a stirred batch reactor (Amouei et al., 2008, Deshpande et al., 2012). The influence of the aqueous to organic viscosity ratio on the occurrence of phase inversion is under debate (Selker et al., 1965, Norato et al., 1998). In general, when the viscosity of a phase is increased, its tendency to be dispersed is also increased.

5.3.4. Flow map

To study the general applicability of the reported flow map, the flow map was studied for an aqueous to organic viscosity ratio ranging from 0.76 to 5.12. The influence of the viscosity ratio was small, i.e. the same regimes were observed. The flow maps measured at the three different viscosity ratios are shown in **Figure 15** (0.76), **Figure 5** (2.62) and **Figure 16** (5.10). The influence of the viscosity range (0.76 - 5.10) on the flow map is small.

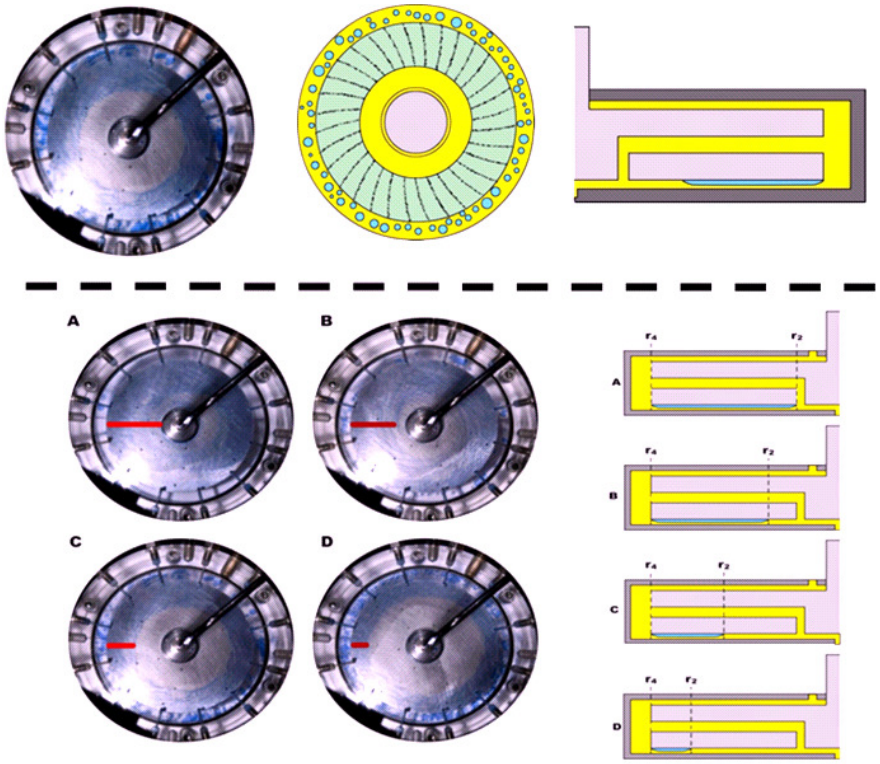

Figure 13. Top: photograph of bottom view and schematic representations of bottom view and side view of the wavy ring regime. In the schematic representation water appears blue and *n*-heptane yellow. Bottom: the wavy ring regime as a function of increasing rotational speed. All experiments are performed at an aqueous volume fraction of 0.15 m^3_{AQ} m^{-3}_{L}. The rotational speed equals 75 RPM (Re_{Ω}= 35.2 10^3) for picture A, 150 RPM (Re_{Ω}= 70.4 10^3) for picture B, 175 RPM (Re_{Ω}= 82.1 10^3) for Picture C, and 200 RPM (Re_{Ω}= 93.8 10^3) for Picture D. In the photographs, the radial length of the water volume is marked with a red line.

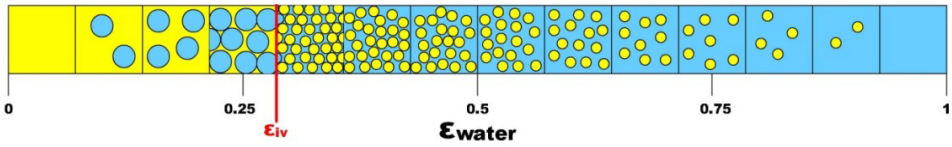

Figure 14. Water-in-*n*-heptane dispersion changes into heptane-in-water dispersion on the point of phase inversion when aqueous volume fraction is increased (Arirachakaran et al., 1989). Water: blue; *n*-heptane: yellow.

This is in contradiction with previous published results on the phase inversion of the *n*-heptane/water system. The reported flow map is thus general applicable within the rotation speed ranging from 0 to 275 RPM (Re_{Ω}= 0.129 10^6), the aqueous volume fractions ranging from 0 to 1 m^3_{AQ} m^{-3}_{L}, and a viscosity ratio of 0.76 to 5.12.

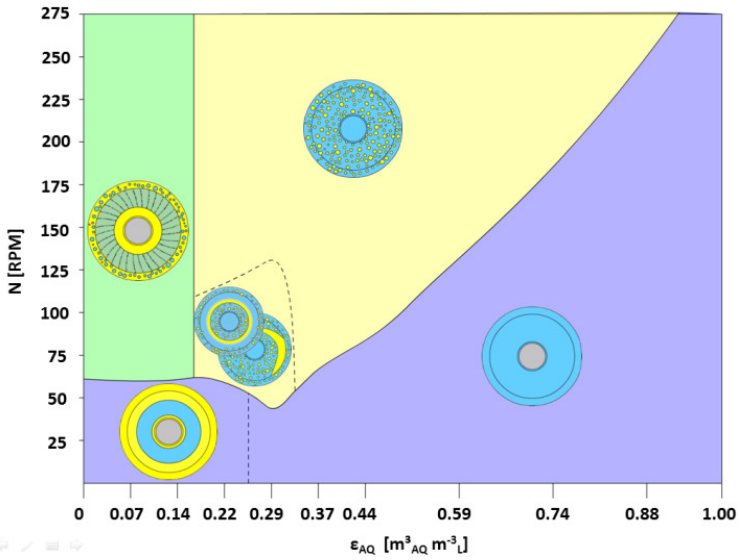

Figure 15. Flow map for the dodecane/water system with the observed regimes as a function of the rotational speed and the aqueous volume fraction. The viscosity ratio is 0.76. When compared to the *n*-heptane-water flow map, the water droplet regime is absent. The map is determined using impeller B, see Figure 1.

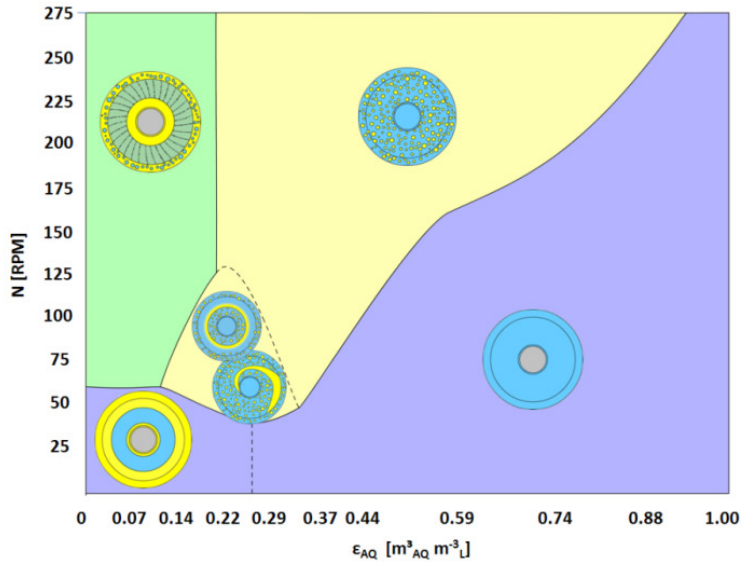

Figure 16. Flow map for the water-30% ethylene glycol/*n*-heptane system with the observed regimes as a function of the rotational speed and the aqueous volume fraction. The viscosity ratio equals 5.12. The map is determined using impeller B, see Figure 1.

5.4. Conclusions

Liquid-liquid flow in an impeller-stator spinning disc reactor is described. The impeller has a comparable function as the impeller in a centrifugal pump, and transports liquid from the bottom center to the rim of the impeller. The impeller-stator configuration is able to selectively pump the lighter liquid phase through the reactor, whilst it is intensively mixed with a heavier liquid phase that remains in a stage of the reactor.

Combining mixing and separation in one compact reactor is an important step toward a counter-current operated impeller-based centrifugal extractor. Water and *n*-heptane were contacted rotational speeds between 0 and 900 RPM (Re_{Ω}= 4.22 10^5), and aqueous volume fractions between 0 and 1 m^3_{AQ} m^{-3}_{L}. Six different flow regimes were observed in the space between the impeller and the bottom stator. Dispersion is absent in the full water regime (rotational speed below 50 RPM) and the stagnant ring regime. Water is the dispersed phase in the water droplets regime (rotational speed above 200 RPM) and wavy ring regime (rotational speed between 50 and 200 RPM). *n*-Heptane acts as the dispersed phase in the *n*-heptane droplets regime and the spiral and ring regime. Flow regime transitions are dominated by three effects: the formation of boundary layers on the impeller and the stator, the shear stress intensity and the aqueous volume fraction. With this information about the liquid-liquid flow behavior in the impeller-stator configuration, a qualitative estimation of the liquid-liquid mass transfer rate in an impeller based centrifugal extractors is possible.

Nomenclature

Roman symbols

H	Head, m
N	Rotational speed, RPM
Q	Volumetric flow rate, m^3 s^{-1}
R	Radius, m
Re_{Ω}	Rotational Reynolds number, $\omega R^2 \upsilon^{-1}$
SS	Stainless steel
V	Volume, m^3

Greek letters

γ	Interfacial tension, $mN \cdot m^{-1}$
ε_{AQ}	Aqueous volume fraction, m^3_{AQ} m^{-3}_{L}
μ	Viscosity, kg m^{-1} s^{-1}
ϱ	Density, kg m^{-3}
σ	Surface tension, $mN \cdot m^{-1}$
υ	Kinematic viscosity, m^2 s^{-1}
ω	Rotational disc speed, rad s^{-1}

Sub- and superscripts

ORG	Organic
AQ	Aqueous
L	Liquid
R	Reactor
IV	Inversion

6. Counter-current liquid-liquid extraction in a high-gravity extractor

This chapter has been submitted for publication:

F. Visscher, S. Saffarionpour, M.H.J.M. de Croon, J. van der Schaaf, J.C. Schouten, "**Counter-current liquid-liquid extraction in a high-gravity extractor",** A*IChE Journal*, 2013.

Abstract

Liquid-liquid extraction is a common separation technique in the chemical industry. Most industrial extractions are performed in equipment that requires large inventories and long processing times. A counter-current liquid-liquid extractor is demonstrated here that uses high-gravity conditions for the subsequent contacting and separation of *n*-heptane and water. This extractor is based on rotor-rotor spinning disc technology, and processes up to 5 m^3 liquid per day. The height of a transfer unit, and thus the extractor volume, is ten times lower as compared to other types of centrifugal extractors. Liquid-liquid extraction processes can therefore be intensified.

6.1. Introduction

Liquid-liquid extraction is a purification technique based on the distribution of a solute over two liquid phases (Muller et al., 5008). It is used for a wide range of applications in the chemical industries (e.g., in oil refineries to separate aromatics from aliphatic hydrocarbons, in the food industry to produce vitamins, and in biotechnology to produce temperature sensitive compounds). In 1805, F.W. Sertüner used liquid-liquid extraction to purify morphine (Klockgether-Radke, 2002).

At that time, liquid-liquid extraction was executed batch wise, i.e., over a repetitive sequence of mixing and separation steps. In current practice, extraction is performed in gravity-driven, continuously operated equipment (Míšek, 1994). Counter-current flow of the two fluids is essential for an efficient extraction process: there is cross-over of the solute between two liquids that are flowing in opposite directions. In the chemical industry counter-current operated equipment can have volumes up to 700 m^3 (Trambouze et al., 2002).

Such equipment can be a mixer-settler sequence (Hashtochahar et al., 2010), a Kuhni column (Gomes et al., 2009), a packed column (Varteressian et al., 2002), or a rotating disc contactor (Al-Rahawi, 2007, Trambouze et al., 2002). The large volume is required when liquids with a small density difference (<10%) are separated. Centrifugal extractors were developed to reduce the equipment volume and processing time with two orders of magnitude and to enhance the separation efficiency over 99.9% (Gebauer et al., 1982).

In centrifugal extractors, the settling effect of the density difference is exploited in combination with the centrifugal force. In addition, the liquids are mixed more intensely due to the fact that they accelerate and decelerate radially. Such extractors, such as the Podbielniak extractor (Barson et al., 1953, Podbielniak et al., 1959), the annular centrifugal extractor (Deshmukh et al., 2007), and the Westfalia/Luwesta extractor (Likidis et al., 1989), reduce the equipment volume but are hard to scale up in terms of maximum through flow. Multiple contacting stages are needed to achieve sufficient mass transfer. Full separation of the two liquid phases between each contacting stage is essential. Incomplete separation of the two liquid phases will decrease the number of contacting stages in the equipment and will thus lead to an increase of the inventory volume (Ingham et al., 2007). For existing centrifugal extractors like the annular centrifugal and the Podbielniak extractor, every additional contacting step requires a new entire module, which implies a multiplication of the required inventory volume.

This chapter describes the ability of a counter-current operated centrifugal extractor to consecutively mix and separate two immiscible liquids. The realized extractor has a liquid volume of 100 10^{-6} m^3 and is able to separate 5 m^3 of mixture per day.

This is comparable to flow rates used in the fine chemical industry. The extractor is based on spinning disc technology, which is known for its excellent performance to contact liquid-liquid, liquid-gas, and liquid-solid mixtures (Visscher et al., 2012d, van der Schaaf et al., 2011, Meeuwse et al., 2010b, Meeuwse et al., 2012). In this chapter, the separation efficiency of the device is illustrated by the separation of an immiscible oil-water mixture, represented by water and *n*-heptane.

The extractor presented in this chapter opens up the application of liquid-liquid separations at locations where equipment needs to handle rapidly changing feed streams, and at locations where floor area or gravity is limited, e.g., offshore oil drilling platforms or in outer space. Purification and recycling processes are essential for sustainable life support in space.

For example, the Environmental Control and Life Support System (ECLSS) uses vapor compression distillation to re-process urine on board the International Space Station (ISS) (Parker et al., 1999). Centrifuge enhanced liquid-liquid extraction has not been applied in space, but will be necessary in the long term to reduce the consumption of raw materials and to reduce energy usage.

6.2. Experimental section

6.2.1. Experimental set-up

A schematic side view of the extractor is depicted in **Figure 1.** A single contacting stage consists of an impeller, which is enclosed by a co-rotating enclosure. The combination of the enclosure-impeller-enclosure gives a rotor-impeller-rotor sequence. Two weirs co-rotate adjacent to the cylindrical enclosure. The impeller (light grey) has a maximum diameter of 170 10^{-3} m and is enclosed in a co-rotating cylindrical enclosure (dark grey) with an inner diameter of 180 10^{-3} m (van der Schaaf et al., 2012). The central shaft and the impeller are made of stainless steel. The external housing (enclosure) and the weirs are made of poly(methyl methacrylate) (PMMA) for visualization purposes.

A schematic cross section of the single-stage extractor is shown in **Figure 1.** The impeller is schematically shown in **Figure 2**. The impeller consists of a top disc with a diameter of 146 10^{-3} m and a bottom disc with a diameter of 170 10^{-3} m. The inner diameter of the extractor is equal to 180 10^{-3} m. The outer diameter of the single-stage extractor is equal to 242 10^{-3} m. The top and bottom discs are connected by six vanes with a height of 2 10^{-3} m. Two weirs are mounted on the rotating enclosure. The weirs have a thickness of 1 10^{-3} m. The spacing between the impeller and the weirs, as well as the spacing between the weirs and the enclosure is equal to 1 10^{-3} m. The maximal distance between the impeller and the enclosure is thus maximized to 3 10^{-3} m.

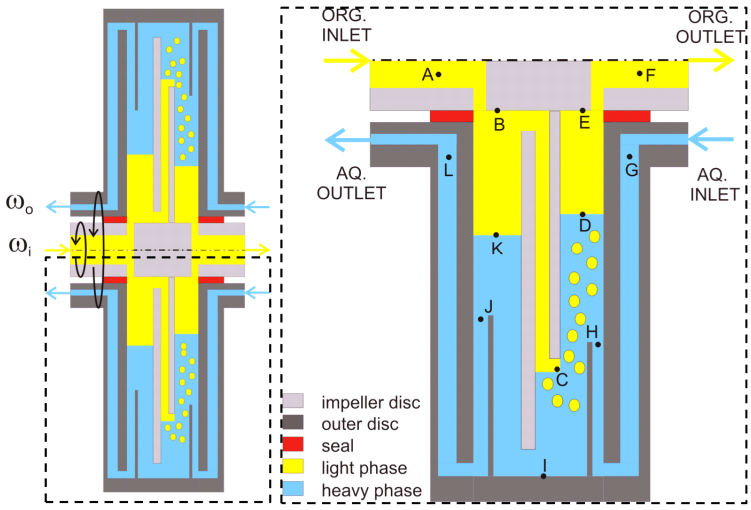

Figure 1. Schematic side view of a single-stage spinning disc based extractor. The impeller (light grey) pumps a liquid with lower density (yellow) from left to right, via *A*, *B*, *C*, *D*, *E*, to *F*. The liquid with higher density (blue) is simultaneously fed from right to left, via *G*, *H*, *I*, *J*, to *L*. At the impeller outlet, *C*, the liquid with lower density is dispersed in to the liquid with the higher density, thereby generating high interfacial area.

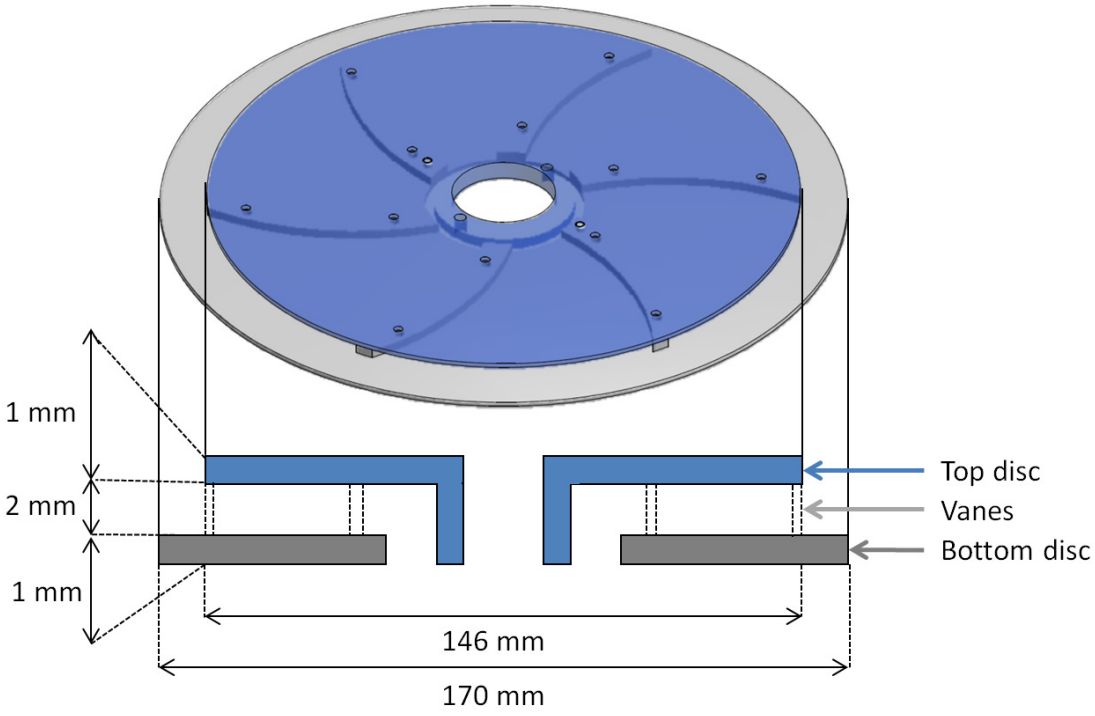

Figure 2. Schematic top view and side view of the stainless steel impeller used in the single-stage and three-stage extractor. Six vanes connect the top disc to the bottom disc. The entire set of the top disc (blue), bottom disc (grey) and vanes forms an impeller. Upon counter-clock wise rotation of the impeller, a pressure gradient between the impeller inlet at the center and the outlet at the rim will cause a liquid flow.

6.2.2. Operational principle

The impeller pumps the liquid with the lower density (yellow) from left to right (**Figure 1**, *A* to *F*) and operates similar to the impellers used in centrifugal pumps (Coulson et al., 2007, Visscher et al., 2012a). Simultaneously the liquid with the higher density is fed from right to left (**Figure 1**, *G* to *L*). Both liquids are in intimate contact at the rim of the impeller **(Figure 1**, *C),* where the liquid with lower density is dispersed into the liquid with the higher density. The two liquids are mixed by the turbulence generated by the difference in rotation speed of enclosure and impeller.

Liquids present in the volume between the enclosure and the weirs are susceptible to the centrifugal force. The phase with the lower density (heptane, yellow) is therefore forced radially inwards, and the phase with the higher density (water, blue) is forced radially outwards. Due to the density difference between water and heptane, the heptane droplets cannot pass though the volume between the weir and the adjacent enclosure. This separation principle is also applied in the mixer-settler combination, which is currently the common workhorse of liquid-liquid extraction (Hashtochahar et al., 2010, Brunner, 2009). Multi-stage contacting can be obtained by repeating the sequence of rotor-impeller-rotor.

6.2.3. Extractor volume

A schematic sideview of the complete extractor is shown in **Figure 3**. The extractor volume occupied by either water or heptane is marked in red. This volume equals 192 10^{-6} m³. The extractor volume where mass transfer occurs is lower and equals 139 10^{-6} m³. This volume is marked green in **Figure 3**.

6.2.4. Materials

Water and *n*-heptane were selected as liquids to demonstrate the separation efficiency of the extractor. These liquids were used as a test system for the determination of liquid-liquid mass transfer rates (Visscher et al., 2011, Visscher et al., 2012d). *n*-Heptane was obtained from Sigma-Aldrich (99 v%). For all experiments, demineralised water was used. The demiwater was purified with a Millipore Elix UV-10 machine. Pelikan Royal Blue ink was used as a dye for the water phase in the visualization experiments. No further purification was performed on the chemicals. All experiments were performed at ambient laboratory temperature. The physical properties of the used chemical systems at 293 K are given in **Table 1.**

Table 1. Density, ϱ / kg m^{-3}, viscosity, η / kg m^{-1} s^{-1}, benzoic acid solubility, *S* / mol%, and interfacial tension with water, σ / mN m^{-1}, at 293 K for water and *n*-heptane (Visscher et al., 2011).

Property	ϱ / kg m^{-3}	η / kg m^{-1} s^{-1}	*S* / mol%	σ / mN m^{-1}
Water	998.2	1.02 10^{-3}	4.95 10^{-4}	-
n-Heptane	683.7	0.39 10^{-3}	1.17	51.24

6.2.5. Experimental approach

Water and heptane are contacted in countercurrent mode at aqueous to organic flow ratios ranging from 1:1 to 1:5 with a maximum total flow rate of 5.1 m³ mixture per day. The residence time for each phase thus varies from 2 to 70 seconds. The separation efficiency of the extractor is determined as a function of the rotational speeds and the flow ratio. The maximum rotational speeds of both the impeller and the rotational enclosure is limited to 700 RPM. The separation efficiency is determined by collecting the volume at the aqueous and organic outlets (**Figure 1,** F and L) over 60 seconds in a (calibrated) graduated cylinder of 500 10^{-6} m³. The separation efficiency is defined as the ratio of the volume of the desired liquid over the total collected volume in the graduated cylinder (eqs. (1) and (2)).

$$\text{Aq} : \frac{V_{AQ}}{V_{AQ} + V_{ORG}} \cdot 100\% \quad (1)$$

$$\text{ORG} : \frac{V_{ORG}}{V_{AQ} + V_{ORG}} \cdot 100\% \quad (2)$$

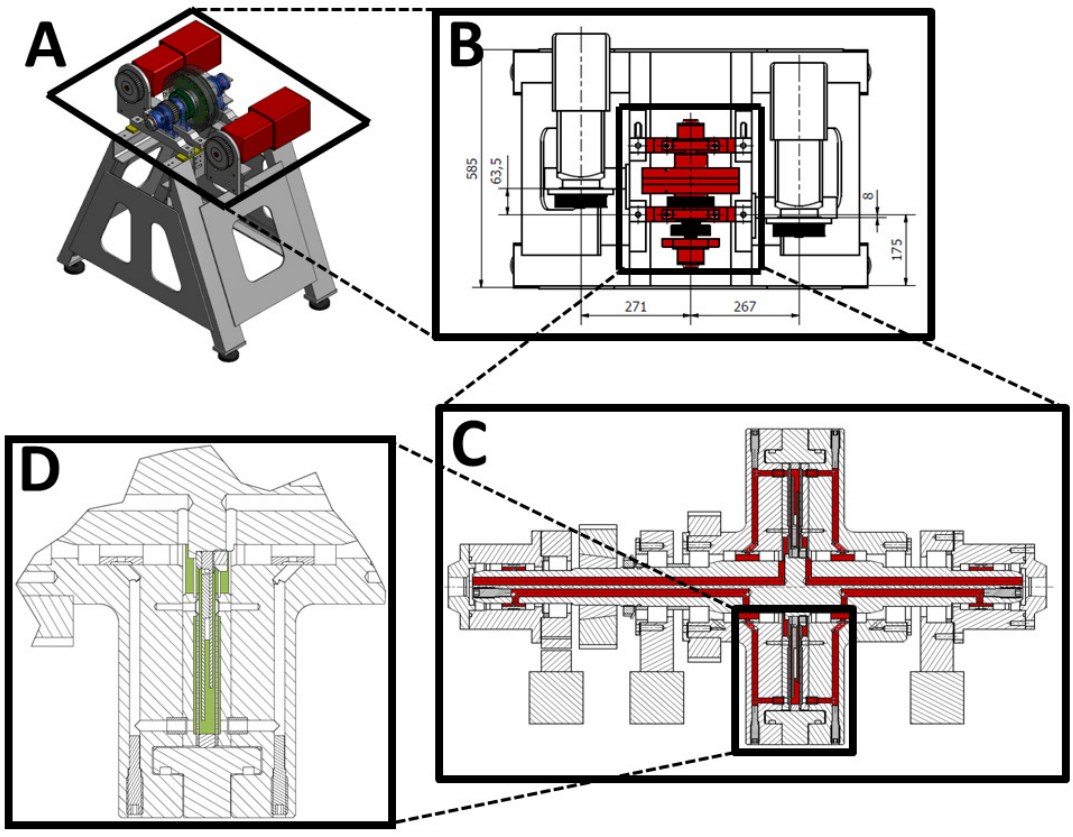

Figure 3. Schematic view of the extractor. (A) Extractor, (B) Top view, (C) Side view with the total extractor volume available for fluid marked red. (D) Enlarged zoom where the volume in which mass transfer can occur is marked green.

6.2.6. Mass transfer experiment

A heptane solution with a benzoic acid concentration of 50 mol m^{-3} was made by dissolving 15.27 g in 2.5 10^{-3} m^3 of heptane. Mass transfer experiments were performed by contacting a benzoic acid rich heptane solution with a benzoic acid free water solution. The physical properties of heptane and water are collected in Table 1. Steady state operation of the single-stage extractor was awaited for approximately six residence times of both phases. The benzoic acid concentrations in heptane and water were measured with offline UV-VIS equipment.

6.3. Results and discussion

6.3.1. Liquid-liquid separation

Water and heptane are contacted in counter-current mode in the extractor (**Figure 1**) as a function of the rotational speeds of the impeller and of the enclosure. The separation efficiency is determined at both outlets (**Figure 1**, points L and F) and is shown in **Figure 4**. Both rotational speeds were limited to 700 RPM. Equal flow rates of water and *n*-heptane were applied of 5 10^{-6} m^3 s^{-1}. At 450 RPM of the impeller and 350 RPM of the enclosure, a separation efficiency >99.9% is obtained for both outlets.

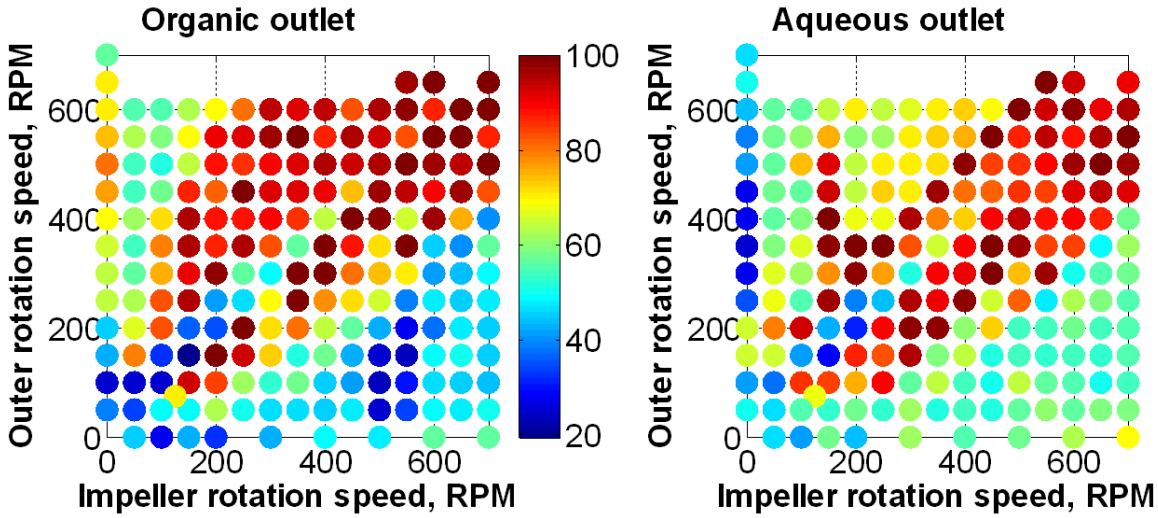

Figure 4. The separation efficiency of the spinning disc extractor is shown as a function of the rotational speeds of the impeller and the enclosure. Both the separation efficiency at the organic outlet (left) and the aqueous outlet (right) are shown. The highest separation efficiency is achieved when the rotational speed of the enclosure is close to that of the impeller. Separations are determined at aqueous and organic phase flow rates of 5 10^{-6} m^3 s^{-1}. The separation efficiency is scaled from 20% (blue) to 100% (red).

Three main conclusions are drawn based on **Figure 4**. First, the highest separation efficiency is achieved when the rotational speed of the enclosure is close to the rotational speed of the impeller. Second, a higher separation efficiency is obtained when the enclosure is rotating faster than the impeller. Third, the separation efficiency at the organic outlet (**Figure 1**, point F) is higher than the separation efficiency determined at the aqueous outlet (**Figure 1**, point L).

A higher separation efficiency is achieved in the single-stage extractor when the rotational speed of the impeller and the enclosure are in close proximity, i.e., when the difference in rotational speeds is below 100 RPM. Under these conditions, larger heptane droplets are created because the shear stress between the impeller and the rotating enclosure is low. This relation between shear stress and droplet size has previously been observed in rotor-stator spinning disc configurations (Meeuwse et al., 2010b, Visscher et al., 2012a, Visscher et al., 2012b). Since the settling velocity of droplets increases with the square root of the droplet diameter, larger droplets are easier to separate.

For single phase flow in rotor-rotor systems, a radial inward flow in a boundary layer is present when the enclosure is rotating faster than the impeller (Will et al., 2009). Boundary layer development for multiphase flow in rotor-rotor or rotor-stator systems has not been described in the literature. We assume that a radial inwards oriented boundary layer (which starts at the rim of the impeller, **Figure 1**, point C) will be present on the impeller and will be directed towards the organic outlet of the extractor (**Figure 1**, point E). The lighter heptane phase is selectively entrained in this boundary layer. The through flow in this boundary layer thus increases with an increase of the rotational impeller speed.

The combined effect of the flow in this boundary layer and the centrifugal force that acts on the density difference between the liquids enhances the transportation of the light phase from the rim of the impeller (**Figure 1**, point C) to the liquid-liquid interface (**Figure 1**, point E). Therefore, the separation efficiency at the organic outlet is higher when the rotational speed of the impeller is increased. The separation efficiency at the aqueous outlet (**Figure 1,** point L) is lower when compared to that of the organic outlet (**Figure 1**, point F) because heptane droplets are entrained in the water flow. This means that coalescence of the heptane droplets at the liquid-liquid interface (**Figure 1**, point D) is stronger than the separation between the rotating enclosure and the weir (**Figure 1,** point J). Increasing the weir height would thus improve the separation efficiency at the aqueous outlet.

6.3.2. Mass transfer experiments

Mass transfer experiments have shown that equilibrium can be reached in one contacting stage, i.e., in one set of subsequent mixing and separation. The benzoic acid concentration in heptane decreases over time and the benzoic concentration in water increases. Comparing the measured outlet concentrations with published equilibrium data shows that the benzoic acid concentrations are in equilibrium (Visscher et al., 2011) when the impeller is rotated at 300 RPM and the enclosure is rotated at 200 RPM.

This proves that the shear stress present at a difference in rotational speed of 100 RPM generates sufficient mass transfer to reach equilibrium. From the initial concentrations, the outgoing concentrations and the flow rates, it was concluded that the mass balance is accurate within more than 99%.

It is assumed that both heptane and water behave as mixed phases. This implies that equilibrium is reached during the mixing phase in one rotor-impeller-rotor sequence, and thus that this sequence equals one contacting stage. If either heptane or water would behave as a plug flow-volume while flowing from the rim of the impeller (**Figure 1**, point C), the counter-current flow in the extractor implies that multiple contacting stages could be reached in one rotor-impeller-rotor sequence. The assumption of mixed behavior thus yields a minimum value of the number of transfer units.

The extractor presented in this chapter has a length of 77 10^{-3} m and contains one rotor-impeller-rotor stage. This equals 13 transfer units per meter (H.T.U. = 0.077 m). Adding an additional contacting stage increases the extractor length with 14 10^{-3} m. The height of transfer unit (H.T.U) thus equals 14 10^{-3} m when the number of stages is increased, assuming one meter of extractor length yields than 70 stages.

6.3.3. Extractor comparison

Comparing liquid-liquid extraction equipment is a complex task. Essential parameters are the capacity (in m^3 per day), extractor efficiency (in transfer units per meter), extractor volume (in m^3), and power requirements of the extractor and the pumps (in kW). One way to compare centrifugal extractors is shown in the Stichlmair plot shown in **Figure 5**. The x-axis shows the capacity, which is defined as cubic meter liquid per square meter area per hour (Stichlmair, 1980, Frank et al., 2012). The initial publication did not include centrifugal extractors. This so-called Stichlmair plot is updated here with centrifugal extractors in **Figure 6** and **Table 2.**

In the original publication, the cross sectional area of the equipment is taken as the area perpendicular to the flow direction. Stacking multiple contacting stages on one rotating shaft yields an equal geometry for centrifugal extractors as for conventional extractor columns. The cross sectional area of the centrifugal extractors is calculated from the inner diameter of the rotating element (**Table 2)**. The height of a transfer unit of the rotor-rotor spinning disc extractor is ten times lower compared to other centrifugal extractors like the Podbielniak and the Rousselet-Robatel extractor. This implies that the equipment volume can be reduced by a factor 10.

Table 2. Design data of various centrifugal extractors. Total volumetric flow rate, F_V, extractor diameter, D, extractor height, H, extractor area, A, motor power, P, number of transfer units in one extractor, N.T.U., height of a transfer unit, H.T.U., number of transfer units per length, and the extractor capacity, C.

	F_V / $m^3\ hr^{-1}$	D / m	H / m	A / m^2	W / kg	P / kW	N.T.U	H.T.U	Stages /m	C / m/s
Podbielniak										
A1	0.03	0.30	0.30	0.07	68	1.87	7.7	0.04	25.67	0.4
B10	6.81	1.38	0.83	1.48	1226	5.00	6.5	0.13	7.88	4.6
D18	11.10	1.90	1.13	2.84	3904	7.46	5.5	0.20	4.89	3.9
E48	113.5	2.83	1.48	6.27	9761	16.41	4	0.37	2.71	18.1
CINC										
CS50	0.11	0.23	0.54	0.05	11	0.18	1	0.54	1.87	2.2
CS125	1.36	0.31	0.91	0.09	68	1.50	1	0.91	1.09	14.6
CS250	6.81	0.70	1.52	0.49	340	6.50	1	1.52	0.66	13.9
CS400	20.44	0.91	1.96	0.84	1361	11.00	1	1.96	0.51	24.5
CS500	45.42	1.22	2.57	1.49	2041	30.00	1	2.57	0.39	30.5
Rousselet-Robatel										
LX122	0.03	0.12	1.13	0.01	180	0.75	2	0.57	1.77	2.7
LX123	0.03	0.12	1.17	0.01	185	0.75	3	0.39	2.56	2.7
LX124	0.03	0.12	1.20	0.01	190	0.75	3	0.40	2.50	2.7
LX126	0.03	0.12	1.28	0.01	210	0.75	6	0.21	4.69	2.7
LX202	0.30	0.20	1.25	0.03	220	1.50	2	0.63	1.60	9.6
LX204	0.30	0.20	1.33	0.03	240	1.50	4	0.33	3.01	9.6
LX323	1.80	0.32	0.76	0.08	280	5.50	3	0.25	3.95	22.4
LX325	1.30	0.32	0.76	0.08	300	5.50	5	0.15	6.58	16.2
LX363	2.10	0.36	0.76	0.10	300	7.50	3	0.25	3.95	20.6
LX365	1.50	0.36	0.76	0.10	320	7.50	5	0.15	6.58	14.7
LX524	6.00	0.52	1.10	0.21	1020	18.5	4	0.28	3.64	28.6
LX527	3.50	0.52	1.10	0.21	1080	18.5	7	0.16	6.36	16.7
LX574	8.00	0.57	1.10	0.26	1100	18.5	4	0.28	3.64	31.4
LX576	6.00	0.57	1.10	0.26	1160	18.5	6	0.18	5.45	23.5
This work										
1-stage	0.02	0.18	0.08	0.03	25	3	1	0.08	12.99	0.7
3-stage	0.22	0.18	0.11	0.03	48	3	3	0.01	71.43	8.5

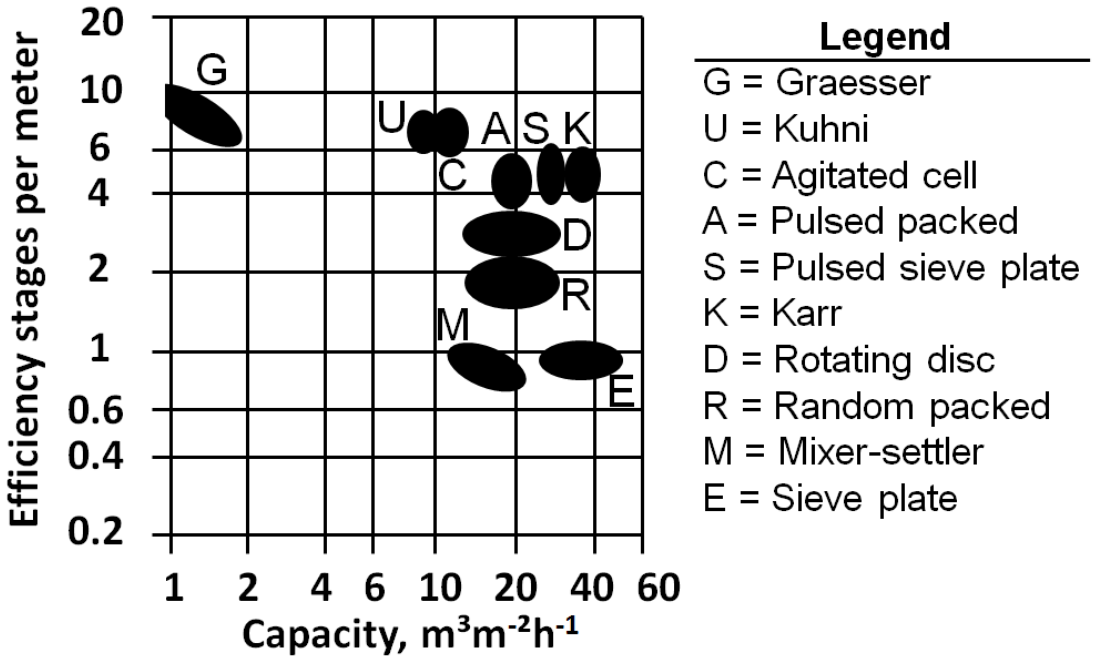

Figure 5. Original Stichlmair plot which shows number of efficiency stages per meter versus the capacity (Frank et al., 2012).

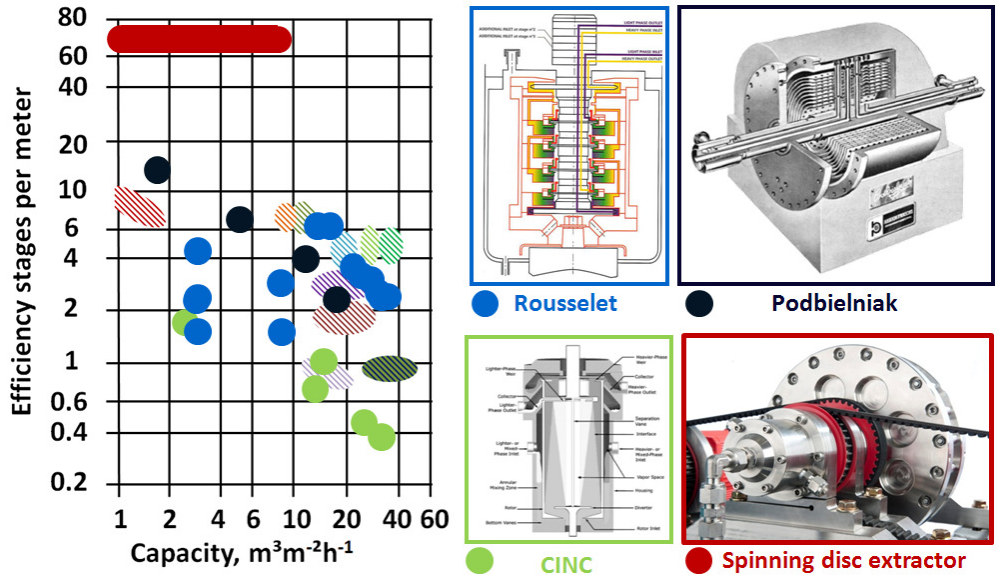

Figure 6. Reactor comparison in a Stichlmair plot (Stichlmair, 1980). Centrifugal extractors are indicated by the blue, red and green circles, non-centrifugal extractors are indicated by the shaded ellipse figures in the diagram. The spinning disc extractor (red) presented in this study has a factor 10 more contacting stages per meter when compared to extractors from Podbielniak (black), CINC (green), or Rousselet-Robatel (blue).

The local energy dissipation in the liquid-liquid mixture is not known for the various centrifugal extractors. However, the maximum power consumption of the motor that propels the rotating reactor parts is available in public literature supplied by the equipment manufacturers (**Table 2)**. The maximum power consumption of the motor is on the same order of magnitude as for other centrifugal extractors (**Figure 7** and **Table 2)**.

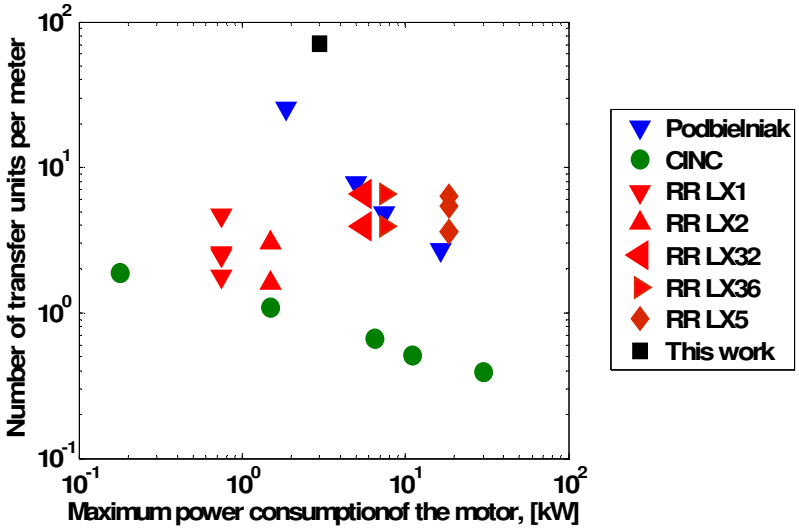

Figure 7. The number of transfer units per meter versus the maximum power consumption of the motor that drives the centrifugal extractor (in kW). The spinning disc extractor contains more transfer units per stage, at a power consumption that is of the same order of magnitude as for other centrifugal extractors. Data is taken from Table 2.

A last advantageous and unique aspect of the extractor is the ability of tuning mixing and separation efficiency individually. The mixing intensity, represented by the mass transfer rate, is determined by the net shear stress between the impeller and the enclosure. The separation efficiency can be enhanced by increasing the intensity of centrifugal force, which is determined by the rotational speed of the enclosure. For a given rotation speed of the enclosure the rotation speed of the impeller determines the difference in rotation speed and thus the mixing intensity.

6.4. Conclusions

A single-stage counter-current extractor is presented, which is based on rotor-rotor spinning disc technology. Counter-current contacting and consecutive complete separation of 5 m^3 total liquid per day is successfully achieved at rotational speeds below 450 RPM. The single-stage extractor can be extended in order to obtain multi-stage counter-current contacting with only 102 mL per stage. The height of a transfer unit is at least a factor 10 lower when compared to common centrifugal extractors. This spinning disc based extractor thus allows for significant intensification of separation processes, which is essential for applications in environments where equipment volume is limited, like on oil rigs and in space.

Nomenclature

Roman symbols

A	Column area perpendicular to flow direction, m^2
C	Concentration, mol m^{-3}
D	Diameter, m
F_V	Volumetric flow rate, m^3 s^{-1}
H	Height, M
k_La_L	liquid-liquid mass transfer rate, s^{-1}
N	Rotation speed, RPM
P	Maximum power consumed by the motor, kW
S	Solubility, mol%
t	Time, s
V	Volume, m^3
W	Weight, kg

Greek letters

ε_{ORG}	Organic phase volume fraction, m^3_{ORG} m^{-3}_R

Sub and superscripts

AQ	Aqueous phase
HA	Non-dissociated acid
MON	Monomer
ORG	Organic phase
R	Reactor
SS	Steady state
TOT	Total
0	Initial value

7. Liquid-liquid extraction in a three stage high-gravity extractor

This chapter has been submitted for publication:

F. Visscher, M.H.J.M. de Croon, J. van der Schaaf, J.C. Schouten. **"Liquid-liquid separation in a three-stage high-gravity extractor",** *Separation & Purification Technology*, 2013.

Abstract

This chapter presents a novel counter-current operated three-stage spinning disc extractor in which benzoic acid is extracted from *n*-heptane to water. Each contacting stage of the extractor consists of a rotor-impeller-rotor sequence. The mixing intensity and the separation efficiency in the extractor can be chosen independently by the separate adjustment of the rotational speeds of the impellers and the enclosure. The volume of one contacting stage is 102 10^{-6} m^3. This stage volume is a factor 10 smaller than for other centrifugal extractors. Each additional contacting stage extends the extractor length with 1.4 10^{-2} m. The first prototype of the extractor processes a total volumetric flow of 0.86 m^3 day^{-1}. The separation efficiencies at the extractor outlets and the degree of back mixing between consecutive contacting stages are reported. The separation efficiency can be tuned to >99.9% for rotational speeds below 1500 RPM. Mass transfer experiments have shown that the solute concentrations between *n*-heptane and water reach equilibrium at each contacting stage.

7.1. Introduction

Liquid-liquid extraction is a purification technique based on the distribution of a solute between two liquid phases (Muller et al., 5008). It is widely applied in chemical industry, e.g. to separate aromatics from aliphatic hydrocarbons, to produce temperature sensitive vitamins, and to manufacture nylon-6. Liquid-liquid extraction can be performed in co-current and counter-current mode. In co-current multistage extraction the solute concentration in both liquid phases reaches equilibrium. Adding more contacting stages does not result in a further solute transfer between the two liquid phases. In counter-current operation there is cross-over of the solute between two liquids that are flowing in opposite directions. Thus one contacting stage requires consecutive mixing and separation of the two liquids. Increasing the number of contacting stages allows to transfer the solute between the phases almost completely. This is shown in **Figure 1**.

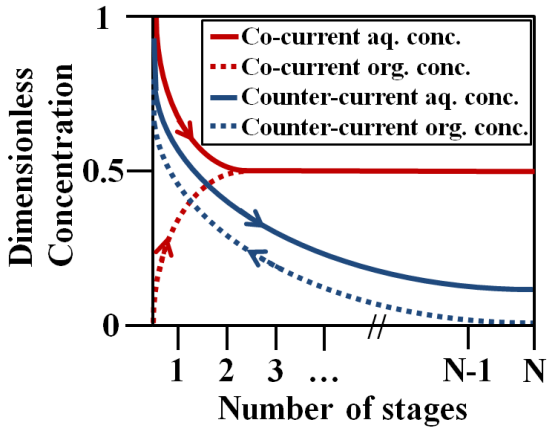

Figure 1. Concentration profiles for counter-current (blue) and co-current (red) extraction. A solute is transferred from an initially solute rich aqueous phase (solid line) towards an initially solute-free organic phase (dotted line). In the co-current scheme the solute distribution reach equilibrium. In counter-current flow the solute is transferred almost completely between the phases.

Incomplete separation between contacting stages decreases the net amount of transferred solute (Ingham et al., 2007). The ability of an extractor to separate liquids, further denoted as the separation efficiency, is therefore an essential characteristic of liquid-liquid extraction equipment. Counter-current liquid-liquid extraction is often operated in gravity driven, continuously operated counter-current extractors (Míšek, 1994). Examples are the Kuhni column (Gomes et al., 2009), the packed column (Varteressian et al., 2002), and the rotating disc contactor (Al-Rahawi, 2007, Trambouze et al., 2002). In such extractors liquids are separated due to the effect of gravity on the density difference between the liquids. The length of an extraction column increases when the density difference becomes smaller. Liquid-liquid extraction columns can have volumes up to 700 m^3 (Trambouze et al., 2002). Accordingly the liquids have relatively long residence times in the range of hours.

Centrifugal extractors were developed to reduce the equipment volume with at least a factor 100, reduce the processing time accordingly and to enhance the separation efficiency (Gebauer et al., 1982). Examples of such extractors are the Podbielniak extractor (Barson et al., 1953, Podbielniak et al., 1959), the annular centrifugal extractor (Deshmukh et al., 2007), and the Westfalia/Luwesta extractor (Likidis et al., 1989). In order to obtain multiple contacting stages in centrifugal extractors every additional contacting step requires an entire new module, which implies a considerable increase of floor space requirements.

A low-volume single-stage counter-current extractor which is based on rotor-impeller-rotor spinning disc technology has been repeated earlier (van der Schaaf et al., 2012, Visscher et al., 2013, Visscher et al., 2012d). This single-stage extractor allows for the subsequent contacting and separation of two immiscible liquids, in this study represented by *n*-heptane and water.

A schematic side view of the single-stage extractor is shown in the previous chapter. The single-stage extractor consists of one rotor-impeller-rotor sequence. Two weirs are rotating along with the enclosure. Liquids present in the volume between the enclosure and the weirs are susceptible for the centrifugal force. Droplets of the phase with the lower density (*n*-heptane, yellow) flow therefore radially inwards. The impeller pumps the liquid with the lower density from left to right and operates similar to the impellers used in centrifugal pumps (Coulson et al., 2007, Visscher et al., 2012a). Simultaneously the liquid with the higher density (water, blue) is fed from right to left. Both liquids are in intimate contact at the impeller outlet, where the liquid with the lower density is dispersed into the liquid with the higher density.

In this chapter, the single-stage extractor is extended with two additional contacting stages to demonstrate extractor scale-up. This chapter describes the separation efficiency of a counter-current operated three-stage extractor with a volume of 102 10^{-6} m^3 per stage. The separation efficiency is determined by the separation of two immiscible liquids, represented by *n*-heptane and water. Additionally, for a separation efficiency above 99.9%, the number of contacting stages is determined by extraction of benzoic acid from *n*-heptane to water. The operating principle of the three-stage extractor is shown in **Figure 2**.

The small extractor volume allows for a rapid change in product stream which reduces the down-time of the extractor. Additionally, the small extractor internal surface opens up the application of exceptional coatings of the extractor parts like platinum and tantalum. These expensive construction materials are often essential to prevent corrosion of the extraction equipment.

7.2. Experimental section

The diameter of the three-stage extractor is equal to the diameter of the single-stage extractor (Visscher et al., 2013). The impellers and the enclosure are co-rotating. The impellers consist of a top disc with a diameter of 146 10^{-3} m and a bottom disc with a diameter of 170 10^{-3} m. The top and bottom discs are connected by six vanes with a height of 2 10^{-3} m. The inner diameter of the extractor is equal to 180 10^{-3} m; the outer diameter of the single-stage extractor equals 242 10^{-3} m. The weirs have a thickness of 1 10^{-3} m (points C1, C2 C3 and D1, D2, D3, **Figure 2**), and are mounted adjacent to the enclosure (Dark grey in **Figure 2)**. These weirs are concentric rings. The inner diameter of the concentric rings at the inlet side of the impellers (Points C1, C2, C3, **Figure 2**) is 30 10^{-3} m. An illustration of the fluid flow directions and the mechanical construction is given in the **Figures 3-8.**

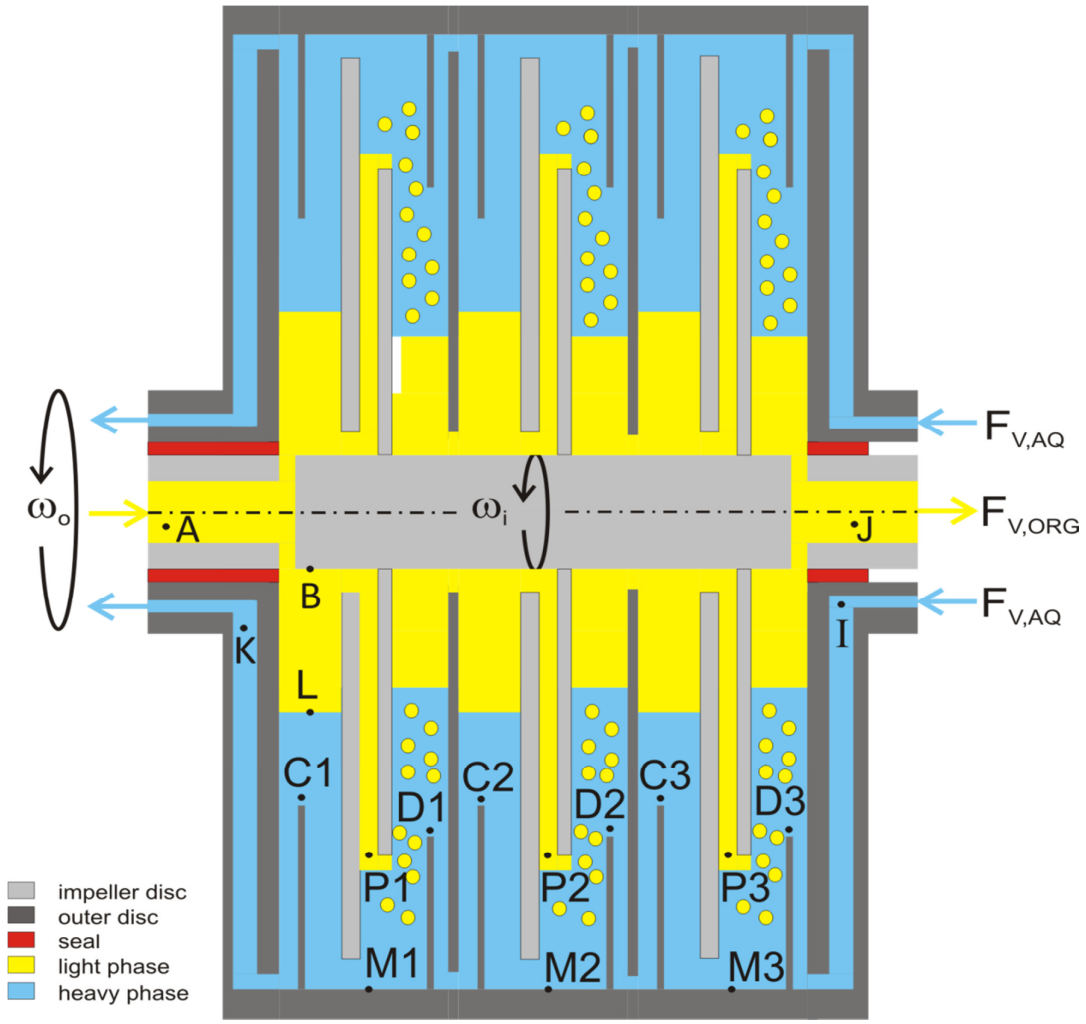

Figure 2. A schematic view of the three-stage spinning disc based extractor. Increasing the extractor with two contacting stages increases the length of the extractor with 2.8 10^{-2} m. The height equivalent of a theoretical stage thus equals 1.4 10^{-2} m. Each additional contacting stage equals 102 10^{-6} m^3 of extractor volume.

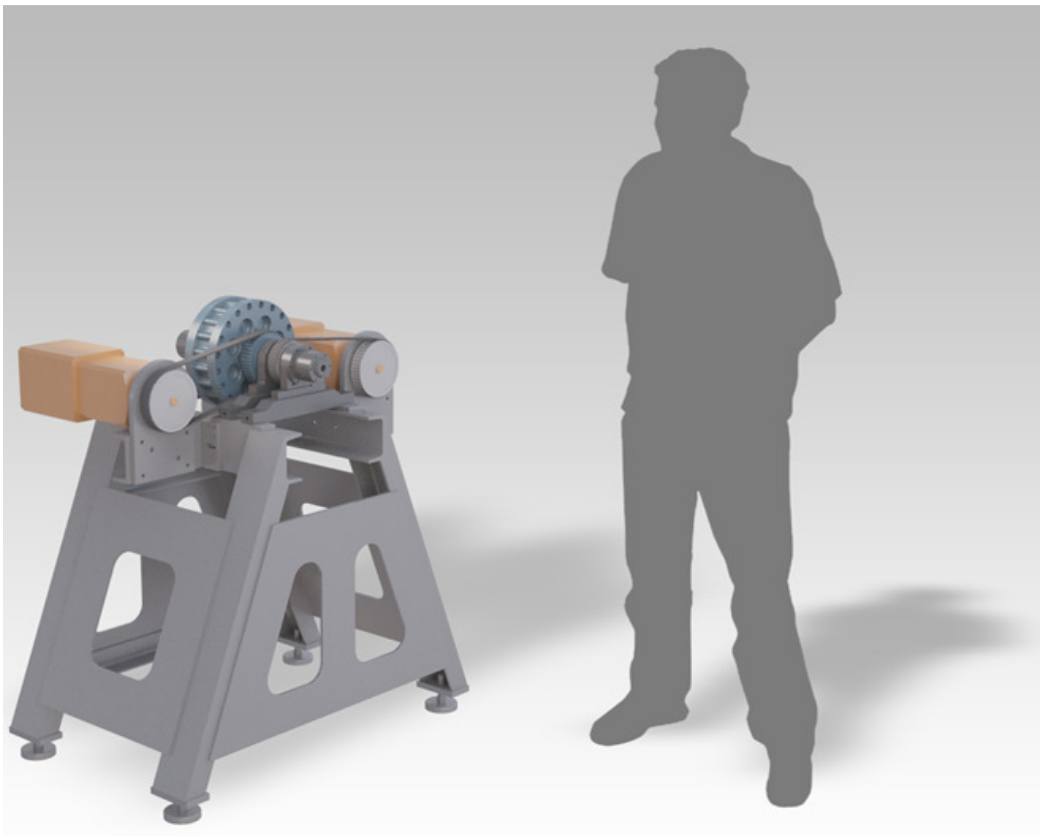

Figure 3. The low-volume three-stage extractor is mounted on a stand-alone frame. The extractor fits on a normal pallet and requires little floor-space, as can be seen in the comparsion to a human being

.

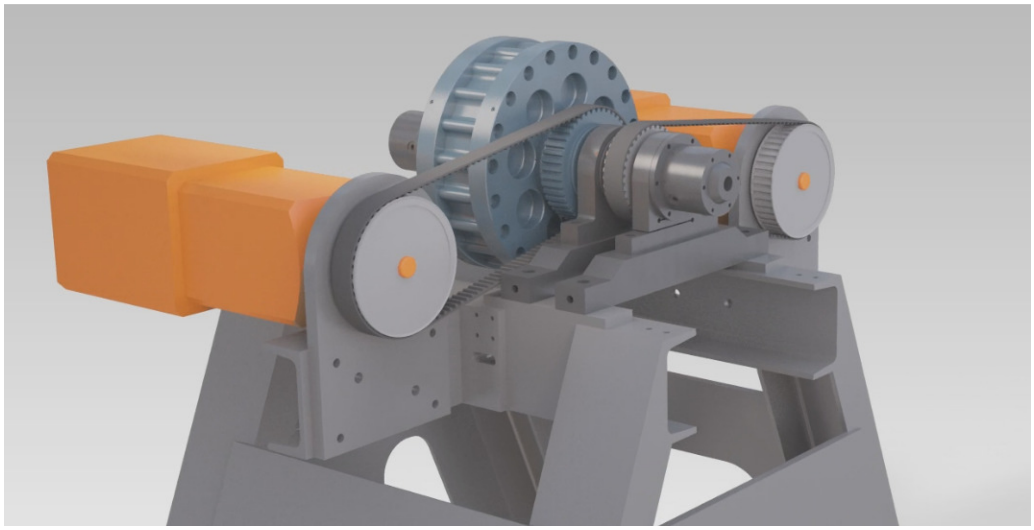

Figure 4. The extractor consists of two co-rotating rotating elements: the enclosure (in blue) and the impellers (not visible).

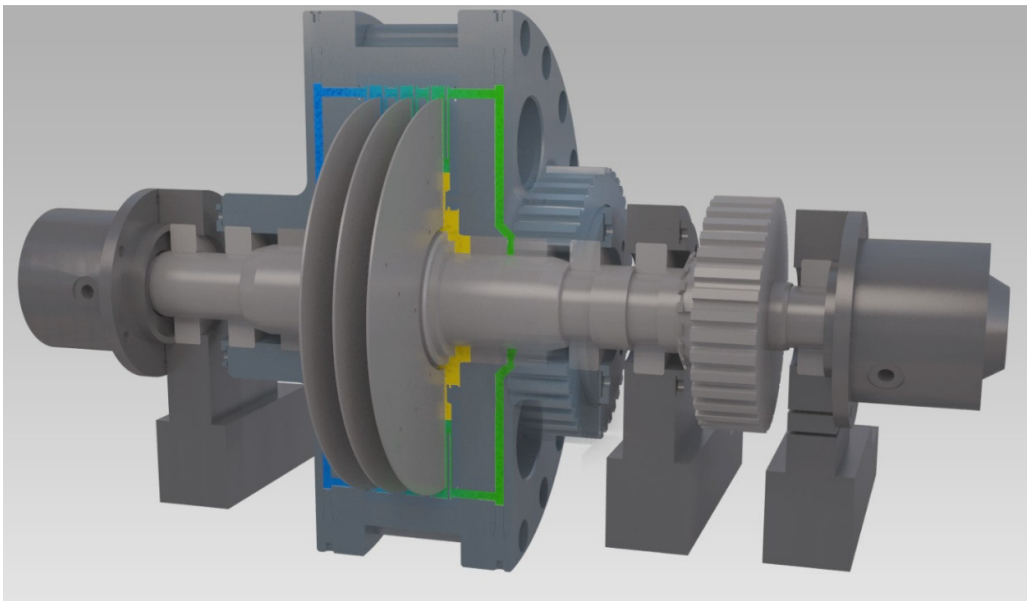

Figure 5. Side view of the three-stage prototype. Three impellers-in-series are placed on a single rotatable shaft, inside the enclosure. Weirs are present between the impellers and separate the consecutive stages.

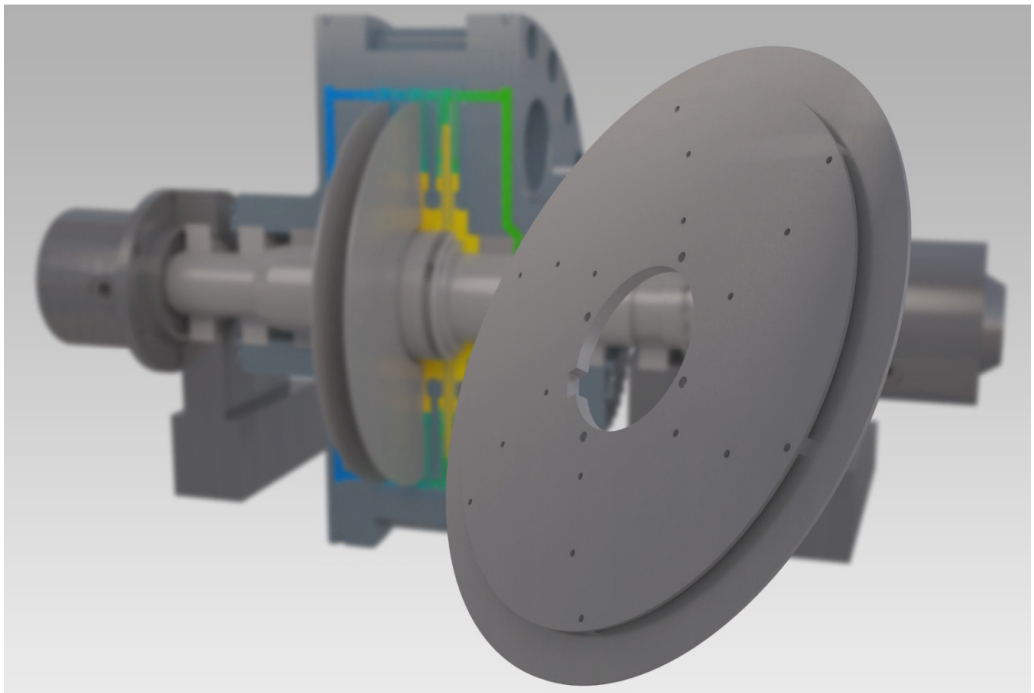

Figure 6. The impeller consist of a top disc with a diameter of 146 10^{-3} m and a bottom disc with a diameter of 170 10^{-3} m. The top and bottom discs are connected by six vanes with a height of 2 10^{-3} m. Three impellers are mounted on a single rotatable shaft, and are separated by weirs which are co-rotating with the enclosure.

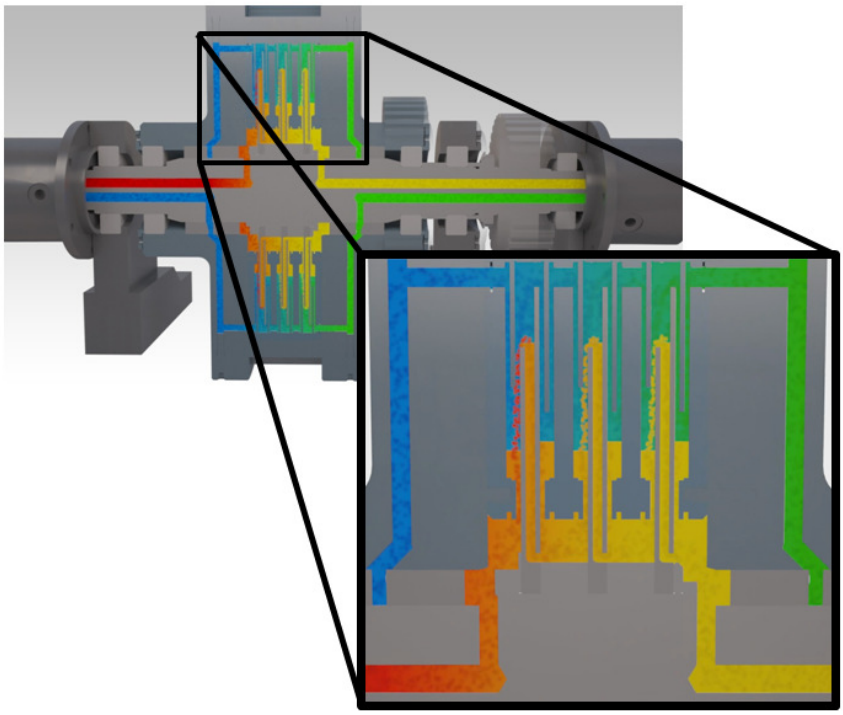

Figure 7. Operating principle of the three-stage extractor. The liquid with the lower density flows from right to left (shown as the transition of yellow to red). The liquid with the higher density flows from left to right (shown as the transition of blue to green). In this way a repeating step of intense mixing and complete separation is achieved three times.

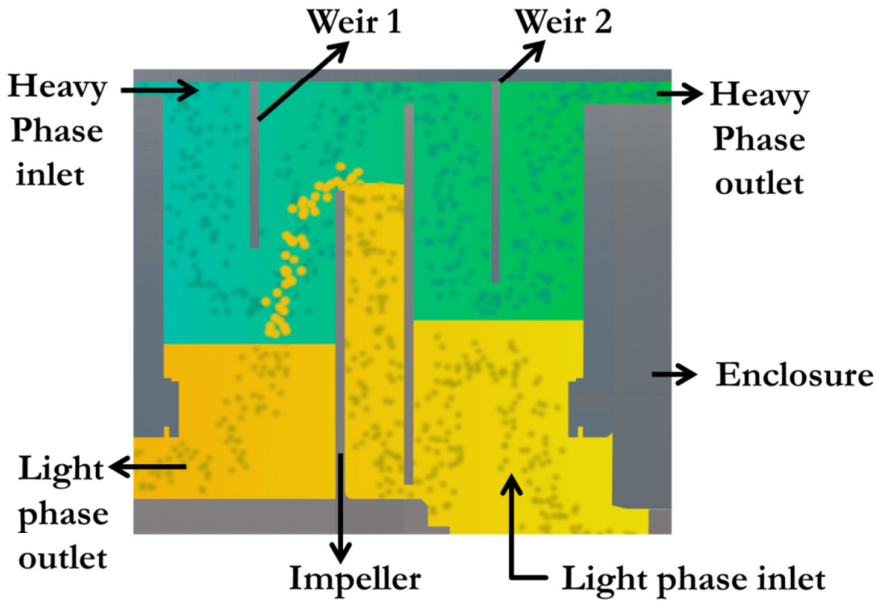

Figure 8. Close-up of Figure 7 showing a single contacting stage. The fluid flow directions are shown, together with the names of the mechanical elements.

The inner diameter of the concentric rings at the outlet side of the impellers (Points D1, D2, D3, **Figure 2**) is 25 10^{-3} m. The spacing between the impeller and the weirs, as well as the spacing between the weirs and the enclosure equals 1 10^{-3} m. The distance between the impeller and the enclosure is thus limited to 3 10^{-3} m. The total extractor volume equals 192 10^{-6} m^3 (**Figure 1**). The extractor volume where mass transfer occurs equals 139 10^{-6} m^3 (**Figure 1**). A photograph of the side view of the three-stage extractor is given in **Figure 9**.

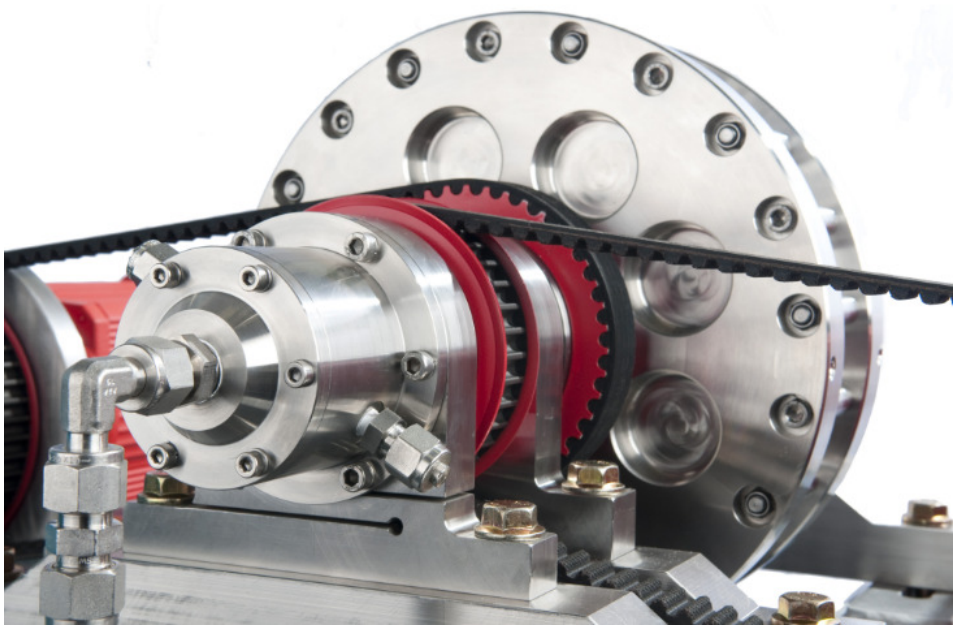

Figure 9. Side view of the realized prototype. Both the rotating shaft of the impellers and the rotating shaft of the enclosure are connected through a belt to the pulley that is attached to the motors.

The impeller and enclosure are propelled by a timing belt which is connected to a 3kW motor (SCFM71M, SEW). The maximum rotation speed of both the impeller and the enclosure is limited to 1500 RPM. The volumetric flow rates of *n*-heptane and water are controlled by two Coriolis mass flow controllers (M55, Bronkhorst). The maximum volumetric flow rate of the combined phases is 60 10^{-6} m^3 s^{-1}. All equipment is connected through ⅜" Swagelok tubing. Pressure and temperature are measured inline at the reactor inlets (points A, I, **Figure 2**) and outlets (points J, K, **Figure 2**). All generated data points are collected in LabView.

7.2.1. Separation at the extractor outlets

n-Heptane and water were contacted in counter-current mode at an aqueous to organic flow ratio of 1:1 with a total volumetric flow rate of 0.86 m^3 mixture per day (10 10^{-6} m^3 s^{-1}). For each measurement of the separation efficiency the volumetric flow rates of water and *n*-heptane were set each to 5.0 10^{-6} m^3 s^{-1} (0.43 m^3 day^{-1}). Next the rotation speeds of the impeller and the enclosure were set.

After reaching the desired rotation speed, thirty seconds were awaited to ensure steady state hydrodynamic behavior. Once this steady state was achieved, a constant separation efficiency was measured over time at the aqueous outlet (point K, **Figure 2**) and the organic outlet (point J, **Figure 2**). The total outflow was collected for 60 seconds at both outlets in two 500 10^{-6} m^3 calibrated graduated cylinders. Each measurement was performed at least twice. The separation efficiency is defined as the ratio of the volume of the desired liquid over the total collected volume (eqs. (1) and (2)). The separation efficiency was measured as a function of the rotation speeds of the impeller and the enclosure.

$$\mathrm{Aq}: \frac{V_{AQ}}{V_{AQ} + V_{ORG}} \cdot 100\% \quad (1)$$

$$\mathrm{ORG}: \frac{V_{ORG}}{V_{AQ} + V_{ORG}} \cdot 100\% \quad (2)$$

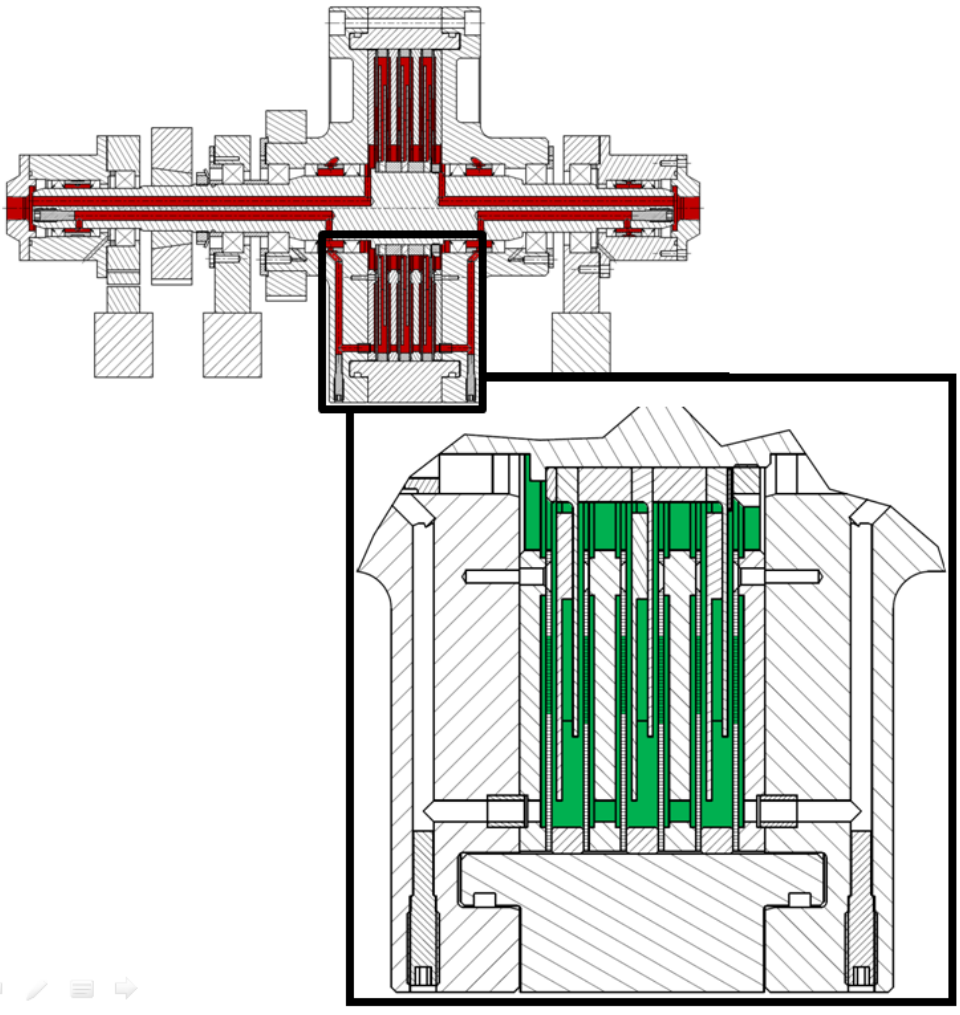

Figure 10. Schematic side view of the extractor. The total extractor volume available for fluid is shown in red. The volume where the liquids are contacted in case of complete separation at both outlets is shown in green in the close-up.

7.2.2. Separation between the stages

Back mixing of water and *n*-heptane between consecutive stages was qualitatively measured by performing mass transfer experiments in which benzoic acid was extracted from *n*-heptane to water.

The amount of benzoic acid that is transferred from *n*-heptane to water is determined by the number of contacting stages and the liquid-liquid mass transfer rate, k_La_L. For a given rotor-diameter and rotor-rotor distance, this is thus determined by the difference in rotation speeds of the impeller and the enclosure (Visscher et al., 2012d). The outlet concentrations of one contacting stage reach equilibrium at high liquid-liquid mass transfer rates.

At the start of an experiment the volumetric flow rate of *n*-heptane with benzoic acid and the volumetric flow rate of water were set to $5.0\ 10^{-6}$ m^3 s^{-1}. Samples of $5\ 10^{-6}$ m^3 were collected at both outlets with 50 s interval. All mass transfer measurements were performed at a separation efficiency of 100% at both outlets. The benzoic acid concentrations in both phases were measured for 500 seconds at various combinations of the rotation speeds of the impeller and the enclosure (Visscher et al., 2012d).

7.3. Results and discussion

7.3.1. Extractor outlet flow

The total liquid volume that is collected over 60 seconds at each outlet (Points J and K, **Figure 2**) is shown in **Figure 11** as a function of the rotation speed of the impeller and the rotation speed of the enclosure. For all measurements the volumetric flow rates of both *n*-heptane and water equal $5.0\ 10^{-6}$ m^3 s^{-1}.

Two observations are made. First, when the impellers are rotating faster that the enclosure the total liquid outflow at the organic outlet (point J, **Figure 2**) is increased and the total liquid outflow at the aqueous outlet (point K, **Figure 2**) is decreased. Second, when the enclosure is rotating faster than the impellers, the opposite trend is observed: the flow rate at the aqueous outlet (point K, **Figure 2**) is increased and the flow rate at the organic outlet (point J, **Figure 2**) is decreased.

When the impeller is rotating faster than the enclosure (ΔN=+450 RPM), the pumping action of the impellers-in-series causes all fluid to flow from the impeller inlet to the impeller outlets (Points P1, P2 P3, **Figure 2**).

When the pumping action of the impellers-in-series is larger than the combined flow of water and *n*-heptane fed to the extractor, liquid will be drawn in at the aqueous outlet (point K, **Figure 2**). This behavior has been observed earlier in case of an impeller-stator configuration (Hafez, 1991). When the enclosure is rotating faster than the impeller (ΔN=-600 RPM), the centrifugal force causes all liquid to flow out of the extractor at the aqueous outlet (point K**, Figure 2**).

When the through flow due to the centrifugal force is larger than the combined flow of water and *n*-heptane fed to the extractor, liquids will be sucked in at the organic outlet (point J, **Figure 2**). For complete separation of *n*-heptane and water a combination of rotation speeds is needed in which the centrifugal force due to the rotation of the enclosure balances the pumping action of the impellers-in-series.

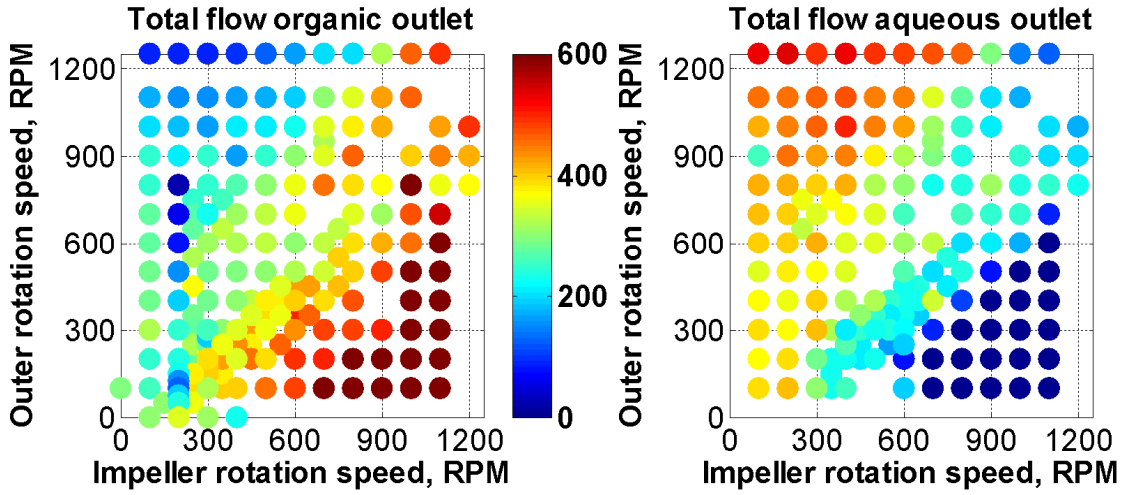

Figure 11 . The total outflow of the three-stage extractor is shown for both outlets, as a function of the rotation speeds of the impeller and the enclosure. Each measurement of the total outflow is measured for 60 seconds with equal flow rates of the aqueous and the organic phase of 5.0 10^{-6} m^3 s^{-1}. The total outflow is scaled from 0 (blue) to 600 ml (red).

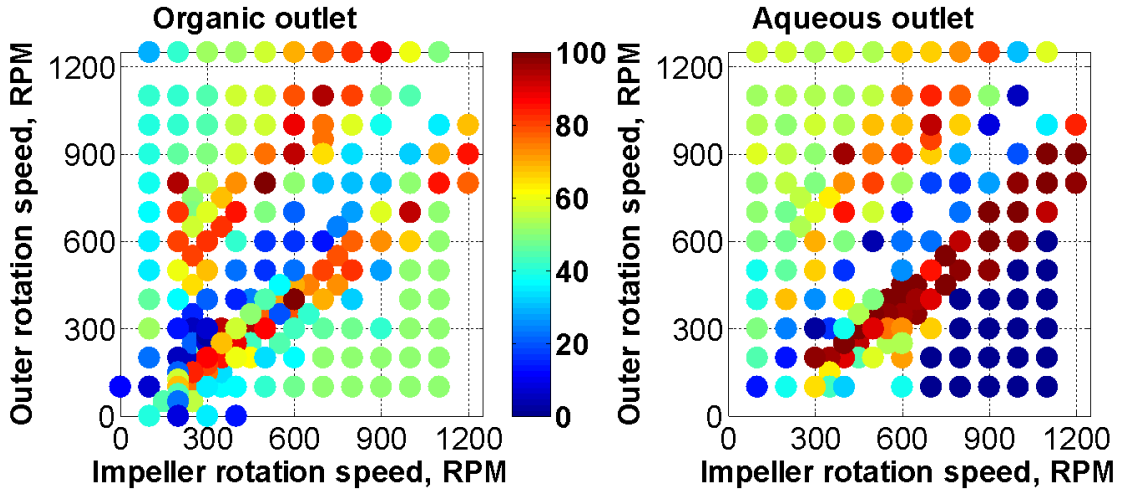

Figure 12. The separation efficiency of the three-stage extractor is shown as a function of the rotation speeds of the impeller and the enclosure. The highest separation efficiency is achieved when the rotation speed of the enclosure is close to that of the impeller. Separations are measured at equal flow rates of the aqueous and the organic phase of 5.0 10^{-6} m^3 s^{-1}. The separation efficiency is scaled from 0% (blue) to 100% (red).

7.3.2. Separation efficiency

The separation efficiency at both outlets is shown in **Figure 12** as a function of the rotation speeds of the impeller and the enclosure. The separation efficiency at both outlets (Points J and K, **Figure 2**) exceeds 99% for various combinations of rotation speeds. For example, a separation efficiency >99% is obtained at N_{IMP} = 450 RPM and N_{OUT} = 300 RPM ($\Delta N = +150$), and at N_{IMP} = 900 RPM and N_{OUT}= 1400 RPM ($\Delta N = -500$) (not shown).

The results show that complete separation of both liquid phases can be achieved at different mixing intensities. Mixing and separation are thus tuned independently of each other. This is a major benefit of the spinning disc based extractor over other centrifugal extractors like the Podbielniak, Rousselet-Robatel or Annular Centrifugal Extractors (CINC). In such centrifugal extractors, increasing the mixing intensity reduces the dispersed phase droplet diameter. As a result it becomes more difficult to separate the dispersed phase and the continuous phase.

The separation efficiency at both outlets (Points J and K, **Figure 2**) is below 20% when the rotation speed of the impeller is close to the rotation speed of the enclosure ($\Delta N < \pm 125$ RPM). The centrifugal force that acts on the liquid inside the impeller is equal or close to the centrifugal force that acts on the liquid between the impeller (light grey, **Figure 2**) and the enclosure (dark grey, **Figure 2**). Accordingly, there is no preferential flow of *n*-heptane through the impellers to point P, **Figure 2** The liquid present inside the impeller volume acts as a stagnant rotating liquid. In this case, *n*-heptane shortcuts the extractor from the organic inlet (Point B, **Figure 2**) to the aqueous outlet (Point K, **Figure 2**). Simultaneously, water shortcuts the extractor from the aqueous inlet (Point I, **Figure 2**) to the organic outlet (Points J, **Figure 2**). The separation efficiency of the extractor decreases below 20% at both outlets: an almost complete separation occurs without counter-current contacting of water and *n*-heptane.

Thus three regions are observed in **Figure 12** where the separation efficiencies at both outlets (points J and K, **Figure 2**) are low. Region 1 occurs when the impeller is rotating faster than the enclosure ($\Delta N \geq +450$ RPM). Region 2 occurs when the impeller is rotating slower than the enclosure ($\Delta N \leq -600$ RPM). Region 3 occurs when the rotation speed of the impeller and the enclosure are close ($\Delta N < \pm 125$ RPM).

A separation efficiency larger than 80% is achieved in the intermediate regions as can be seen in **Figure 12**. When the impellers are rotating faster than the enclosure ($\Delta N \geq$ 200 RPM), the pumping action of the impeller-in-series is forcing the *n*-heptane to flow through the subsequent impellers.

When the impellers are rotating 200 RPM slower than the enclosure, the impeller acts as a siphon that connects the liquid reservoir at the inlet side of the impeller (Point L, **Figure 2**) to the liquid reservoir at the outlet side of the impeller (Point P1, **Figure 2**). The siphon allows the *n*-heptane to flow to the organic outlet (point J, **Figure 2**). The centrifugal force that acts on the liquids between the impeller and the enclosure due to the rotation of the enclosure and causes the separation of water and *n*-heptane between the impeller outlet (Point P3, **Figure 2**) and the organic outlet of the extractor (Point J, **Figure 2**).

7.3.3. Inter stage separation

The steady state concentrations of benzoic acid at the extractor outlets are calculated as a function of the liquid-liquid mass transfer rate. For this purpose the extractor is described as three contacting stages in series. On each contacting stage ideally mixed behavior of each phase is assumed (**Figure 13**). From these assumptions six ordinary differential equations (ODE's) arise (**Table 3**) which are solved simultaneously. In the ODE's (**Table 3**), the driving force for mass transfer between water and *n*-heptane is the concentration difference of the benzoic acid monomer in the organic phase and the non-dissociated benzoic acid in the aqueous phase (Visscher et al., 2011, Visscher et al., 2012d). Solving the six ODE's yields the steady state concentrations at the extractor outlet as a function of the flow rates and initial conditions.

The steady state outlet concentrations in both phases are calculated for an aqueous volumetric flow rate (F_V^{AQ}) of 5.0 10^{-6} m^3 s^{-1}, organic volumetric flow rate (F_V^{ORG}) of 10.0 10^{-6} m^3 s^{-1}. The initial concentration of the aqueous phase (C_{AQ}^0) is 0 mol m^{-3}, and the initial concentration of the organic phase (C_{ORG}^0) is 47.8 mol m^{-3}. The volume fraction of *n*-heptane in the extractor, ε_{ORG}, is calculated from the ratio of the volumetric *n*-heptane flow rate over the total volumetric flow rate (Visscher et al., 2012b). The liquid-liquid mass transfer rate is not limiting, as a result the benzoic acid concentrations in water and *n*-heptane are in equilibrium on each contacting stage.

The operating line of the extractor originates from the mole balance over the entire extractor, and is given by equation (3). The operating line gives the relationship between the initial concentrations, C^0 (Points A, I, **Figure 2**), and the steady state concentrations at the extractor outlets, C^{SS} (Points J, K, **Figure 2**). The operating line has the slope F_V^{ORG} / F_V^{AQ}, and passes through two coordinates P(C_{ORG}^{SS}, C_{AQ}^0) and Q(C_{ORG}^0, C_{AQ}^{SS}).

$$\frac{F_V^{ORG}}{F_V^{AQ}} = \frac{\left(C_{AQ}^{SS} - C_{AQ}^0\right)}{\left(C_{ORG}^0 - C_{ORG}^{SS}\right)} \tag{3}$$

The operating line is shown together with the equilibrium curve in **Figure 14**. The calculated exit concentrations of stage 1 (●), stage 2 (■), and stage 3 (♦) are marked on the equilibrium curve. The number of contacting stages can thus be estimated from the equilibrium curve and the operating line. This is marked by the dotted lines.

This procedure is similar to the McCabe-Thiele method which is used to analyze binary distillation (*21*). Dimerization of benzoic acid causes a strong non-linear curvature of the equilibrium curve (Long et al., 2008, Visscher et al., 2011). The operating line and the equilibrium curve therefor may have an intersection, and thus may yield a solutropic composition, similar to an azeotropic composition in distillation (Smith, 1950).

The steady state concentrations of benzoic acid at the extractor outlets (Points J and K, **Figure 2**) were determined experimentally for an aqueous volumetric flow rate of 5.0 10^{-6} m^3 s^{-1}, organic volumetric flow rate of 5.0 10^{-6} m^3 s^{-1}.The initial benzoic acid concentration in the aqueous phase was 0 mol m^{-3}, and the initial benzoic acid concentration in the organic phase of 28.7 mol m^{-3}. The rotation speed of the impeller was set to 900 RPM, the rotation speed of the enclosure to 1500 (ΔN=+500 RPM).

The total benzoic acid concentration in the organic phase decreases in 450 seconds from the initial concentration (28.7 mol m^{-3}) to the steady state concentration (13.2 mol m^{-3}). The total benzoic acid concentration in the aqueous phase increases from the initial concentration (0 mol m^{-3}) to the steady state concentration (15.4 mol m^{-3}).

These benzoic acid concentrations are close to the concentrations for calculations in which the liquid-liquid mass transfer is not limiting, and in which complete phase separation is assumed. For those conditions the steady state benzoic acid outlet concentrations in *n*-heptane and water equal 13.1 mol m^{-3} and 15.5 mol m^{-3} respectively.

These calculated steady state concentrations are close to the measured values, which proves the complete separation between the consecutive stages. Also this shows that equilibrium is reached at each stage at a rotation speed difference of +500 RPM

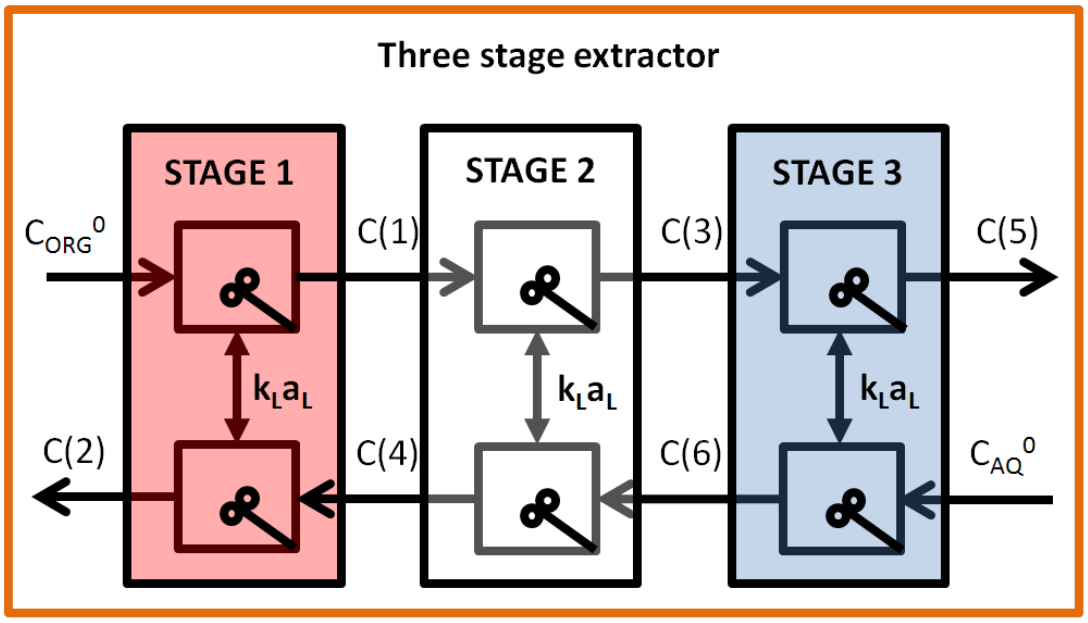

Figure 13. Model used to predict the steady state concentration of benzoic acid in both phases. Six linear ordinary differential equations are solved simultaneously as a function of the liquid-liquid mass transfer rate, k_La_L. The indices of the concentrations originate from the ODE-number.

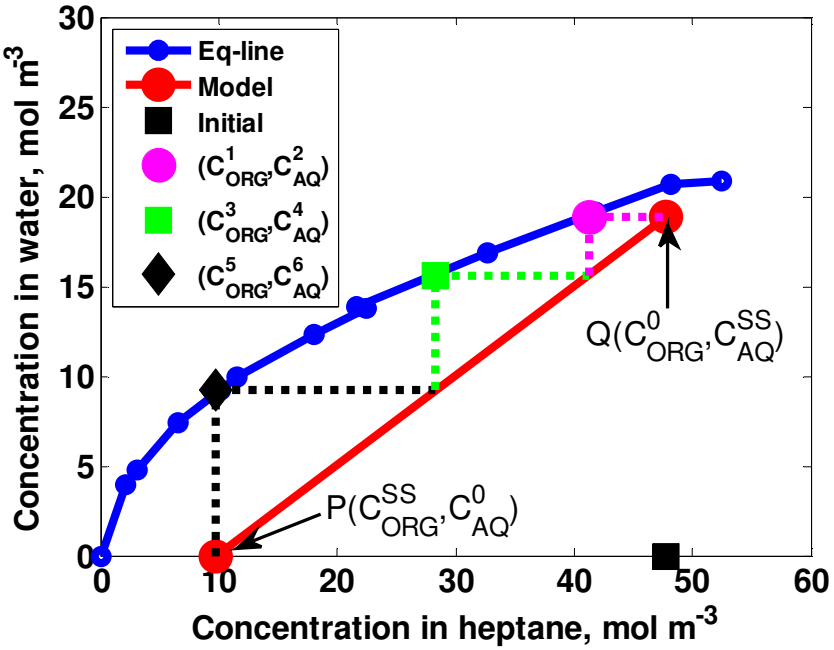

Figure 14. The equilibrium curve of the water/*n*-heptane/benzoic acid system is shown in blue (Visscher et al., 2011). The modeled operating line is shown in red, with the coordinates P and Q from equation (3). Model conditions: F_V^{AQ} = 5 10^{-6} m^3 s^{-1}, F_V^{ORG} = 10 10^{-6} m^3 s^{-1} C_{AQ}^0 = 0 mol m^{-3}, C_{ORG}^0 = 47.8 mol m^{-3}. The value of k_La_L is set to infinite, thus equilibrium is obtained on each contacting stage. The calculated exit concentrations of stage 1 (●), stage 2 (■), and stage 3 (♦) are shown on the equilibrium curve.

Table 3. Ordinary differential equations used to predict the steady state benzoic concentrations at the outlet of the extractor (Figure 13).

ODE	Stage	Liquid phase	Ordinary differential equation
1	1	ORG	$\frac{dC_{ORG}^{TOT,1}}{dt} = F_{V,ORG}\left(C_{ORG}^{0} - C_{ORG}^{TOT,1}\right)... - k_L a_L \varepsilon_{ORG} V_R \left(C_{ORG}^{MON,1} - K_P^{MON} C_{AQ}^{HA,1}\right)$
2	1	AQ	$\frac{dC_{AQ}^{TOT,1}}{dt} = F_{V,AQ}\left(C_{AQ}^{TOT,2} - C_{AQ}^{TOT,1}\right)... - k_L a_L \varepsilon_{ORG} V_R \left(C_{ORG}^{MON,1} - K_P^{MON} C_{AQ}^{HA,1}\right)$
3	2	ORG	$\frac{dC_{ORG}^{TOT,2}}{dt} = F_{V,ORG}\left(C_{ORG}^{TOT,1} - C_{ORG}^{TOT,2}\right)... - k_L a_L \varepsilon_{ORG} V_R \left(C_{ORG}^{MON,2} - K_P^{MON} C_{AQ}^{HA,2}\right)$
4	2	AQ	$\frac{dC_{AQ}^{TOT,2}}{dt} = F_{V,AQ}\left(C_{AQ}^{TOT,3} - C_{AQ}^{TOT,2}\right)... - k_L a_L \varepsilon_{ORG} V_R \left(C_{ORG}^{MON,2} - K_P^{MON} C_{AQ}^{HA,2}\right)$
5	3	ORG	$\frac{dC_{ORG}^{TOT,3}}{dt} = F_{V,ORG}\left(C_{ORG}^{TOT,2} - C_{ORG}^{TOT,3}\right)... - k_L a_L \varepsilon_{ORG} V_R \left(C_{ORG}^{MON,3} - K_P^{MON} C_{AQ}^{HA,3}\right)$
6	3	AQ	$\frac{dC_{AQ}^{TOT,3}}{dt} = F_{V,AQ}\left(C_{AQ}^{0} - C_{AQ}^{TOT,3}\right)... - k_L a_L \varepsilon_{ORG} V_R \left(C_{ORG}^{MON,3} - K_P^{MON} C_{AQ}^{HA,3}\right)$

7.4. Benchmarking

One way to compare extractor performance is by using the Stichlmair plot, which shows the number of transfer stages per meter versus the capacity (in cubic meter liquid per square meter area per hour). In the original plot the cross sectional area of extraction columns is taken as the area perpendicular to the flow direction (Stichlmair, 1980). Stacking multiple contacting stages on one rotating shaft yields an equal geometry for centrifugal extractors as for conventional extractor columns (Visscher et al., 2013). Each additional contacting stage adds 14 10^{-3} m to the length of the extractor, thus a spinning disc based extractor of 1 meter high may contain 71 contacting stages. This is 3 times more than the in case of Podbielniak extractor (Type A1, (Barson et al., 1953)), 30 times more than the annular centrifugal extractor from CINC (CS500, (CINC, 2013)), and 30 times more than the Rousselet-Robatel extractors (LX527, (Rousselet Robatel, 2013)), (Visscher et al., 2013).

7.5. Conclusion

A counter-current operated, three-stage spinning disc based centrifugal extractor is presented. Each contacting stage of the extractor consists of a rotor-impeller-rotor sequence. Each additional contacting stage extends the length of the extractor with 1.4 10^{-2} m. The volume of a contacting stage is 102 10^{-6} m^3. The extractor processes up to 0.86 m^3 day^{-1}. Complete separation can be achieved for both outlets for rational speeds below 1500 RPM. The mixing intensity in the extractor is tuned independently by adjusting the rotation speed difference between the impeller and the enclosure.

Nomenclature

Roman symbols

C	Concentration, mol m^{-3}
F_V	Volumetric flow rate, m^3 s^{-1}
k_La_L	liquid-liquid mass transfer rate, s^{-1}
N	Rotation speed, RPM
S	Solubility, mol%
t	Time, s
V	Volume, m^3

Greek letters

ε_{ORG}	Organic phase volume fraction, m^3_{ORG} m^{-3}_R
ϱ	Density, kg m^{-3}
η	Viscosity, kg m^{-1} s
σ	Surface tension, mN m^{-1}

Sub and superscripts

AQ	Aqueous phase
DIM	Dimer
IMP	Impeller
L	Liquid
MON	Monomer
ORG	Organic phase
OUT	Enclosure
R	Reactor
SS	Steady state
TOT	Total
0	Initial value

8. Conclusions and outlook

8.1. Conclusions

This thesis describes the results of a PhD-project leading to novel and compact rotating equipment in which two immiscible phases are intensely contacted, either co-current or counter-currently. This equipment is based on spinning disc technology and utilizes high-gravity, high-shear conditions, which yield high mass transfer rates for liquid-liquid mixtures. In this thesis, first the single phase fluid flow in a rotor-stator spinning disc reactor (SDR) is described. Next, a mixture of *n*-heptane and water is used to describe the volume fraction and the liquid-liquid mass transfer rates in an SDR. Following, the rotor is replaced with an impeller. The pumping action of the impeller is essential for the counter-current contacting of two immiscible liquids, as is shown in the last two chapters.

A reactor model is presented for the single phase fluid flow in a rotor-stator spinning disc reactor which is based on residence time distribution measurements. The residence time distribution was determined from pulse-wise tracer injection experiments, as a function of the rotational disc speed, the volumetric flow rate of water, and the axial clearance between the rotor and the stator. The residence time distribution is described by a plug flow model in combination with 2 to 3 ideally stirred tanks-in-series. The resulting reactor model is explained with the effect of turbulence, the formation of von Kármán and Bödewadt boundary layers, and the effect of the volumetric flow rate.

The single phase study is extended to a multiphase study in which *n*-heptane and water are contacted in an SDR. Their volume fractions were measured using γ-ray tomography and photographic image analysis and are determined as a function of rotational disc speed, flow ratio, position in the reactor, liquid mixture density difference, and rotor material. Below 75 RPM the volume fractions measured by tomography and photographic image analysis are within 10% deviation. For low rotational disc speeds, the *n*-heptane volume fraction decreases slightly with increasing rotational disc speed. At higher rotational disc speeds the droplets become smaller, and the *n*-heptane volume fraction becomes equal to the *n*-heptane to total flow ratio. The volume fractions do not depend on the density difference between the two liquids.

The liquid-liquid flow behavior and the liquid-liquid mass transfer rates are obtained from experiments in an SDR. The liquid-liquid mass transfer rate is determined from extraction experiments of benzoic acid from *n*-heptane to water. For the calculation of the overall mass transfer rate the dimerization and acid dissociation equilibria are taken into account.

Three flow patterns are characterized. Up to 100 RPM, continuous radially inwards spiraling *n*-heptane patterns are observed. Between 100 RPM and 300 RPM this continuous spiral changes to spiraling *n*-heptane droplets. Above 300 RPM fully dispersed phase flow is observed. The lowest overall mass transfer rate is measured to be 0.17 m^3_{ORG} m^{-3}_{R} s^{-1} at 100 RPM, and the highest value obtained is equal to 51.5 m^3_{ORG} m^{-3}_{R} s^{-1} at 1600 RPM. These mass transfer rates are at least 25 times higher compared to those in packed columns, and at most 15 times higher compared to mass transfer rates in state of the art microchannels.

The liquid-liquid flow in an impeller-stator SDR is qualitatively described. The impeller has a comparable function as the impeller in a centrifugal pump, and transports liquid from the bottom center to the rim of the impeller. The impeller-stator configuration is able to selectively pump the lighter liquid phase through the reactor, whilst it is intensively mixed with a heavier liquid phase that remains in a stage of the reactor. The liquid-liquid flow is studied by contacting water and *n*-heptane as a function of the rotational speed and aqueous volume fractions. The liquid-liquid flow is characterized by six different flow regimes. These were observed in the space between the impeller and the bottom stator. Dispersion is absent in the full water regime (rotational speed below 50 RPM) and the stagnant ring regime. Water is the dispersed phase in the water droplets regime (rotational speed above 200 RPM) and wavy ring regime (rotational speed between 50 and 200 RPM). *n*-Heptane acts as the dispersed phase in the *n*-heptane droplets regime and the "spiral and ring"-regime. The transitions between the flow regimes are dominated by three effects: the formation of boundary layers on the impeller and the stator, the shear stress intensity and the aqueous volume fraction.

Based on the pumping action of the impeller and on the liquid-liquid mass transfer rates, spinning disc equipment is developed for the counter-current contacting of two immiscible liquids. This equipment is based on rotor-impeller-rotor spinning disc technology and allows for the counter-current contacting and consecutive complete separation of 5 m^3 liquid per day. The mixing intensity and the separation efficiency in the extractor can be chosen independently by adjusting the rotation speed of the impeller and of the rotors. The height of a transfer unit, and thus the extractor volume, is ten times lower compared to common centrifugal extractors.

Finally, the single stage extractor is extended with two additional stages in which benzoic acid is extracted from *n*-heptane to water. Each contacting stage of the extractor consists of a rotor-impeller-rotor sequence. The volume of one contacting stage is 102 10^{-6} m^3. Each additional contacting stage extends the extractor length with 1.4 10^{-2} m. The first prototype of the extractor processes a total volumetric flow of 0.86 m^3 day^{-1}. The separation efficiencies at the extractor outlets and the degree of back mixing between consecutive contacting stages are reported.

The separation efficiency can be tuned to 100% for rotational speeds below 1500 RPM. Mass transfer experiments have shown that the solute concentrations between *n*-heptane and water reach equilibrium at each contacting stage.

8.2. Future perspective

All multiphase experiments in this thesis have been performed with a system comprising water and *n*-heptane. This is a non-conventional extraction system, that was selected because of its moderate compatibility with the construction material of the reactor, poly(methyl methacrylate). The European Federation of Chemical Engineering re-advised in 1985 to use "standard" liquid-liquid extraction test systems: water/acetone/toluene (high interfacial tension), water/acetone/butyl acetate (medium interfacial tension), or water/succinic acid/n-butanol (low interfacial tension). Measurements of the separation efficiency of these systems in the counter-current operated spinning disc equipment will demonstrate the feasibility of this equipment, and thus motivate end-product users to apply the spinning disc extractor in their own liquid-liquid extraction process.

The liquid-liquid mass transfer rate in the single-stage spinning disc extractor needs to be measured as a function of the difference in rotational speed between the impeller and the enclosure. The results in this thesis have shown that the residence time in combination with the liquid-liquid mass transfer rate allows for sufficient mass transfer to reach the equilibrium concentrations of the solute. It would be valuable to determine the liquid-liquid mass transfer rate at a constant difference in the rotational speed of the enclosure and the impeller, which would possibly allow one to measure at a constant droplet size, and thus at a constant interfacial area.

To develop the spinning disc based extractor further, there is an urgent need for the development of concise design rules. Preferably, the liquid-liquid mass transfer rate would be described by a concise design rule as a function of dimensionless parameters, which would allow one to predict the liquid-liquid mass transfer rate as a function of the impeller diameter and the rotational speeds of the impeller and the enclosure. This would allow one to identify the best route for up scaling of the volumetric through flow.

Another design rule for the counter-current operated spinning disc equipment should predict the steady-state radial position of the liquid levels of the heavy phase liquid and the light phase liquid. Variables which should be taken into account for such a design rule are the pressure drop over the extractor, the volumetric flow rate of both liquids, the difference in rotational speed between the impeller and the enclosure, and the liquid densities. This design rule could be obtained by solving the hydrostatic pressure balance, with a term that describes the centrifugal acceleration instead of gravitational acceleration.

Preliminary experiments, in which the backpressures at the extractor outlets were varied at constant flow rates and constant rotational disc speed, have confirmed the overall trends predicted by the hydrostatic pressure balance. There exists an operating window of the rotational disc speeds of the impeller and the enclosure, in which full separation can be achieved at both outlets for fixed liquid densities, outlet pressures, and flow rates (Saffarionpour et al., 2013).

In addition to the hydrostatic pressure balance, the emulsification of the dispersed phase should be taken into account: the droplet size in the emulsion is mainly determined by the interfacial tension and the liquid viscosities, in combination with the rotation difference. A higher rotation difference will give smaller droplets that give a higher mass transfer but which are more difficult to separate. This model should be validated by measuring the separation efficiency at both outlets, and the pressure drop over the extractor.

For the operational conditions at which complete phase separation is achieved, a simultaneous residence time distribution measurement in both liquid phases could be performed. This would give valuable information about possible dead volumes in the extractor, but will also be essential for the modeling of the liquid-liquid mass transfer rate. In addition, the residence time distribution would show if it is possible to have counter-current plug flow behavior of both phases, which would result in multiple contacting steps in a single rotor-impeller-rotor sequence. Such experiments would require a stable and non-intrusive measurement technique at both outlets of the extractor, like inline UV-VIS equipment, and two inert tracers that selectively dissolve in one of the phases.

An unknown characteristic of the spinning disc equipment is the characteristic time scale at which micromixing occurs in the equipment. Such a timescale can experimentally be derived from the product distribution of two parallel competitive reactions, like the Villermaux-Dushman system. This timescale is related to the local energy dissipation, and allows for comparison of equipment.

9. References

Al-Dahhan, M., Highfill, W., Liquid holdup measurement techniques in laboratory high pressure trickle Bed Reactors, *Can. J. Chem. Eng.* **77**, 759 (1999).

Al-Rahawi, M. I., New predictive correlations for the drop size in a rotating disc contactor liquid-liquid extraction column, *Chem. Eng. Tech.* **30**, 184 (2007).

Alessi, V., Penzo, R., Slater, M. J., Tessari, R., Caprolactam production: A comparison of different layouts of the liquid-liquid extraction section, *Chem. Eng. Tech.* **20**, 445 (1997).

Ali, S. H., Lababidi, H. M. S., Merchant, S. Q., Fahim, M. A., Extraction of aromatics from naphtha reformate using propylene carbonate, *Fluid Phase Eq.* **214**, 25 (2003).

Amouei, M., Khadiv-Parsi, P., Moosavian, M. M., Hedayat, N., Davoodi, A. A., Phase inversion in a batch liquid-liquid stirred system, *Ir. J. Chem. Eng.* **2**, 55 (2008).

Anderson, N. G., Using continuous processes to increase production, *Org. Process Res. Dev.* **16**, 852 (2012).

Arirachakaran, S., Oglesby, K. D., Malinowky, M. S., Shoham, O., Brill, J. P., paper presented at the SPE Production Operations Symposium, 1989, pp. 155-167.

Aveyard, R., Saleem, S. M., Interfacial tensions at alkane-aqueous electrolyte interfaces, *Journal of the Chemical Society, Faraday Transactions: Physical Chemistry in Condensed Phases* **72**, 1609 (1976).

Barson, N., Beyer, G. H., Characteristics of a Podbielniak centrifugal extractor, *Chem. Eng. Prog.* **49**, 243 (1953).

Batchelor, G. K., Note on a class of solutions of the Navier-Stokes equations representing steady rotationally-symmetric flow, *Quar. J. Mech. App. Math.* **4**, 29 (1951).

Bieberle, A., Hoppe, D., Hampel, U., paper presented at the Imaging Systems and Techniques (IST), 2010 IEEE International Conference on, 2010a, pp. 261-265.

Bieberle, A., Kronenberg, J., Schleicher, E., Hampel, U., Design of a high-resolution gamma-ray detector module for tomography applications, *Nuclear Instruments and Methods in Physics Research Section A: Accelerators, Spectrometers, Detectors and Associated Equipment* **572**, 668 (2007).

Bieberle, A., Hoppe, D., Schleicher, E., Hampel, U., Void measurement using high-resolution gamma-ray computed tomography, *Nuc. Eng. Des.* **241**, 2086 (2011).

Bieberle, A., Schleicher, E., Hampel, U., Temperature control design for a high-resolution gamma-ray tomography detector, *Rev. Sci. Instrum.* **81**, 014702 (2010b).

Blass, E., in *Liquid-liquid extraction equipment*, J. C. Godfrey, M. J. Slater, Eds. (Hohn Wiley & Sons, Chichester, UK, 1994) , Chapter 14, pp. 533-568.

Bödewadt, U. T., Die drehströmung über festem grunde, *Z. angew. Math. Mech.* **20**, 241 (1940).

Bonnet, J. C., Jeffreys, G. V., Hydrodynamics and mass transfer characteristics of a scheibel extractor. Part I: Drop size distribution, holdup, and flooding, *AIChE J.* **31**, 788 (1985).

Boodhoo, K. V. K., Jachuck, R. J., Process intensification: spinning disk reactor for styrene polymerisation, *App. Therm. Eng.* **20**, 1127 (2000).

Boskovic, D., Loebbecke, S., Modelling of the residence time distribution in micromixers, *Chem. Eng. J.* **135**, S138 (2008).

Brunner, G., Counter-current separations, *J. Supercrit. Fluids* **47**, 574 (2009).

Buffet, D., Centrifuges with hydraulic controls, US4285462, Date issued: 25-8-1981

Buhtz, E, Method of and apparatus for carrying out chemical reactions or physical processes, US1629200, Date issued: 17-5-1927

Burns, J. R., Jachuck, R. J. J., Determination of liquid-solid mass transfer coefficients for a spinning disc reactor using a limiting current technique, *Int. J. of Heat and Mass Trans.* **48**, 2540 (2005).

Caudwell, D. R., Trusler, J. P. M., Vesovic, V., Wakeham, W. A., The viscosity and density of n-dodecane and n-octadecane at pressures up to 200 MPa and temperatures up to 473 K, *Int. J. Thermophysics* **25**, 1339 (2004).

CEFIC, "Facts and Figures 2012, The European chemicals industry in a worldwide perspective" , (CEFIC, 2012).

Cengroš, J., Badin, V., Stefan, P., Residence time distribution in a wiped liquid film, *T. Chem. Eng. J. Biochem. Eng. J.* **59**, 259 (1995).

Cheah, S. C., Iacovides, H., Jackson, D. C., Ji, H., Launder, B. E., Experimental investigation of enclosed rotor-stator disk flows, *Exp. Therm Fluid Sci.* **9**, 445 (1994).

CINC, Solutions http://www.cincsolutions.com/, page accesed: 4-9-2013

Coleby, J, Apparatus for countercurrent treatment of immiscible fluids, US3017253, Date issued: 16-1-1962

Coulson, J. M., Richardson, J. F., Backurst, J. R., Harker, J. H., in *Chemical Engineering,* (Elsevier, 2007), vol. 1. Fluid flow heat transfer and mass transfer , Chapter 8, pp. 314-378.

Craig, L. C., Post, O., Apparatus for Countercurrent Distribution, *Analytical Chemistry* **21**, 500 (1949).

Cros, A., Ali, R., Le Gal, P., Thomas, P. J., Schouveiler, L., Carpenter, P. W., Chauve, M. P., Effects of wall compliance on the laminar–turbulent transition of torsional Couette flow, *J. Fluid. Mecha.* ***481***, 177 (2003).

Cros, A., Le Gal, P., Spatiotemporal intermittency in the torsional Couette flow between a rotating and a stationary disk, *Physics of Fluids* **14**, 3755 (2002).

D.B.Todd, W.J.Podbielniak, Advances in centrifugal extraction, *Chem. Eng. Prog.* **61**, 69 (1965).

Daily, J. W., Nece, R. E., Chamber dimension effects on induced flow and frictional resistance of enclosed disks, *J. Basic. Eng.* **82**, 217 (1960).

Danckwerts, P. V., Continuous flow systems : Distribution of residence times, *Chem. Eng. Sci.* **2**, 1 (1953).

Danckwerts, P. V., Jenkins, J. W., Place, G., The distribution of residence-times in an industrial fluidised reactor, *Chem. Eng. Sci.* **3**, 26 (1954).

de Vries, W., SenterNovem, Ed. (SenterNovem, 2008).

Debuchy, R., Nour, F. A., Bois, G., An analytical modeling of the central core flow in a rotor-stator system with several preswirl conditions, *J Fluids Eng Trans ASME* **132**, 0611021 (2010).

Dehkordi, A. M., Application of a novel-opposed-jets contacting device in liquid-liquid extraction, *CEP:PI* **41**, 251 (2002).

Deshmukh, S. S., Joshi, J. B., Koganti, S. B., Flow visualization and three-dimensional CFD simulation of the annular region of an annular centrifugal extractor, *Ind. Eng. Chem. Res.* **47**, 3677 (2007).

Deshmukh, S. S., Sathe, M. J., Joshi, J. B., Koganti, S. B., Residence time distribution and flow patterns in the single-phase annular region of annular centrifugal extractor, *Ind. Eng. Chem. Res.* **48**, 37 (2008).

Deshpande, K. B., Kumar, S., Phase inversion in agitated liquid-liquid dispersions: Anomalous effect of electrolyte, *Chem. Eng. Sci.* **78**, 33 (2012).

Djaoui, M., Debuchy, R., Heat transfer in a rotor-stator system with a radial inflow, *Comptes Rendus de l'Academie des Sciences - Series IIB - Mechanics-Physics-Chemistry-Astronomy* **326**, 309 (1998).

Dongaonkar, K. R., Pratt, H. R. C., Stevens, G. W., Mass transfer and axial dispersion in a Kühni extraction column, *AIChE J.* **37**, 694 (1991).

Eisenlohr, G. H., Mehrstufige Gegenstromextraktion mit einem neuen Solvent-Zentrifugal-Extraktor, *Chem. Ing. Tech.* **23**, 12 (1951).

Fernandes, J. B., Sharma, M. M., Effective interfacial area in agitated liquid--liquid contactors, *Chem. Eng. Sci.* **22**, 1267 (1967).

Frank, T. C. *et al.*, in *Perry's Chemical Engineer's Handbook*, D. W. Green, R. H. Perry, Eds. (McGraw-Hill, 2012) , Chapter 15, pp. 1-106.

Gaakeer, W. A., de Croon, M. H. J. M., van der Schaaf, J., Schouten, J. C., Liquid-liquid slug flow separation in a slit shaped micro device, *Chem. Eng. J.* **207-208**, 440 (2012).

Gebauer, K., Steiner, L., Hartland, S., Zentrifugalextraktion – Eine Literaturübersicht, *Chem. Ing. Tech.* **54**, 476 (1982).

Ghaini, A., Mescher, A., Agar, D. W., Hydrodynamic studies of liquid-liquid slug flows in circular microchannels, *Chem. Eng. Sci.* **66**, 1168 (2011).

Ghaini, A., Kashid, M. N., Agar, D. W., Effective interfacial area for mass transfer in the liquid-liquid slug flow capillary microreactors, *CEP:PI* **49**, 358 (2010).

Godfrey, J. C., Slater, M. J., *Liquid–Liquid Extraction Equipment* (Wiley, 1994).

Goebel, A., Lunkenheimer, K., Interfacial tension of the water/n-alkane interface, *Langmuir* **13**, 369 (1997).

Gomes, L. N., Guimarães, M. L., Stichlmair, J., Cruz-Pinto, J. J., Effects of Mass Transfer on the Steady State and Dynamic Performance of a Kühni Column – Experimental Observations, *Ind. Eng. Chem. Res.* **48**, 3580 (2009).

Gutoff, E. B., Interstage mixing in an Oldshue-Rushton liquid-liquid extraction column, *AIChE J.* **11**, 712 (1965).

Haddadi, S., Poncet, S., Turbulence modeling of torsional couette flows, *Int. J. Rot. Mach.* **2008**, 1 (2008).

Hafez, M., in *Handbook of Solvent Extraction*, T. C. Lo, M. H. I. Baird, C. Hansen, Eds. (Krieger Publishing COmpany, Malabar, Florida, USA, 1991) , Chapter 15, pp. 459-476.

Hampel, U., Bieberle, A., Hoppe, D., Kronenberg, J., Schleicher, E., Suhnel, T., Zimmermann, F., Zippe, C., High resolution gamma ray tomography scanner for flow measurement and non-destructive testing applications, *Rev. Sci. Instrum.* **78**, 103704 (2007).

Harmand, S., Pelle, J., PONCET, S., Shevchuk, I. V., Review of fluid flow and convective heat transfer within rotating disk cavities with impinging jet, *Int. J. Therm. Sci.* **67**, 1 (2013).

Hashtochahar, E., Safdari, S. J., Haghighi-Asl, A., Torab-Mostaedi, M., Prediction of slip velocity in a Hanson mixer- settler extraction column, *Can. J. Chem. Eng.* **88**, 808 (2010).

Hemrajani, R. R., Tatterson, G. B., in *Handbook of Industrial Mixing - Science and Practice*, E. L. Paul, V. A. Atiemo-Obeng, S. M. Kresta, Eds. (John Wiley & Sons, Hoboken, New Jersey, 2004) , Chapter 6, pp. 345-390.

Horvath, M., Steiner, L., Hartland, S., Prediction of drop diameter, hold-up and backmixing coefficients in liquid-liquid spray columns, *The Canadian Journal of Chemical Engineering* **56**, 9 (1978).

Hosoya, H., Nagakura, S., Spectroscopic studies on reactive intermediates of esterification of aromatic carboxylic acids, *Spectrochimica Acta* **17**, 324 (1961).

Hosoya, H., Tanaka, J., Nagakura, S., Ultraviolet absorption spectra of monomer and dimer of benzoic acid, *J. Mol. Spectrosc.* **8**, 257 (1962).

Imamura, T., Saito, K., Ishikura, S., Nomura, M., A new approach to continuous emulsion polymerization, *Polym. Int.* **30**, 203 (1993).

Ingham, J., Dunn, I. J., Heinzle, E., Prenosil, J. E., in *Chemical Engineering Dynamics*, (Wiley, 2007) , Chapter 3, pp. 168-173.

Itoh, M., Yamada, Y., Imao, S., Gonda, M., Experiments on turbulent flow due to an enclosed rotating disk, *Exp. Therm Fluid Sci.* **5**, 359 (1992).

Jachuck, R., Burns, J. R., in *Encyclopedia of Chemical Processing*, (Taylor & Francis, 2005), pp. 2847-2857.

Jaradat, M., Attarakih, M., Bart, H. J., Advanced prediction of pulsed (packed and sieve plate) extraction columns performance using population balance modelling, *Chem. Eng. Res. Des.* **89**, 2752 (2011).

Jin Kim, M., Sung Ghim, Y., Nam Chang, H., Residence time distribution analysis in controllable flow conditions: case of rotating disk reactor, *Chem. Eng. Sci.* **39**, 813 (1984).

Jones, E., McClean, K., Housden, S., Gasparini, G., Archer, I., Biocatalytic oxidase: Batch to continuous, *Chem. Eng. Res. Des.* **90**, 726 (2012).

Kashid, M. N., Gupta, A., Renken, A., Kiwi-Minsker, L., Numbering-up and mass transfer studies of liquid-liquid two-phase microstructured reactors, *Chem. Eng. J.* **158**, 233 (2010).

Kashid, M. N., Harshe, Y. M., Agar, D. W., Liquid-liquid slug flow in a capillary: an alternative to suspended drop or film contactors, *Ind. Eng. Chem. Res.* **46**, 8420 (2007a).

Kashid, M. N., Agar, D. W., Hydrodynamics of liquid-liquid slug flow capillary microreactor: Flow regimes, slug size and pressure drop, *Chem. Eng. J.* **131**, 1 (2007b).

Kashid, M. N., Renken, A., Kiwi-Minsker, L., Gas-liquid and liquid-liquid mass transfer in microstructured reactors, *Chem. Eng. Sci.* **66**, 3876 (2011).

Keith, F. W., Hixson, A. N., Liquid-Liquid Extraction Spray Columns - Drop Formation and Interfacial Transfer Area, *Ind. Eng. Chem.* **47**, 258 (1955).

Klockgether-Radke, A. P., F. W. Sertürner and the discovery of morphine. 200 Years of pain therapy with opioids, *Anasthesiol. Intensivmed. Notf. med. Schmerzther.* **37**, 244 (2002).

Kraai, G., van Zwol, F., Schuur, B., Heeres, H., de Vries, J., Two-phase (bio)catalytic reactions in a table-top centrifugal contact separator, *Angew. Chem.* **120**, 3969 (2008).

Krishna, R., Sie, S. T., Strategies for multiphase reactor selection, *Chem. Eng. Sci.* **49**, 4029 (1994).

Krishna, R., Nanoti, S. M., Goswami, A. N., Mass-transfer efficiency of sieve tray extraction columns, *Ind. Eng. Chem. Res.* **28**, 642 (2002).

Kumar, Prediction of drop size, dispersed-phase holdup, slip velocity, and limiting throughputs in packed extraction columns, *Chem. Eng. Res. Des.* **72**, 89 (1994).

Kumar, A., Hartland, S., Correlations for prediction of mass transfer coefficients in single drop systems and liquid-liquid extraction columns, *Chem. Eng. Res. Des.* **77**, 372 (1999).

Kumar, A., Steiner, L., Hartland, S., Capacity and hydrodynamics of an agitated extraction column, *Ind. Eng. Chem. Proc. Des. Dev.* **25**, 728 (1986).

Levenspiel, O., in *Chemical Reaction Engineering*, (Wiley, 1999) , Chapter 9.

Likidis, Z., Schlichting, E., Bischoff, L., Schügerl, K., Reactive extraction of penicillin G from mycel-containing broth in a countercurrent extraction decanter, *Biotechnol. Bioeng.* **33**, 1385 (1989).

Likidis, Z., Schügerl, K., Recovery of penicillin by reactive extraction in centrifugal extractors, *Biotechnol. Bioeng.* **30**, 1032 (1987).

Long, B., Wang, Y., Yang, Z., Partition behaviour of benzoic acid in (water and n-dodecane) solutions at T=(293.15 and 298.15)K, *J. Chem. Thermodyn.* **40**, 1565 (2008).

Lyra, M., Ploussi, A., Filtering in SPECT image reconstruction, *Int. J. Bio. Imag.* **2011**, 1 (2011).

MacInnes, D. A., Dayhoff, M. O., The partial molal volumes of potassium chloride, potassium and sodium iodides and of iodine in aqueous solution at 25°C, *JACS* **74**, 1017 (1952).

Madhuranthakam, C. M., Pan, Q., Rempel, G. L., Residence time distribution and liquid holdup in Kenics KMX static mixer with hydrogenated nitrile butadiene rubber solution and hydrogen gas system, *Chem. Eng. Sci.* **64**, 3320 (2009).

Martin, A. D., Interpretation of residence time distribution data, *Chem. Eng. Sci.* **55**, 5907 (2000).

Meeuwse, M., Lempers, S., van der Schaaf, J., Schouten, J. C., Liquid-solid mass transfer and reaction in a rotor-stator spinning disc reactor, *Ind. Eng. Chem. Res.* **49**, 10751 (2010a).

Meeuwse, M., Hamming, E., van der Schaaf, J., Schouten, J. C., Effect of rotor-stator distance and rotor radius on the rate of gas-liquid mass transfer in a rotor-stator spinning disc reactor, *CEP:PI* **50**, 1095 (2011).

Meeuwse, M., van der Schaaf, J., Kuster, B. F. M., Schouten, J. C., Gas-liquid mass transfer in a rotor-stator spinning disc reactor, *Chem. Eng. Sci.* **65**, 466 (2010b).

Meeuwse, M., van der Schaaf, J., Schouten, J. C., Mass transfer in a rotor-stator spinning disk reactor with cofeeding of gas and liquid, *Ind. Eng. Chem. Res.* **49**, 1605 (2009).

Meeuwse, M., van der Schaaf, J., Schouten, J. C., Multistage rotor-stator spinning disc reactor, *AIChE J.* **58**, 247 (2012).

Merchuk, J. C., Shai, R., Wolf, D., Experimental study of copper extraction with LIX-64N by means of motionless mixers, *Ind. Eng. Chem. Proc. Des. Dev.* . **19**, 91 (1980).

Miachon, J. P., Installation for the centrifugal extraction of one liquid by another, US4220279, Date issued: 9-2-1980

Míšek, T., in *Liquid-liquid extraction equipment*, J. C. Godfrey, M. J. Slater, Eds. (John Wiley & Sons, 1994) , Chapter 5.

Mohammadi, S., Boodhoo, K., Online conductivity measurement of residence time distribution of thin film flow in the spinning disc reactor, *Chem. Eng. J.* **207-208**, 885 (2012).

Muller, E., Berger, R., Blass, E., Sluyts, D., Pfennig, A., in *Ullmann's Encyclopedia of Industrial Chemistry*, (Wiley-VCH Verlag, 5008), pp. 249-307.

Nauman, E. B., in *Handbook of industrial mixing*, E. L. Paul, V. A. Atiemo-Obeng, S. M. Kresta, Eds. (John Wiley & Sons, Hoboken, New Jersey, 2004) , Chapter 1, pp. 1-17.

Norato, M. A., Tavlarides, L. L., Tsouris, C., Phase inversion studies in liquid-liquid dispersions, *Can. J. Chem. Eng.* **76**, 486 (1998).

Nour, F. A., Debuchy, R., Bois, G., Influence of a weak superposed centripetal flow in a rotor-stator system for several pre-swirl ratio, *ASME Conference Proceedings* **2011**, 2921 (2011).

Ogihara, T., Matsuda, G., Yanagawa, T., Ogata, N., Fujita, K., Nomura, M., Continuous synthesis of monodispersed silica particles using couette-taylor vortex flow, *J. Ceram. Soc. Jpn.* **103**, 151 (1995).

Otsu, N., A threshold selection method from gray-level histograms, *IEEE Transactions on Systems, Man and Cybernetics* **9**, 62 (1979).

Owen, J. M., Rogers, R. H., in *Flow and heat transfer in rotating-disc systems.*, Morris W.D., Ed. John Wiley & sons, 1989) , Chapter 7.

Oxley, P., Brechtelsbauer, C., Ricard, F., Lewis, N., Ramshaw, C., Evaluation of spinning disk reactor technology for the manufacture of pharmaceuticals, *Ind. Eng. Chem. Res.* **39**, 2175 (2000).

Parker, D. S., O'Connor, E. W., Bagdigian, R., paper presented at the Int. Conf. Env. Sys., Denver, Co, USA, 1999.

Pask, S. D., Nuyken, O., Cai, Z., The spinning disk reactor: an example of a process intensification technology for polymers and particles, *Polym. Chem.* **3**, 2698 (2012).

Pawar, R. R., Nahire, S. B., Hasan, M., Solubility and density of potassium iodide in binary ethanol–water solvent mixture at (298.15, 303.15, 308.15, and 313.15) K, *J. Chem. Eng. Data.* **54**, 1935 (2009).

Podbielniak, W. J., Gavin, A. M., Kaiser, H. R., Use of the centrifugal contactor for water-washing of refined oils, *J. Am. Oil Chem. Soc.* **36**, 238 (1959).

Poncet, S., Chauve, M. P., Le Gal, P., Turbulent rotating disk flow with inward throughflow, *J. Fluid. Mecha.* **522**, 253 (2005a).

Poncet, S., Chauve, M. P., Schiestel, R., Batchelor versus Stewartson flow structures in a rotor-stator cavity with throughflow, *Physics of Fluids* **17**, 075110 (2005b).

Poncet, S., Schiestel, R., Chauve, M. P., Centrifugal flow in a rotor-stator cavity, *J. Fluids Eng.* **127**, 787 (2005c).

Reay, D., Ramshaw, C., Harvey, A., *Process intensification, engineering for efficiency, sustainability and flexibility* (Butterworth-Heinemann, Oxford, ed. 1, 2008), p. xxi.

Rocha, J. A., Cardenas, J. C., Garcia, J. A., Preliminary design of sieve tray extraction columns. 2. Determination of the column height. Overall efficiency of sieve tray extractors, *Ind. Eng. Chem. Res.* **28**, 1879 (1989a).

Rocha, J. A., Carlos Cardenas, J., Sosa, C., Rosales, J., Preliminary design of sieve tray extraction columns. 1. Determination of the column diameter. Flooding velocities in sieve tray extractors, *Ind. Eng. Chem. Res.* **28**, 1873 (1989b).

Rothfeld, L. B., Ralph, J. L., Equivalence of pulse and step residence time measurements in a trickle-phase bed, *AIChE J.* **9**, 852 (1963).

Rousselet Robatel http://www.robatel.com/, page accesed: 21-2-2013

Saber, M., Huu, T. T., Pham-Huu, C., Edouard, D., Residence time distribution, axial liquid dispersion and dynamic–static liquid mass transfer in trickle flow reactor containing ß-SiC open-cell foams, *Chem. Eng. J.* **185-186**, 294 (2012).

S. Saffarionpour, J. van der Schaaf, J. C. Schouten, F. de Boeff, Stan Ackermans Institute (2013).

Scheibel, E. G., Performance of an internally baffled multistage extraction column, *AlChE J.* **2**, 74 (1956).

Scheibel, E. G., Karr, A. E., Semicommercial multistage extraction column - performance characteristics, *Ind. Eng. Chem.* **42**, 1048 (1950).

Schlichting, H., Gersten, K., *Boundary Layer Theory* (Springer-Verlag Telos, ed. 8st, revised, 1999), p. -801.

Schouveiler, L., Le Gal, P., Chauve, M. P., Instabilities of the flow between a rotating and a stationary disk, *J. Fluid. Mecha.* **443**, 329 (2001).

Schubert, M., Bieberle, A., Barthel, F., Boden, S., Hampel, U., Advanced Tomographic Techniques for Flow Imaging in Columns with Flow Distribution Packings, *Chem. Ing. Tech.* **83**, 979 (2011).

Schuur, B., Kraai, G. N., Winkelman, J. G. M., Heeres, H. J., Hydrodynamic features of centrifugal contactor separators: Experimental studies on liquid hold-up, residence time distribution, phase behavior and drop size distributions, *CEP:PI* **55**, 8 (2012).

Sczechowski, J. G., Koval, C. A., Noble, R. D., A Taylor vortex reactor for heterogeneous photocatalysis, *Chem. Eng. Sci.* **50**, 3163 (1995).

Seibert, A. F., Fair, J. R., Hydrodynamics and mass transfer in spray and packed liquid-liquid extraction columns, *Ind. Eng. Chem. Res.* **27**, 470 (1988).

Selker, A. H., Sleicher, C. A., Factors affecting which phase will disperse when immiscible liquids are stirred together, *Can. J. Chem. Eng.* **43**, 298 (1965).

Smith, A. S., Solutropes, *Ind. Eng. Chem.* **42**, 1206 (1950).

Soltanali, S., Ziaie-Shirkolaee, Y., Amoabediny, G., Rashedi, H., Sheikhi, A., Chamanrokh, P., Hydrodynamics and mass transfer performance of rotating sieved disc contactors used for reversed micellar extraction of protein, *Chem. Eng. Sci.* **64**, 2301 (2009).

Stankiewicz, A. I., Moulijn, J. A., Process intensification: Transforming chemical engineering, *Chem. Eng. Prog.* **96**, 22 (2000).

Steensma, M., Westerterp, K. R., Thermally safe operation of a cooled semi-batch reactor. Slow liquid-liquid reactions, *Chem. Eng. Sci.* **43**, 2125 (1988).

Steiner, L., Shoukry, E., Hartland, S., Conductometric measurement of particle size in a dispersion, *Ind. Eng. Chem. Fund.* **13**, 267 (1974).

Stewartson, K., On the flow between two rotating coaxial disks, *Mathematical Proceedings of the Cambridge Philosophical Society* **49**, 333 (1953).

Stichlmair, J., Leistungs- und Kostenvergleich verschiedener Apparatebauarten für die Flüssig/Flüssig-Extraktion, *Chem. Ing. Tech.* **52**, 253 (1980).

Su, Y., Zhao, Y., Chen, G., Yuan, Q., Liquid-liquid two-phase flow and mass transfer characteristics in packed microchannels, *Chem. Eng. Sci.* **65**, 3947 (2010).

Thulasidas, T. C., Abraham, M. A., Cerro, R. L., Dispersion during bubble-train flow in capillaries, *Chem. Eng. Sci.* **54**, 61 (1999).

Thyn, J., Zitny, R., Radiotracer applications for the analysis of complex flow structure in industrial apparatuses, *Nuclear Instruments and Methods in Physics Research Section B: Beam Interactions with Materials and Atoms* **213**, 339 (2004).

Torres, A. P., Oliveira, F. A. R., Residence time distribution studies in continuous thermal processing of liquid foods: a review, *J. Food Eng.* **36**, 1 (1998).

Trambouze, P., Euzen, J. P., in *Chemical Reactors, From design to operation*, (Institute Français du pétrole publications, Paris, Fr, 2002) , Chapter 5, pp. 299-346.

Tschentscher, R., Schubert, M., Bieberle, A., Nijhuis, T. A., van der Schaaf, J., Hampel, U., Schouten, J. C., Tomography measurements of gas holdup in rotating foam reactors with Newtonian, non-Newtonian and foaming liquids, *Chem. Eng. Sci.* **66**, 3317 (2011).

Tschentscher, R., Schubert, M., Bieberle, A., Nijhuis, T. A., van der Schaaf, J., Hampel, U., Schouten, J. C., Gas holdup of rotating foam reactors measured by tomography - effect of solid foam pore size and liquid viscosity, *AIChE J.* **DOI: 10.1002/aic.13787**, (2012).

Tsierkezos, N. G., Molinou, I. E., Thermodynamic poperties of water + ethylene glycol at 283.15, 293.15, 303.15, and 313.15 K, *J. Chem. Eng. Data* **43**, 989 (1998).

Urrutia, G., Bonelli, P., Cassanello, M. C., Cukierman, A. L., On dynamic liquid holdup determination by the drainage method, *Chem. Eng. Sci.* **51**, 3721 (1996).

van der Schaaf, J., Schouten, J. C., High-gravity and high-shear gas-liquid contactors for the chemical process industry, *Curr. Opin. Chem. Eng.* **1**, 84 (2011).

van der Schaaf, J., Visscher, F., Bindraban, D., and Schouten, J. C., Device for multi phase and single phase contacting, WO/2012/150226 A1, Date issued: 30-4-2012

van Eeten, K. M. P., van der Schaaf, J., Schouten, J. C., van Heijst, G. J. F., Boundary layer development in the flow field between a rotating and a stationary disk, *Physics of Fluids* **24**, 033601 (2012).

Varteressian, K. A., Fenske, M. R., Performance of a packed extraction column, using continuous countercurrent, *Ind. Eng. Chem.* **28**, 928 (2002).

Vedantam, S., Joshi, J. B., Annular centrifugal contactors – A review, *Chem. Eng. Res. Des.* **84**, 522 (2006).

Visscher, F., Nijhuis, R. T. R., de Croon, M. H. J. M., van der Schaaf, J., Schouten, J. C., Liquid-liquid flow in an impeller-stator spinning disc reactor, *CEP:PI* **DOI:10.1016/j.cep.2013.01.015**, (2012a).

Visscher, F., Saffarionpour, S., de Croon, M. H. J. M., van der Schaaf, J., Schouten, J. C., Counter-current liquid-liquid contacting in an spinning disc reactor, *Unpublished work* (2013).

Visscher, F., Bieberle, A., Schubert, M., van der Schaaf, J., de Croon, M. H. J. M., Hampel, U., Schouten, J. C., Water and n-heptane volume fractions in a rotor-stator spinning disc reactor, *Ind. Eng. Chem. Res.* **51**, 16670 (2012b).

Visscher, F., de Hullu, J., de Croon, M. H. J. M., van der Schaaf, J., Schouten, J. C., Residence time distribution in a single phase rotor-stator spinning disc reactor, *AIChE J.* **59**, 2686 (2012c).

Visscher, F., Gaakeer, W. A., Granados Mendoza, P., de Croon, M. H. J. M., van der Schaaf, J., Schouten, J. C., Liquid-liquid extraction systems of benzoic acid in water and heptane, methylbenzene, or trichloroethylene as cosolvent, *J. Chem. Eng. Data.* **56**, 3630 (2011).

Visscher, F., van der Schaaf, J., de Croon, M. H. J. M., Schouten, J. C., Liquid-liquid mass transfer in a rotor–stator spinning disc reactor, *Chem. Eng. J.* **185-186**, 267 (2012d).

von Kármán, T., Über laminare und turbulente reibung, *Z. angew. Math. Mech.* **1**, 233 (1921).

Will, B. C., Benra F. K. The rise of complexity in describing fluid flow in rotating cavities. 2008 Proceedings of the ASME Fluids Engineering Division Summer Conference, FEDSM 2008 2, 261-270. 2009. Jacksonville, FL. 2008 ASME Fluids Engineering Division Summer Conference, FEDSM 2008. 10-8-2008.

Wiseman, P., *An introduction to industrial chemistry* (Applied Science Publishers, London, ed. Second edition, 1979).

Xu, J. Q., Duan, W. H., Zhou, X. Z., Zhou, J. Z., Extraction of phenol in wastewater with annular centrifugal contactors, *J. Hazard. Mater.* **131**, 98 (2006).

Yeo, L. Y., Matar, O. K., Perez de Ortiz, E. S., Hewitt, G. F., Phase inversion and associated phenomena, *Multiphase Science and Technology* **12**, 51 (2000).

Zaldívar, J. M., Molga, E., Alós, M. A., Hernández, H., Westerterp, K. R., Aromatic nitrations by mixed acid. Fast liquid-liquid reaction regime, *Chemical Engineering and Processing* **35**, 91 (1996).

Zhang, Han, Viscosity and density of water + sodium chloride + potassium chloride solutions at 298.15 K, *J. Chem. Eng. Data.* **41**, 516 (1996).

Zhao, Y., Chen, G., Yuan, Q., Liquid-liquid two-phase mass transfer in the T-junction microchannels, *AIChE J.* **53**, 3042 (2007).

10. List of publications

Journal publications

- Visscher, F., Gaakeer, W.A., Granados Mendoza, P., de Croon, M.H.J.M., van der Schaaf, J, Schouten, J.C., "**Liquid-liquid extraction systems of benzoic acid in water, and *n*-heptane, methylbenzene, or trichloroethylene as co-solvent**", *Journal of Chemical Engineering Data*, 2011, 56 (9), pp. 3630–3636.
- Visscher F., van der Schaaf, J., de Croon, M.H.J.M., Schouten, J.C., **"Liquid-liquid mass transfer in a rotor-stator spinning disc reactor",** *Chemical Engineering Journal*, 2012, 185-186, pp. 267-273.
- Visscher, F., Bieberle, A., Schubert, M., van der Schaaf, J., de Croon, M.H.J.M., Hampel, U., Schouten, J.C., "**Water and *n*-heptane volume fractions in a rotor-stator spinning disc reactor",** *Industrial & Engineering Chemistry Research*, 2012, 51 (51), pp. 16670-16676.
- Visscher F., de Hullu, J. van der Schaaf, J., de Croon, M.H.J.M., Schouten, J.C., **"Single phase residence time distribution in a rotor-stator spinning disc reactor",** *AIChE Journal*, 2013, 59 (7), pp. 2686-2693.
- Visscher F., Nijhuis, R.T.R. van der Schaaf, J. de Croon, M.H.J.M., Schouten, J.C., **"Liquid-liquid flow in an impeller-stator spinning disc reactor",** *Chemical Engineering and Processing: Process Intensification*, DOI: 10.1016/j.cep.2013.01.015, 2013.
- Visscher F., van der Schaaf, J., Nijhuis, T.A., Schouten, J.C., **"Rotating Reactors – A Review",** *Chemical Engineering Research and Design*, DOI: 10.1016/j.cherd.2013.07.021, 2013.
- Visscher, F., Saffarionpour, S., de Croon, M.H.J.M., van der Schaaf, J., Schouten J.C., **"Counter-current liquid-liquid extraction in a high-gravity extractor",** submitted, *AIChE Journal*, 2013.
- Visscher F., van der Schaaf, J., de Croon, M.H.J.M., Schouten, J.C., **"Liquid-liquid separation in a three-stage high-gravity extractor",** submitted, *Separation & Purification Technology*, 2013.

Oral presentations

- Visscher, F., de Croon, M.H.J.M., van der Schaaf, J., Schouten, J.C., **"Counter-current liquid-liquid flow in a high-shear high-gravity extractor"**, Accepted; *World Conference of Chemical Engineering*, August 18-23, 2013, Seoul, Korea.
- Visscher, F., Saffarionpour, S., de Croon, M.H.J.M., van der Schaaf, J., Schouten, J.C., **"Counter-current liquid-liquid extraction in a high-shear high-gravity extractor"**, *European Congress of Chemical Engineering*, April 21-24, 2013, The Hague, The Netherlands.
- Visscher, F., Saffarionpour, S., de Croon, M.H.J.M., van der Schaaf, J., Schouten, J.C., **"Counter-current liquid-liquid flow in a high-shear high-gravity extractor"**, *North American Symposium on Chemical Reactor Engineering* (NASCRE-3), March 17-20, 2013, Houston, USA.
- Visscher, F., Chen, X., van der Schaaf, J., de Croon, M.H.J.M., Schouten, J.C., **"Experimental and Numerical Study of Micromixing in a Rotor-Stator Spinning Disc Reactor"**, *Netherlands Process Technology Symposium 2011* (NPS-11), 24-26 October 2011, Arnhem, The Netherlands (pp. 45).
- Visscher, F. Chen, X., van der Schaaf, J., de Croon, M.H.J.M., Schouten, J.C., **"Experimental validation of a novel model for the micromixing intensity in a rotor-stator spinning disc reactor"**, *American Institute of Chemical Engineers Annual Meeting 2011*: October 16-21, 2011, Minneapolis, USA.
- Visscher, F. van der Schaaf, J., de Croon, M.H.J.M., Schouten, J.C., **"Liquid-liquid mass transfer in a rotor-stator spinning disc reactor"**, *American Institute of Chemical Engineers Annual Meeting 2011*: October 16-21, 2011, Minneapolis, USA.
- Schaaf, J. van der, Visscher, F., Eeten, K.M.P. van, Croon, M.H.J.M. de & Schouten, J.C., **"Process intensification of multiphase processes with a rotor-stator spinning disc reactor"**, *American Institute of Chemical Engineers Annual Meeting 2011*: October 16-21, 2011, Minneapolis, USA.
- Visscher F., van der Schaaf, J., Croon, M.H.J.M., Schouten, J.C., **"Liquid-liquid mass transfer in a rotor-stator spinning disc reactor"**, *European Congress of Chemical Engineering*, September 25 - 29, 2011, Berlin, Germany.

Poster presentations

- Visscher, F., de Hullu, J., de Croon, M.H.J.M., van der Schaaf, J., Schouten, J.C., **"Residence time distribution in a rotor-stator spinning disc reactor"**, *Proceedings of the International Symposium on Chemical Reaction Engineering*, September 2-5, 2012, Maastricht, The Netherlands.
- Visscher F., Croon, M.H.J.M., van der Schaaf, J., Schouten, J.C., **"Liquid-liquid processes in rotating high-shear equipment"**, *Netherlands Process Technology Symposium 2009* (NPS-9), 26-28 October, Veldhoven. Netherlands (pp. 130).
- van der Schaaf, J., de Hullu, J., Visscher, F., de Croon, M.H.J.M., Schouten, J.C., **"Residence time distribution in a rotor-stator spinning disc reactor"**, *Proceedings of the 3rd European Process Intensification Conference*, June 20-23, 2011, Manchester, United Kingdom.
- Visscher F., Croon, M.H.J.M., van der Schaaf, J., Schouten, J.C., **"Spinning disc contactor for high-shear, high-gravity liquid-liquid processes"**, *Proceedings of the XIth Netherlands Catalysis and Chemistry Conference* (NCCC XI), 01-03 March 2010, Noordwijkerhout, Netherlands (pp. 307).
- Visscher F., van der Schaaf, J., Croon, M.H.J.M., Schouten, J.C., **"Liquid-liquid mass transfer in rotating high-shear equipment"**. *Netherlands Process Technology Symposium 2010* (NPS-10), 25-27 October 2010, Veldhoven. Netherlands.

Patent application

- J. van der Schaaf, F. Visscher, D. Bindraban, J. C. Schouten, "**Device for multi phase and single phase contacting**", Technische Universiteit Eindhoven. WO/2012/150226. Filed: 4-30-2012. Netherlands.

Remaining

- Visscher, F., van der Schaaf, J., Schouten, J.C., **"Een nieuwe generatie meerfase reactoren"**, 564ste lezing Chemisch Kring Eindhoven, April 24th 2011.
- Schouten, J.C., Visscher, F., **"De moderne chemische reactor, van geroerde pot naar multi-functioneel apparaat**", Woudschoten Chemie Conferentie, November 2nd, 2012.
- Visscher, F., "**Verdraaid efficiënt**", in: "Exact wat je zoekt, Research4U, Lessenserie voor het vwo", van: Stichting C3, 2012.

Dankwoord – Acknowledgement

Are we there yet?
- *Donkey, Shrek 2*

There is a kind of happiness and wonder that makes you serious.
It is too good to waste on jokes.
- *C.S. Lewis, The last battle*

Een wetenschappelijke promotie is een voortdurende strijd met jezelf. Ik heb de eer en het genoegen gehad deze strijd aan te gaan met creatieve, bevlogen en bedreven mensen aan mijn zijde. Daarbij komt als eerste mijn dank toe aan mijn wetenschappelijke begeleiders.

Hooggeleerde promotor, beste Jaap, je hebt al mijn schrijfsels en ideeën van inhoudelijk en tekstueel commentaar voorzien. Ik zal daar de rest van mijn professionele carrière veel aan hebben. Als nauwkeurig snellezen ooit een Olympische sport zou worden, eindig je met stip op één. Dat onze overlegmomenten behouden bleven toen je meer bestuurstaken kreeg heb ik erg gewaardeerd. Je snelle en oplossingsgerichte manier van zaken doen maakt het onderzoek niet alleen beter maar ook leuker. Je hebt mij veel vrijheid gegeven, en stuurde bij waar dat nodig was. Dank.

Zeergeleerde co-promotor, beste John, ik wil je bedanken dat ik heb mogen genieten van je oneindige ideeënstroom. Je bent een baken van kennis over een grote verscheidenheid van onderwerpen. Dat maakt discussies met jou altijd vernieuwend en verrassend. De felheid van onze discussies is illustratief voor je gedrevenheid: mijn onderzoek is daar vaak beter van geworden. Je hebt een groot talent voor het fenomenologisch verklaren van experimentele resultaten. Ook je betrokkenheid bij mijn leven buiten het inhoudelijke project heb ik gewaardeerd.

Mart, dank voor de gesprekken, recepten, mathematische exercities en voor je ongenuanceerde meningen die je altijd paraat hebt. Ik ga je gelach om mijn 'Fransismen' missen en wens je graag nog veel plezier in de jaren tot je pensioen en daarna met MC^2.

Ik wil ook graag Denise bedanken. Je hebt mij gedurende vier jaren door alle formulieren, formaliteiten en deadlines heen geholpen. Je wist altijd op al mijn vragen antwoorden. Dank daarvoor.

I thank prof. dr. ir. Stankiewicz, dr. Boodhoo, dr. ir. De Rijke and prof. dr. ir. Janssen for their willingness to participate in my PhD graduation committee.

Ook wil ik graag prof. dr. Meuldijk bedanken. De afgelopen meer dan 8 jaar bent u zeer betrokken geweest bij mijn studie en mijn promotie. Een startende student kan zich geen betere en meer betrokken mentor wensen, waarvoor mijn dank.

Kapitel 4 dieser Arbeit konnte nicht entstehen ohne den Beitrag meiner deutschen Kollegen, wofür ich mich herzlich bedanke. Weiterhin danke ich Prof. Dr. Uwe Hampel, Dr. Markus Schubert und Dr. André Bieberle für die freundliche Unterstützung, Gastfreundschaft und wissenschaftliche Exzellenz, die ich während der Arbeit am Helmholz-Zentrum Dresden-Rossendorf erlebt habe.

This research received funding from the European Research Council under the European Community's Seventh Framework Programme (FP7/2007-2013) / ERC grant agreement n° 227010, which is gratefully acknowledged. Various industrial experts-in-the-field provided advice throughout the project: I am especially grateful to Tommy Norén and Kasper Hoglund from Alfa Laval, and Raf Reintjens from DSM Innovative Synthesis.

Vanuit de technische ondersteuning was er binnen de capaciteitsgroep SCR veel vakmanschap, betrokkenheid, en tomeloos geduld om ongeduldige promovendi zo snel mogelijk te helpen. Madan, je hebt prachtig ontwerpen uitgedacht. Bedankt voor de mooie plaatjes waar je menig avond op hebt zitten zwoegen, en voor je prachtige schaterlach. Ik heb veel over werktuigbouwkunde van je geleerd en weet zeker dat er nog meer mooie spinning disc kindjes zullen volgen.

Ook dank aan Erik: een promovendus is gezegend met een technicus die om 12 uur 's nachts via Skype behulpzaam wil zijn. Anton, Dolf, Theo en Chris: dank voor de vele uren sleutelhulp en uitleg. Ook de mensen van de GTD ben ik erkentelijk: Harry, Paul B, Jan, en Luciano. Paul Aendenroomer: dank dat je tijd hebt gemaakt om mijn opstellingen werkend te krijgen en te houden. Peter, Carlo en Marlies, jullie stonden altijd klaar om mij te helpen met waardevolle adviezen en met gezelligheid: jullie zijn het sociale hart van de groep.

Mijn studentenroedel ben ik zeer erkentelijk voor het vele werk dat zij hebben verricht: Stefan, Jannes, Jos, Sven, Xiaoping, Paola, Rik, Ben, Shima en Mirjam: bedankt! Veel van jullie werk is essentieel geweest voor dit proefschrift. Ik heb erg genoten van jullie doorzettingsvermogen en creativiteit. Voor de micromengers onder jullie: helaas is jullie onderwerp niet in dit proefschrift aan bod gekomen. Dat maakt het onderwerp echter niet minder relevant of interessant. Het is het laaghangende fruit dat overblijft aan het eind van dit promotieonderzoek.

Graag bedank ik ook ir. Wijers voor de leerzame discussies bij de verschillende afstudeersessies. Ook bedank ik hier Niels Deen en Maike Baltussen voor de leerzame experimenten met hun hogesnelheidscamera. De metingen van de grensvlak-spanningen had ik niet zonder Jos Laven kunnen doen, waarvoor mijn dank.

Het werk in dit proefschrift bouwt voort op het eerdere promotieonderzoek van Marco Meeuwse. Marco, je hebt bij je vertrek elegante opstellingen achtergelaten waar ik dankbaar gebruik van heb gemaakt. Dank voor het op weg helpen en voor het behoeden voor ongelukken (terzijde: je bent een boefje: het was niet mijn schuld!).

Het is gaaf dat ik het spinning disc onderzoek in goede handen kan achterlaten. Kevin, Paola, Michiel, Slaviša, Shohreh: heel veel succes en plezier met het afronden van jullie promotieprojecten. In ditzelfde kader dank ik ook de jongens van Spinid: Wouter, Wessel, Jeoffrey, Job en Maarten. Dank voor de vele enthousiaste discussies, verhalen en natuurlijk voor ons YouTube filmpje! Tijdens mijn promotie was er (soms) ook tijd voor ontspanning. Spelletjesavonden, verjaardagsborrels, zweefvliegen, het bezoek aan de Efteling, en de ultieme net-niet afscheidsborrel. Frustraties en ideeën kon ik altijd eerst kwijt bij mijn kamergenoten: Maria, Roman, Michael, en Michiel. Dank voor de gezellige tijd, mooie verhalen, en jullie betrokkenheid.

In vier jaar is er een grote doorloop aan collega's geweest. Martin dank ik voor zijn verfrissende humor en zijn voorliefde voor goede documentaires en Xander voor de vele gedeelde koffiepauzes (en frequent flyer tips). Met plezier heb ik samengewerkt en samen genoten met Vitaly, Wim, Emila, Nopi, Fernanda, Violeta, Dulce, Lara, Jun, Bruno, Chattarbir, Jack, Christine, Faysal, Ivana, Jiaqi, Joost, Judith, Lidia, Ma'moun, Mohamed, Narendra, Serdar, Stijn, en Qi.

Academische vorming vond ook buiten werktijd plaats. Met Fokko waren er veel hoogte- en dieptepunten: dank je wel dat je er bent: ik wens je professioneel en privé de onmisbare zegen toe. Veel heb ik te danken aan de VGSEi en haar leden. Goede discussies, grappen en gesprekken zullen mij altijd bij blijven waarvan die met Jorg, John, Lisanne en Marten in het bijzonder. Binnen SCR zijn Michiel van der Stelt en Tom goede vrienden geworden. Ik deel met elk van jullie interesses buiten de bètawetenschap. Dank voor de vele koffie, concerten, en lezingen.

De laatste alinea is voor mijn familie. Jullie hebben mij mijn gehele Eindhovense verblijf onvoorwaardelijk gesteund, vanaf de allereerste tentamens tot de laatste pagina's van dit proefschrift. Ik kan daar niet dankbaar genoeg voor zijn, dank voor jullie toewijding en wijsheid. Esther: je bent mijn ware koningin. Dank dat je er altijd voor mij bent geweest, zonder jou en Annelise als mijn thuisfront had ik dit niet kunnen en willen doen.

Eindhoven, juli 2013

About the author

Frans Visscher was born in Zaanstad, The Netherlands on June 4th 1985. After finishing secondary school (MAVO in 2001, HAVO in 2003), he obtained his propaedeutics in Analytical Chemistry at Hogeschool Inholland in 2004. That same year, he started with the Bachelor Chemical Engineering and Chemistry at Eindhoven University of Technology. Subsequently he obtained his MSc. degree from that same university with a thesis entitled: "Enzymatic hydrolysis of nitrile endgroups", under combined supervision of prof. dr. J. Meuldijk (Process Development Group) and prof.dr. C.E. Koning (Laboratory of Polymer Chemistry). In July 2009 he started his PhD research in the Laboratory of Chemical Reactor Engineering under supervision of prof.dr.ir. J.C. Schouten, dr.ir. J. van der Schaaf, and dr. M.H.J.M. de Croon. The results thereof are described in this thesis. From July 1st 2013 he is working as a scientist at the Technology and Innovation center of SABIC Europe in Geleen, The Netherlands.